POWDER PROCESSING, DENSIFICATION BEHAVIOUR, MICROSTRUCTURE AND MECHANICAL PROPERTIES OF AL_2O_3- 50 Vol% ZrO_2 COMPOSITES

A Thesis Submitted in Partial Fulfillment of the
Requirements for the Degree of

DOCTOR OF PHILOSOPHY

in

ENGINEERING

by

RAGHUNATH PRASAD RANA
(Roll No: 50408003)

Supervisors:
Dr. Santanu Bhattacharyya
Dr. Swadesh Kumar Pratihar

DEPARTMENT OF CERAMIC ENGINEERING
NATIONAL INSTITUTE OF TECHNOLOGY ROURKELA
NOVEMBER, 2009

NATIONAL INSTITUTE OF TECHNOLOGY
ROURKELA, INDIA

CERTIFICATE

This is to certify that the thesis entitled “Powder Processing, Densification Behaviour, Microstructure and Mechanical Properties of Al_2O_3- 50 vol% ZrO_2 Composites” being submitted by Mr. Raghunath Prasad Rana for the degree of Doctor of Philosophy in Engineering, is a record of bonafied research work carried out by him under our supervision at Department of Ceramic Engineering. To the best of our knowledge, the work has not been submitted to any other University or Institute for the award of any degree or diploma.

(S Bhattacharyya)	(S K Pratihar)
Professor	Associate Professor
Department of Ceramic Engineering	Department of Ceramic Engineering

Dedicated to my parents

CONTENTS

Chapter I - Introduction

Chapter II - Literature Review

Chapter IV - Experimental Work

Chapter V - Results and Discussion

Effect of Y_2O_3 Doping on the Properties of Al_2O_3-ZrO_2 Composites

Densification Kinetics of Al_2O_3-ZrO_2 Composites

Chapter VI - Results and Discussion – Al_2O_3-Y-ZrO_2 Composites

Chapter VII- Conclusions and Scope of Further work

Publications resulting from the Ph.D. work

Curriculum Vitae

Abstract

Al_2O_3-ZrO_2 composites containing nominally equal volume fraction of Al_2O_3 and ZrO_2 were prepared through solution chemistry route using inorganic precursors of $AlCl_3$ and $ZrOCl_2$. It was expected that the solution chemistry route will yield highly reactive fine powders which could be sintered into a dense composite with a small grain size. Such a microstructure is expected to retain *t*-ZrO_2 without the use of stabilizers. Three different processing routes, viz gelation (ROUTE 1), precipitation (ROUTE 2) and precipitation followed by washing (ROUTE 3) (consisting of hot water and alcohol washing) were employed. However, the ROUTE 1 powders could be sintered only up to 72% relative density and the highest density was 88% for ROUTE 3. FTIR and DSC/TG studies revealed that the washing process not only removed soluble salts but also helped to reduce the extent of agglomeration and produced softly agglomerated powders. However, the washing process could not completely remove chlorides and the presence of the residual chlorine hindered densification by creating residual pores during the final densification stage. The sintered samples had nearly equal grain sizes (1.9 μm and 1.5 μm for Al_2O_3 and ZrO_2 respectively). However, extensive microcracking resulted during spontaneous t→m transformation of ZrO_2 during cooling from the sintering temperature. The combined effect of microcracking and low sintered density resulted in poor mechanical properties (σ_f = 64 MPa, K_{IC} = 1.74 $MPam^{1/2}$, H_V = 4.1 GPa). The partial substitution of chloride precursor by nitrate precursor ($Al(NO_3)_3$ for $AlCl_3$) (ROUTE 4) resulted in improved sintered density (95% relative density) but grain size was more than the critical size for prevention of spontaneous t→m transformation during cooling of sintered sample and once again microcracking resulted in lowering of strength and toughness (σ_f = 88.7 MPa, K_{IC} = 1.9 $MPam^{1/2}$, H_V = 7.9 GPa). The initial stage densification mechanism of these composites was studied from non-isothermal and isothermal sintering behavior. The densification was controlled by volume diffusion with the activation energy for densification being 236-258 $KJmol^{-1}$.

Retention of metastable *t*-ZrO_2 at room temperature is an important factor for achieving higher strength and toughness of the composites. Since, only a small fraction of t-ZrO_2 (10-15 vol%) could be retained in Al_2O_3-undoped ZrO_2, it was decided to use Y_2O_3 as a stabilizer for t-ZrO_2. Four different mole percent of Y_2O_3 (1.0, 2.0, 2.5 and 3.0 mol%) were added to separate batches of $Al(NO_3)_3$-$ZrOCl_2$ mixed solution, followed by precipitation and washing of the precipitated powder using modified ROUTE 4. The *t*-ZrO_2 retention (measured on the sintered surface) was 100% at 3 mol% Y_2O_3 addition, 97% for 2.5 mol% Y_2O_3 and only 14% for 2 mol% Y_2O_3 which further decreased at 1.0 mol% Y_2O_3 . The sintered density was also high (>94%) at 2, 2.5 and 3.0 mol% Y_2O_3 doped Al_2O_3-ZrO_2 composition while it was low for 1 mol% Y_2O_3 doped Al_2O_3-ZrO_2. Nearly 100% relative density could be attained in Al_2O_3-3Y-ZrO_2 sintered composites. The positive effect of high sintered density and high t-ZrO_2 retention reflected in the improved mechanical properties of the composites. The highest fracture strength was 650 MPa (in 3 point bending) and 350 MPa (in bi axial flexure) for Al_2O_3-3Y-ZrO_2 composites. The fracture toughness was 8.5, 9 and 13.04 $MPam^{1/2}$ respectively for Al_2O_3-2Y-ZrO_2, Al_2O_3-2.5Y-ZrO_2 and Al_2O_3-3Y-ZrO_2 composites sintered at 1600°C. The zone depths (measured from ground surface XRD pattern) for Al_2O_3-2.5Y-ZrO_2 and Al_2O_3-3Y-ZrO_2 composites were 2.99 and 4.69 µm respectively. The contribution of transformation toughening (ΔK_{ICTT}) for the above two composites were calculated using Mc Meeking and Evans model and was found to be 7.36 and 9.21 $MPam^{1/2}$ respectively. These findings suggested that some additional toughening mechanism was also operative in these composites. FE-SEM images show the presence of both intergranular and transgranular cracks in Al_2O_3-3Y-ZrO_2 samples. HR-TEM image suggests that YAG ($Y_2Al_5O_{12}$) has formed at the Al_2O_3-ZrO_2 grain interface. The presence of YAG increases the grain boundary fracture energy thereby modifying the crack propagation path from intergranular to transgranular. The indent surface image shows significant deviation of main crack from its original path, crack bowing around an obstacles, and crack branching. All these effects probably combined to give high strength and toughness of Al_2O_3-Y-ZrO_2 composites. Thermal shock resistance of Al_2O_3-3Y-ZrO_2 composites was also studied by air quenching method. For ΔT up to 1000°C, significant fracture toughness (K_{IC} = 7.28 $MPam^{1/2}$) and strength (σ_f = 547 MPa) could be retained in the quenched composites. This hints at good thermal shock resistance of the composites. The evaluated properties of Al_2O_3-3Y-ZrO_2 composites suggest that it may be used as a cutting tool material.

Key words:

Al_2O_3- 50 vol% ZrO_2 Composites, Powder processing, Solution chemistry route, Powder characterization, Sintering kinetics, Grain growth, Al_2O_3-Y-ZrO_2 composite, Hardness, Fracture strength, Fracture toughness, Microstructure, Thermal shock resistance, Cutting tool.

ACKNOWLEDGEMENTS

I thank my advisors Prof. Santanu Bhattacharyya and Prof. Swadesh Kumar Pratihar for their guidance and timely suggestion as well as critical comments for improving the thesis quality.

I am ever grateful to Pratihar Sir who played the major role in winding of this thesis. I never felt him as my teacher instead an elder brother to me. He resolved most of the critical situation during my work as well as my thesis writing.

My sincere thanks to Prof. J. Bera and Prof. D. Sarkar for appraising my work critically. My overwhelming thanks to Prof. R. Mazumdar, Prof. B. B. Nayak, Prof. S. Pal for their continuous encouragement.

I would also like to acknowledge the Department of Science & Technology, in India for financially supported for this project. The IIT Mumbai KRISS, South Korea and Nanocentre IISc Bangalore for permitting me to carryout out the microstructural studies (TEM, FE-SEM) of my samples. I would also express my sincere thanks to the laboratory technicians of Department of Ceramic Engineering and Material Science, N.I.T., Rourkela, especially P. K. Mohanty, U.K. Sahoo and R. Pattanaik for constant practical assistance and help whenever required.

To all my friends who amicably all been there for me like Sunil, Pankaj, Saroj, Vamsi, Subrat, Susanta, Ayas, Yuga, Kiran, Sarat, Atanu, Deepak, Helen for helping me throughout the difficult times, and for all the emotional support, camaraderie, entertainment, and caring they provided. As well as to my best friend Leizl for her extraordinary and unconditional support and patience from my triumph and failures in life.

Above all, I wish to thank my entire family especially my parents, brothers, half-siblings, my sister-in-law, nephew and niece who shaped my personality and influenced my priorities and molded me to pursue my engineering career and PhD course. My father and elder brother who always encouraged me to explore my knowledge, ability and skills since the time I joined this programme in 2004.

I thank to Lord Siva for this blessed life and affiliated the people who make me capable for accomplishment of this thesis.

Raghunath Prasad Rana

LIST OF FIGURES

Fig. No **Figure Caption** **Page No**

Chapter I - Introduction

Chapter II - Literature Review

Chapter IV - Experimental Work

Chapter V - Results and Discussion

Chapter VI - Results and Discussion – Al_2O_3-Y-ZrO_2 Composites

LIST OF TABLES

Table No **Table Caption** **Page No**

Chapter I - Introduction

Chapter II - Literature Review

Chapter V - Results and Discussion

Chapter VI - Results and Discussion – Al_2O_3-Y-ZrO_2 Composites

Chapter I

Introduction

Introduction

Ceramics have been known to mankind since the earliest civilization and have played an important role in the evolution and development of human civilization. Generally ceramics are defined as solid crystalline materials composed of oxides, carbides, nitrides, borides having important structural, mechanical, thermal and electronic properties. Most of the ceramic materials have significant fraction of covalent bonding which ensures improved high temperature properties like high melting point, strength at high temperature etc. The improved high temperature mechanical properties, coupled with high wear, oxidation and chemical resistance makes it suitable for many advanced and strategic applications such as ceramic bearings and grinding media, automobile parts, turbine plates, radomes, space shuttle tiles, ceramic armors etc. [1.1]. However, brittle fracture along with low Weibull modulus makes ceramics vulnerable for many advanced applications. There have been numerous efforts to reduce the brittleness and to improve the Weibull modulus of ceramics. Among these, composites have been found to be most successful in overcoming many of these shortcomings. Both metals and nonmetals have been successfully used as reinforcing materials either as particles, platelates, whiskers or fibers. The strengthening and toughening arises due to load transfer or various crack deflection mechanisms. The difference between the matrix and the reinforcement modulus as well as the nature of interfacial bonding becomes the deciding factor for determining the extent of strength and toughness improvement [1.2].

However, another class of composites exists where the toughness is achieved through controlled phase transformations of the reinforcement. These phase transformations are usually stress and/or temperature assisted and involve volume, shape or coordination change and usually occur by a combination of shear and rotation mechanism [1.3]. Ceramic composites utilizing these phase transformation are known as Transformation Toughened Ceramics. Table 1.1 lists some of these materials exhibiting shear type phase transformation involving large volume changes and some of these materials have been used for toughening of the host ceramic matrix.

As seen from Table 1.1 the reverse phase transformation of the ZrO_2 (t-ZrO_2 to m-ZrO_2) involves a volume expansion of 4-6 % and shear strain of 7-10%. Thus t-ZrO_2 has been used to toughen many ceramic matrices like Al_2O_3, SiC, mullite etc. These ZrO_2

containing composites are known as zirconia dispersed ceramics (ZDC) or zirconia toughened ceramics (ZTC) [1.3]. Since, the improvement in strength and toughness in these ZDC or ZTC results from the volume expansion and shear strain arising from $t \rightarrow m$ ZrO_2 transformation, it is important that t-ZrO_2 is retained at room temperature as a metastable phase. The retention of t-ZrO_2 at room temperature depends on many other factors namely the size of ZrO_2 particles, the matrix elastic modulus etc. [1.4]. A smaller particle size of ZrO_2 along with high matrix modulus provides the activation energy barrier against spontaneous $t \rightarrow m$ ZrO_2 transformation [1.5, 1.6]. Thus ideally, the elastic modulus of the matrix material should be much higher than that of ZrO_2 for utilizing the transformation toughening phenomenon.

Table 1.1 Shear transformations in nonmetallic substances [1.3]

Inorganic Compound	
Alkali Halides (MX)	($NaCl_{-cubic} \leftrightharpoons CsCl_{-cubic}$)
Ammonium Halides (NH_4X)	
Nitrates	
$RbNO_3$	($NaCl_{-cubic} \leftrightharpoons$ rhombohedral $\leftrightharpoons CsCl_{-cubic}$)
$TiNO_3$, $AgNO_3$, KNO_3	(Orthorhombic ⇋ rhombohedral)
Sulfides	
MnS	(Zinc blende-type $\leftrightharpoons NaCl_{-cubic}$)
BaS	($NaCl_{-cubic} \leftrightharpoons CsCl_{-cubic}$)
Dicalcium silicate ($2CaO.SiO_2$)	(Orthorhombic ⇋ monoclinic)
Minerals	
Pyroxene silicates	
Enstatite ($MgSiO_3$)	
Wollastonite ($CaSiO_3$)	(Orthorhombic ⇋ monoclinic)
Ferrosilicate ($FeSiO_3$)	(monoclinic⇋ triclinic)
Olivine ⇋ spinel ($[Mg,Fe]_2 SiO_2$)	(Orthorhombic ⇋ monoclinic)
Quartz (SiO_2)	(Orthorhombic ⇋ cubic)
	(Rhombohedral⇋ hexagonal)
Ceramics	
Boron nitride	(Wurtzite-type ⇋ graphite-type)
Carbon	(Wurtzite-type ⇋ graphite)
Zirconia (ZrO_2),HfO_2)	(Tetragonal ⇋ monoclinic)

Alumina is an important structural ceramic material having many desirable properties like high melting point (2046 ±5°C), hardness (18 GPa), elastic modulus (380 GPa) and excellent resistance to acids and alkalis. It is being widely used as grinding media, textile thread guides, in paper manufacturing industry, cutting tools etc [1.7]. However, it is brittle and has very low resistance to crack propagation i.e. low fracture toughness which results in catastrophic failure of the components. Among the several approaches that have been used to inhibit the catastrophic failure of alumina ceramics, toughening by incorporating *t*-ZrO_2 in the alumina matrix has been very successful.

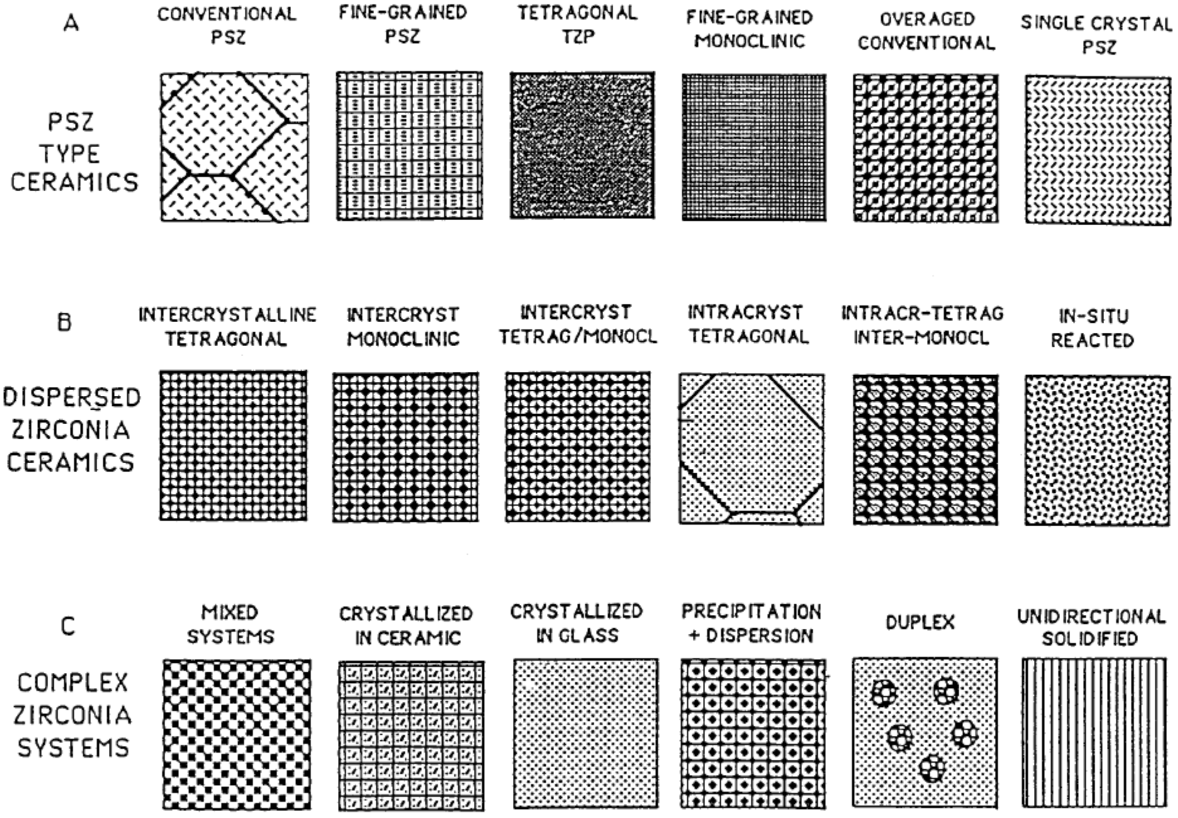

Fig.1.1 Classification of zirconia based ceramic composites [1.9]

These reinforcements make use of different energy absorbing mechanism (such as crack deflection, crack branching or crack bowing) which becomes operative in the stress field of an advancing crack tip. The mechanisms result in a process zone surrounding the main crack in which the crack tip stress intensity reduces, thereby arresting the propagation of the main crack. Moreover, the volume expansion due to the phase transition in the frontal zone exerts a back stress to the crack tip and it may also provide the crack closure forces in the fully developed wake region thereby obstructing the propagation of the advancing crack front by applying crack closer forces. The study of Al_2O_3 - ZrO_2 system is also of interest as both pure oxide systems contain a multitude of metastable phases that can be beneficial in many applications [1.8]. The commercially available Al_2O_3 - ZrO_2 composite are either known as Alumina Toughened Zirconia (ATZ) or Zirconia Toughened Alumina (ZTA) depending on whether ZrO_2 or Al_2O_3 is the matrix phase. Figure 1.1 gives a classification of the different types of zirconia toughened ceramics [1.9].

Recently, Nihara [1.10] has classified the ceramic matrix composites into four different categories (Fig. 1.2) on the basis of the matrix and reinforcement particle size. These are intra-type, inter-type, intra/inter-type and nano/nano-type. These nanocomposites show improved properties both at room temperature and at high temperature. The hybridization of both micro-nano composites is expected to give further improvement. However the synthesis of nanomaterials for bulk production is difficult due to grain growth of initial fine particles, introduction of processing related process flaws during initial sample preparation and handling of materials on its original dimension till the final microstructure development. The different type of ZrO_2 based composites which have been discussed above can also be grouped into these four categories as outlined by Nihara depending on their grain size, position (inter or intra granular) and uniformity of dispersion etc. The localized residual tensile strain around the particles induces transgranular fracture and the toughening occurs by the crack tip deflection. Thus, if the composite can be made into a nano/nano or a nano/micro type, additional improvement in strength and toughness can be expected because of the change of fracture mode of the composite which act to deflect or stop the crack propagation.

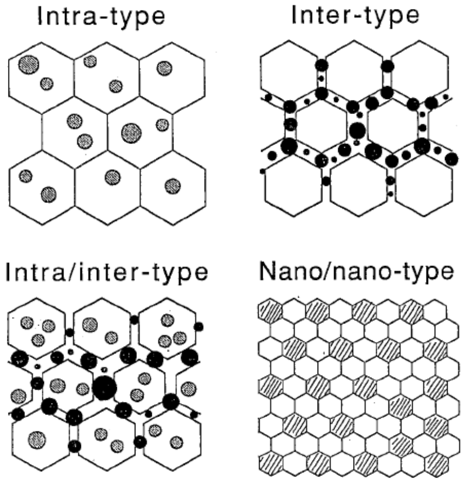

Fig. 1.2 Schematic representation of microstructural features of various nanocomposites as well as nano/nanocomposites [1.10]

In ATZ, usually low volume/weight fraction of ZrO_2 is incorporated in Al_2O_3 matrix. The increase in strength and toughness can be either due to transformation toughening or due to microcrack toughening [1.6, 1.9]. In the former case, high elastic modulus of Al_2O_3 helps to retain metastable t-ZrO_2 phase. Subsequently these metastable t-ZrO_2 particles undergo stress induced $t \rightarrow m$ ZrO_2 transformation in the stress filed of an advancing crack tip. The transformation toughening - considered as a crack-shielding mechanism is related to the process zone development. When the process zone is only ahead of the propagating crack, the toughness increment will be zero due to the absence of a fully developed wake region [1.11-1.13]. The maximum toughness increment occurs when the transformation zone fully extends over the crack surface. The contribution of toughness increment resulting from the stress induced toughening depends on toughening mechanism [1.11]. The general expression for the toughness increment is given by

$$\Delta K_{IC} = \frac{\eta E^* e^T V_f \sqrt{h}}{(1-\nu)} \tag{1.1}$$

where, ΔK_{Ic} is the toughening increment, V_f is the volume fraction of transformable ZrO_2 particles, e^T is the dilatational strain, E^* is effective modulus of the composite, h is the width of the transformed zone, ν is Poisson's ratio and η is a numerical constant which depends on the zone shape at the crack tip and the nature of the stress field in that zone (this particular point has been further elaborated in Chapter II during the discussion of transformation toughening models). The factors which controls the relative toughness of the precipitate and particulate-toughened systems are V_f, e^T and E^* because ν is about the same for both classes of material. Higher matrix modulus constrains the transformation, thereby decreasing the extent of the transformation zone depth h. The decrease in h is due to the lower fraction of t-ZrO_2 available for transformation. This restricted transformation situation arises either in very high modulus matrix or due to the presence of stabilizers. The elastic modulus of the composite will increase with increasing alumina content as the Young's modulus of alumina (380 GPa) is almost twice than that of zirconia (210 GPa). The high matrix modulus also causes a lowering of M_S temperature which further helps in t-ZrO_2 retention [1.14, 1.15]. Elaborate discussion on this mechanism can be obtained in the classical works of Claussen [1.9], Becher et al. [1.16] Evans et al. [1.17] Rühle et al. [1.18], Lange [1.19] and others.

In the second method, unstabilized ZrO_2 (m-ZrO_2) is introduced in Al_2O_3 matrix. As the composite is cooled down from the sintering temperature, the reverse $t \rightarrow m$ transformation takes place spontaneously which cause microcracking of the matrix. These microcracks either dilate by absorbing the crack tip stress or can deflect the propagating crack thereby dissipating the crack energy. This toughening mechanism is known as microcrack toughening. However, this toughening mechanism may not always cause a synergetic increase in strength [1.20].

Stabilization of the tetragonal ZrO_2 using dopants like MgO, Y_2O_3, and CeO_2 helps to retain t-ZrO_2 at room temperature even when the particle size is large, i.e. the dopants increase the critical particle size range for spontaneous transformation. Thus it becomes easy to tailor the toughness by controlling the extent of stress induced $t \rightarrow m$ transformation. The critical volume fraction of ZrO_2 required for the peak toughness depend on zirconia particle size. The fracture toughness, strength and hardness of sintered ceramics increase with the transformable tetragonal phase retention and are maximum when the crystallite size reaches the critical value for stress induced transformation. In this respect, care must be taken to optimize the sintering temperature and amount of stabilizer added since the matrix is required to reach the high density in order to provide the necessary matrix constraint to zirconia particles.

The key factors that decide the achievement of optimum fracture toughness and strength of ATZ and ZTA are volume/weight fraction of ZrO_2, particle size of ZrO_2, amount of stabilizer - which determines the transformability and degree of mixing (this depends on powder synthesis). These factors can be controlled during powder processing and green consolidation of the ATZ/ZTA composites. In the sintered composites the factors are sintered density, grain size of Al_2O_3 and ZrO_2, position of ZrO_2 grains (intergranular or intragranular), shape of ZrO_2 grains, distribution of Al_2O_3 and ZrO_2 grains (homogeneous or agglomerated distribution), variation of stabilizer content within different ZrO_2 grains [1.21,1.22].

Homogeneous distribution of ZrO_2 grains in Al_2O_3 is the most desirable microstructural feature of an Al_2O_3-ZrO_2 composite. However, in reality, processing difficulties do cause clustering/agglomeration of ZrO_2 particles. The ZrO_2 clusters grow to large grains during sintering which not only cause densification problems but also reduces t-ZrO_2 retention as the agglomerated ZrO_2 causes spontaneous $t \rightarrow m$ transformation thereby lowering the strength and toughness of the composite. The above problem becomes more pronounced at higher ZrO_2 content. This may be one reason why Al_2O_3-ZrO_2 composites have not been studied extensively 35-40 vol% ZrO_2 addition. Secondly, due to lower elastic modulus of ZrO_2 (E = 210 GPa) with regard to that of Al_2O_3 (E = 380 GPa), the overall elastic modulus is lowered quite significantly at higher ZrO_2 content. This factor also adversely affects the retention of t - ZrO_2 in the alumina matrix and thus the overall toughness increment.

Depending on the volume fraction of zirconia added to Al_2O_3, the composites that has been studied till now can be classified into two broad categories viz. (i) ZTA with ZrO_2 fraction typically up to 20-30 vol% ZrO_2 dispersed in Al_2O_3 and (ii) ADZ with low fraction of Al_2O_3 (10-20 vol %) distributed in ZrO_2 matrix. However, research have been rather limited on the composites having higher volume fraction of ZrO_2 (>30 vol %) in Al_2O_3 or more typically containing equal volume fraction of both phases. One school of thought opined that the toughness and strength increment will not be significant due to possibly low amount of retained t-ZrO_2. It is predicted that the microstructure of such a composite will be heavily microcracked leading to low fracture toughness. People who disagreed with this theory were of opinion that retention of t-ZrO_2 may be possible if densification can be lowered to below that of the critical transformation temperature. It is further suggested that M_s temperature can be considerably reduced by controlling the dopant type and amount. The combined effect of smaller grain size and stabilizing oxide may act to retain t-ZrO_2 even in high or equal volume fraction of Al_2O_3-ZrO_2 composites. The other possible objection for Al_2O_3-high ZrO_2 composites is the increased softness (ZrO_2 is softer) of the composites due to the higher amount of ZrO_2 and this factor may limit its use as a structural ceramics. However, while accepting the fact that the overall hardness of the composites will be lowered due to higher ZrO_2, the situation is expected to change once the ZrO_2 undergoes stress induced $t \rightarrow m$ transformation and the matrix may be became hard. Thus, in the light of the above discussion, it may be summarized that the study of Al_2O_3-ZrO_2 containing equal volume fraction of Al_2O_3 and ZrO_2 (with ZrO_2 in both unstabilized and stabilized form) may prove interesting both from understanding the transformation behavior as well as from property upgradation view point. One more obstacle which may become critical is the microstructural coarsening or clustering of ZrO_2 at high ZrO_2 loading which may change the ZrO_2 grain size. But at this stage, it is presumed that if solution chemistry routes are adopted for the processing these composites, many of the above mentioned difficulties may be tackled.

The processing routes adopted for fabricating the Al_2O_3-ZrO_2 composites do play a vital role in deciding the final properties of the sintered composites. It has been reported that the addition of ZrO_2 in Al_2O_3 reduces the grain growth tendency of Al_2O_3 but it also affects the compact sinterability. Lange [1.23] observed that the densification behavior of the Al_2O_3-ZrO_2 composite depend on the pore coordination number which in turn depends on the volume fraction of ZrO_2 and its packing behavior. It has been reported that the uniform distribution of Al_2O_3 and ZrO_2 can be achieved if the starting particle size of both Al_2O_3 and ZrO_2 is very small (nano range). Fine starting particle sizes can also give rise to several other advantages: (i) it can cause high packing density if agglomeration tendency can be controlled, (ii) finer particle size can considerably reduce the sintering temperature and increase the sintered density, (iii) dense fine grained microstructure can give rise to super plastic effect in the composites. However, all the above advantages could be realized if the agglomeration behaviour could be controlled and high density of the composite could be achieved. Extensive research has been carried out on the agglomeration tendency of fine powder of Al_2O_3 and ZrO_2 [1.24] which cites the importance of processing routes, nature of the solvents on the agglomeration behavior etc.

Presently, submicron or nano size Al_2O_3-ZrO_2 composites are mainly processed through solution chemistry routes like sol-gel [1.25], combustion synthesis [1.26-1.27], coprecipitation [1.28], gel-precipitaion [1.29], slurry compaction [1.30] etc.

Although these individual routes have subtle variations as dictated by their precursors, mixing techniques, processing conditions etc, all of them use solution based precursors for intimate mixing and aim to produce a homogeneous mixture of sub-micron or nano size materials. In many cases, the initial mixture is found be amorphous or partially crystallized. The use of solution precursors not only ensures homogeneous mixing at the molecular level but it also ensures crystallization of fine particles. Such powder due to its extremely high surface area have high reactivity and if properly densified can give rise to a nano structured composites provided post processing problems can be successfully tackled. Further, it is also observed that because of intimate mixing of precursors in the solution stage, powder prepared through these routes show many metastable phases which are absent in the powder prepared through conventional solid state routes and these metastable phases play crucial role in determining the final microstructure and hence the final properties of the sintered composites [1.31].

On the negative side of the solution chemistry route, it is often noted that the residual anions affect the phase evolution, agglomeration behaviour and sinterability of the powder. Residual chloride ions reduce the crystallization temperature of the powder. However, they go off at very high temperature leaving behind large voids which reduces the final sintered density. For this reason, chloride precursors need some extra post precipitation processing steps for overcoming the densification problem [1.32]. Nitrates, sulphates, and citrates precursors similarly have their characteristic problems.

Summarizing the above discussion, it can be said that the optimization of the microstructure – mechanical properties of Al_2O_3-ZrO_2 composites depends both on the characteristics of the starting powder, the fabrication and densification route that will be adopted for shaping and densification of the composites as well as on the type of precursors that are being used for powder processing.

Therefore, the present work proposes to study the processing and characterization of Al_2O_3-ZrO_2 (50:50 v/v) composites. The effect of precursors and post precipitation processing (washing) on the phase evolution, tetragonal ZrO_2 retention and densification behavior will be studied along with mechanical properties like strength, toughness and hardness. Optimization of microstructure and properties will be carried out through controlled processing, optimized sintering schedule and the use of Y_2O_3 as stabilizer for

ZrO_2 for fine tuning the mechanical properties. In the light of the above discussion, the entire problem has been elaborated in five different chapters besides this chapter.

The literature on ZTA and related materials is discussed in Chapter II. The chapter begins with a general review on the different transformation mechanism involving zirconia (ZDC, ATZ and ZTA) and the different transformation models available, followed by the different powder processing routes that are adopted for processing of ZDC, ATZ and ZTA, their relative advantages and disadvantages, the importance of post precipitation washing on the densification behavior during sintering. This is followed by the literature on sintering behavior, sintering models, the role of Al_2O_3, residual ions and pore coordination number etc on the densification mechanism of ZDC, ATZ and ZTA ceramics. The chapter ends with a detailed literature review discussing the mechanical properties-microstructure relationships in different of ZDC, ATZ and ZTA ceramics.

Chapter III elaborates the work plan and methodology for carrying out the proposed study.

Chapter IV discusses the experimental procedure and the different experimental parameters involved during powder processing, densification of the composites as well as mechanical property evaluation (strength, toughness, hardness, thermal shock resistance) of Al_2O_3 - ZrO_2 composites and microstructural studies.

Chapter V discusses the results and the related discussions involving the processing of Al_2O_3-ZrO_2 composites (with undoped ZrO_2). The chapter clearly demonstrates why precipitation route for powder preparation is better than gelation route, the adverse effects of chloride ions and the advantages of water/ alcohol washing on the agglomeration behavior and sintered density. The chapter also discusses the advantages of using nitrate precursors and the reasons for not retaining higher amount of *t*-ZrO_2 in the sintered composites. The isothermal and non isothermal densification behavior and the mass transport mechanism of Al_2O_3-ZrO_2 composites (with undoped ZrO_2) during the initial stage of sintering have been discussed. The effects of Y_2O_3 doping on the sintering mechanism, density and *t*-ZrO_2 retention have also been separately discussed.

Chapter VI discusses the effect of Y_2O_3 doping on the strength, toughness and hardness of ZTA composites. The correlation between microstructure and properties is also elaborated and the effect of grain boundary phase on the crack propagation behavior is also discussed. At the end, the thermal shock resistance behavior of some selected ZTA compositions has also been discussed.

Chapter VII summaries the results of the present investigations with the possible directions for future work.

References

1.1 D.W. Richerson, “The Magic of Ceramics”, Wiley- American Ceramic Society., USA (2000).

1.2 W.E. Lee and M. Rainferth, “Ceramic Microstructures: Property Control by Processing”, Chapman and Hall, Great Britain, 67-121 (1994).

1.3 D.J.Green, R.H.J. Hannink, M.V. Swain, “Transformation Toughened Ceramics”, CRC Press, Boca Raton, FL, 1989.

1.4 A.H. Heuer, and L.W. Hobbs (Eds),“Advances in Ceramics Science and Technology of Zirconia”, American Ceramic Society., Columbus, OH, 1981

1.5 R.C. Garvie, R.H.J. Hannink and R.T. Pascoe, “Ceramic Steel?” Nature (London), 258, 703-704(1975).

1.6 A.H. Heuer, “Transformation Toughening in ZrO_2 – Containing Ceramics”, J. Am. Ceram. Soc., 70, 689-698 (1987).

1.7 E. Dorre and H. Hubner, “Alumina processing, properties and Applications”, Springer-Verlag, Heidelberg, (1984).

1.8 D. Sarkar, “Synthesis and Thermo – Mechanical Properties of Sol – Gel Derived Zirconia Toughened Alumina Nanocomposite”, Ph.D. Thesis, N.I.T, Rourkela, 2006.

1.9 N. Claussen, “Microstructural Design of Zirconia Toughened Ceramics (ZTC)”, Advances in Ceramics, Vol. 12, Science and Technology of Zirconia II, American Ceramic Society, Columbus, OH, 1985, pp 325-351.

1.10 K. Nihara, “New Design Concept of Structural Ceramics: Ceramic Nanocomposites”, J. Ceram. Soc, Jpn 99, 974-982 (1991).

1.11 R.H.J. Hannink, P.M. Kelly and B.C. Muddle, “Transformation toughening in Zirconia-containing Ceramics”, J. Am. Ceram. Soc., 83 [3], 461-487(2000).

1.12 B. Bndiansky, J. Hutchinson and J. Lambropoulos, “Continum theory of dilatant transformation toughening in ceramics”, Int. J. Solids Struct., 19, 337- 355 (1983).

1.13 A. G. Evans, “Transformation Toughening: An Overview”, J. Am. Ceram. Soc., 69, iii (1986).

1.14 R.M. Mc Mecking and A.G. Evans, “Mechanics of transformation toughening in brittle materials”, J. Am. Ceram. Soc, 65, 242-246 (1982).

1.15 B. Basu, J. Vlengels and O. Van DerBiest, “Transformation Behaviour of Tetragonal Zirconia: Role of Dopant Concentration and Distribution”, Mat. Sci. and Engg. A, 366, 338-347 (2004).

1.16 P.F. Becher, M.V. Swain and M.K. Ferber, “Relation of transformation temperature to the fracture toughness of transformation – Toughned Ceramics”, J. Mat. Sci., 22, 76-84 (1987).

1.17 A.G. Evans and A.H. Heuer, “Review – Transformation Toughnening in Ceramics: Martensitic Transformation in Crack – Tip Stress Fields”, J. Am. Ceram. Soc., 63, 241-248 (1980).

1.18 M. Riihle, N. Claussen and A.H. Heuer, “Microstructural Studies of Y_2O_3-Containing Tetragonal ZrO_2 Polycrystals (Y-TZP) ””, Advances in Ceramics, vol. 12, Science and Technology of Zirconia II, American Ceramic Society, Columbus, OH, 1985, pp 352-370.

1.19 F. F. Lange, “Transformation Toughening – Part 2: Contribution to fracture toughness”, J. Mat. Sci, 17, 235-239 (1982).

1.20 N. Claussen, Fracture toughness of Al_2O_3 with an unstabilised ZrO_2 dispersed phase”, J. Am. Ceram. Soc., 59, 49-51(1976).

1.21 R.H.J. Hannink and C.J. Howard, “Relationship between fracture toughness and phase assemblage in Mg – PSZ”, J. Am. Ceram. Soc., 71, 571-579 (1994).

1.22 B. Basu, “Toughening of yttria – stabilized tetragonal zirconia ceramics”, Int. Mat. Rev., 50, 239-256 (2005).

1.23 F.F. Lange, and M.M. Hirlinger, “Grain growth in two phase ceramics: Al_2O_3 inclusions in ZrO_2”, J. Am. Ceram. Soc., 70,827-830 (1987).

1.24 F. F. Lange, “Sinterability of agglomerated powders”, J. Am. Ceram. Soc., 67, 83-89 (1984).

1.25 J. Chandradass and M. Balasubramanium, “Sol-gel processing of alumina – zirconia minispheres”, Ceram. Int., 31, 743-748 (2005).

1.26 Y. Wu, A. Bandyopadhyay and S. Bose, “Processing of alumina and zirconia nano-powders and compacts”, Mat. Sci. and Engg. A 380 349-355 (2004).

1.27 S. Biamino, P. Fino, M. Pavese and C. Badini, “Alumina – zirconia - yttria nanocomposites prepared by solution combustion synthesis”, Ceram. Int., 32 509-513 (2006).

1.28 S. Kikkawa, A. Kijima, K. Hirota and O. Yamaguchi, “Soft solution preparation methods in a ZrO_2-Al_2O_3 binary system”, Solid State Ionics, 151, 359-364 (2002).

1.29 V.K. Singh and R.K. Sinha, “Preparation of alumina by a combined precipitation and gelation Process”, *Mat. Lett.* 18, 201-206 (1994).

1.30 S. Dhara and P. Bhargava, “Influence of Nature and Amount of Dispersant on Rheology of Aged Aqueous Alumina Gelcasting Slurries” J. Am. Ceram. Soc. 88, 547-552 (2005)

1.31 M.L. Balmer, F.F. Lange, V. Jayaram and C.G. Levi, “Development of nanocomposite microstructure in ZrO_2-Al_2O_3 via the solution precursor method”, J. Am. Ceram. Soc., 78, 1489-1494 (1995).

1.32 C.E.Scott and J.S.Reed, “Effect of laundering and milling on the sintering behavior of stabilized ZrO_2 powders,” Am. Ceram. Soc. Bull., 58, 587-590 (1979).

Chapter II

Literature Review

Ever since the classical paper by Claussen [2.1] discussed the effectiveness of ZrO_2 in increasing the fracture strength of Al_2O_3, Al_2O_3-ZrO_2 compositions have been widely used for the last three decades. Immediately after Claussen, Lange [2.2-2.5] published a series of four papers which discussed the thermodynamics of constrained phase transformation with reference to critical size of ZrO_2 required for t-ZrO_2 retention, physics of transformation toughening leading to the increased fracture toughness of stabilized ZrO_2 containing composites as well as the validation of the theory with the experimental observation in Al_2O_3-ZrO_2 system. For the next three and half decades, numerous researches have been conducted on the different aspects of Al_2O_3-ZrO_2 composites. Owing to the density difference between Al_2O_3 and ZrO_2, the processing of Al_2O_3 and ZrO_2 has been of concern and extensive literatures are available on the different aspects of powder processing. The need for uniform dispersion of Al_2O_3-ZrO_2 composites have also been addressed by many researchers along with the different processing techniques adopted for achieving uniform dispersion. The mechanical properties, viz, strength, toughness and hardness, thermal shock resistance as well as aging behavior are controlled by microstructure and therefore many literatures are also available on this aspect. In view of the large numbers of available literature, in the present study, the available literature has been discussed under four different headings. These are transformation toughening mechanism, processing of Al_2O_3-ZrO_2 composites, densification behavior of Al_2O_3-ZrO_2 composites and finally microstructure and mechanical properties.

2.1 Transformation Toughening Mechanism

The basic idea behind the development of any transformation toughened ceramics is the retention of t-ZrO_2 in a metastable state and to ensure that this t-ZrO_2 undergo stress induced $t \rightarrow m$ ZrO_2 transformation in the stress field of an advancing crack tip at stress level not exceeding the material fracture strength. Thus this transformation acts as a crack shielding mechanism. These prerequisites are met through composition control, use of stabilizer for ZrO_2 (which shifts the critical particle size for t-ZrO_2 retention to higher value) as well as by controlling M_S temperature closer to room temperature (this helps to prevent spontaneous $t \rightarrow m$ ZrO_2 transformation during cooling from the sintering temperature. For a single or a multiphase brittle ceramic material/composite, [2.6, 2.7] the fracture toughness is given by

$$\mathrm{K_{IC}} = \mathrm{K_o} + \Delta K_C \tag{2.1}$$

where, K_o is the matrix toughness and ΔK_C is the contribution to the toughness from various crack shielding mechanism [2.8]. In the case of zirconia dispersed ceramics (ZDC), the stress induced $t \rightarrow m$ ZrO_2 transformation may increase the toughness through a change in the transformation zone shape. The volume change (4-6%) and the strain energy associated with the above transformation generate a compressive strain field around the crack tip which acts to stop or retard the crack tip propagation. Further increase in toughness can be realized from the microcracking associated with the $t \rightarrow m$ ZrO_2 transformation, the associated strain energy and the crack deflection by microcracks [2.9].

The three principal crack shielding mechanisms operative in the ZDC or other tough ceramics are transformation toughening (ΔK_{CT}), transformation induced microcrack toughening (ΔK_{CM}) and crack deflection toughening (ΔK_{CD}) [2.10, 2.11]. The extent of contribution by each of the above mechanisms is controlled by the morphology, size, shape, volume fraction and distribution of ZrO_2.

Either the energetic or the mechanistic approach is used to understand and develop the transformation toughening behavior and the resultant change in overall toughness. Both the approaches assume that the starting material is isotropic and the transformation effect diminishes from the crack tip to the surface or bulk [2.12-2.14]. The contribution of stress induced phase transformation to the overall toughness is given

$$\Delta \mathrm{K_{CT}} = \frac{\eta \mathrm{E}^* e^T V_f \sqrt{h}}{(1 - \nu)} \tag{1.1}$$

where, η depends on the zone shape at the crack tip as well as on the nature of stress field, E^* is the effective modulus of the material, e^T is the dilation strain, V_f is the volume fraction of t-ZrO_2 actually transformed, h is the zone depth and ν is the Poisson ratio.

The effective matrix modulus E^* controls the extent of dilatational strain [2.12]. Matrix materials having a high elastic modulus (Al_2O_3) ($E^* \sim 380$ GPa, $\nu = 0.2$) is more effective in constraining the transformation ($E_{ZrO2} = 210$ GPa, $\nu = 0.3$). This factor although helps to retain ZrO_2 in tetragonal form but also opposes the stress induced $t \rightarrow m$ ZrO_2 transformation because the volume change has to work against a greater constraining force. In ZDC materials, although the room temperature toughness may be high, it decreases at high temperature due to the increased stability of t-ZrO_2 at high temperature. However, there are reports that some ZDC materials may retain high toughness at elevated temperature through additional toughening mechanism [2.15].

In most of the transformation toughed ceramics, strength is inversely related to toughness. Swain [2.16] observed that for achieving toughness > 8 MPa√m, the strength need to be sacrificed. It was noted that for $K_{IC} < 8$ MPa√m, the strength value is flaw controlled while for $K_{IC} > 8$ MPa√m, it is controlled by the extent of transformation toughening.

2.2 Transformation Toughening Models

The two widely accepted models are either based on linear elastic fracture mechanics proposed by Evans [2.10] and McMeeking [2.12] or based on energy changes or work of fracture model proposed by Budiansky et al. [2.13]. Evans [2.10] and McMeeking [2.12] considered that only the dilatational strain was effective during the transformation and within the transformation zone and that the transformation was uniform. However, the model proposed by Budiansky et al. [2.13] computed the energy balance analysis for the transformation with a dilatational strain as well as considering that the transformation strain is not uniform throughout the transformation zone. Budiansky et al. further suggested that both the models were equivalent once steady state cracking condition is reached. This assumption was later corroborated by Rose [2.17].

The other factor that can affect the toughness calculation using the two existing models is the degree and nature of transformation (i.e. whether supercritical or subcritical toughening).The supercritical transformation implies complete transformation taking place within the process zone and zero transformation outside the process zone. This kind of step function type transformation is probably unrealistic and a gradient in the volume fraction of transformed material across the process zone provides a more realistic picture of the actual transformation i.e. transformation is more likely to be subcritical [2.13]. Marshall et al. [2.18] and Yu et al. [2.19] have experimentally observed this type of transformation behavior in Mg-PSZ and Ce-TZP-Al_2O_3 system. From the toughness prediction view point, supercritical transformation overestimates the toughening and subcritical transformation (a more realistic assumption) results in reduction of predicted toughness by a factor of two. Budiansky et al. [2.13] also introduced a parameter “intensity of the transformation” defined as

$$\omega = \frac{1+\nu \mathrm{E} \mathrm{V}_{\mathrm{t}} e^{T}}{1-\nu \sigma_{\mathrm{T}}} \qquad (2.2)$$

where, E is the elastic modulus, ν is Poisson’s ratio, V_t is the volume fraction of transformed material, e^T is the transformation strain and σ_T is the critical stress required to initiate the transformation process. A large value of ω (>> 1) denotes intense or strong transformation which can be realized if the M_S temperature is close to the test temperature and only a small stress is required to initiate the transformation (σ_T is small).

Still another important factor which can affect the toughness prediction is the nature of transformation, i.e. whether it is pure dilatational, pure shear or a mixture of shear and dilatational. Table 2.1 provides the different values of η considering different strain couplings when dilatation model is considered. η is $0.214/(1-\nu)$ for supercritical transformation and it is $0.107/(1-\nu)$ for subcritical transformation. However, this type of strain conditions could not account for the experimentally observed toughness, which in many cases was higher by a factor two. Evans [2.20] proposed that both dilatational and shear transformation need to be operative to account for the experimental value of toughness and using this proposal Lambropoulos [2.21] suggested $\eta = 0.55$ [i.e., $0.385/(1-\nu)$]. Comparable values were obtained by other workers, a comprehensive list of which is provided in Table 2.1. The shape and size of the process zone also affects the toughness enhancement. Usually, three types of process zone are observed – underdeveloped, fully developed and partially developed. When the process zone remains only in front of the crack tip of the propagating crack, the main crack lies in the untransformed material. Under this condition, the application of load changes the zone shape similar to that of dilatational strain, which interacts only with the crack tip.

Table 2.1 Comparison of toughening model predictions with the value of η

Model	Transformation initiation stress	Transformation Strain (e^T)	Constant (η)
McMeeking and Evans	Hydrostatic	Volume change	0.214
Budiansky et al.	Hydrostatic	Volume change	0.214
Evans and Cannon	Shear bands	Volume change	0.38
Lambropoulos	Maximum principal stress	Uniaxial dilatation	~0.37
Lambropoulos	Volume change and reduced shear	Volume change and reduced shear	~0.22
Chen and Reyes-Morel	Shear and volume change	Volume change	0.48
Swain	Experimental	Volume change	0.45
Chen and Reyes-Morel	Experimental	Volume change	0.22-0.32

For such a case, integration of the tractions along the transformation zone boundary shows that ΔK_{CT} is zero and no toughening is observed due to the transformation effect (Fig. 2.1 a ,b) [2.21, 2.22]. When the transformation process zone fully encompasses the main crack (and not the crack tip only), it exerts closer tractions on both the crack surface and the zone boundary (Fig.2.1c, d). Integration of these tractions over the transformation zone gives the maximum toughness increment same that as Eqn. (2.1) However, when the transformation zone partially covers the crack, R-curve behavior is observed and ΔK_C increases with the increase in crack length (Δa), and the approximated ΔK_C is given by

$$\Delta \mathrm{K_C} \approx \left[\frac{0.44}{\pi(1-\nu)}\right] E e_T V_f \tan^{-1}\left(\frac{\Delta a}{h}\right) \tag{2.3}$$

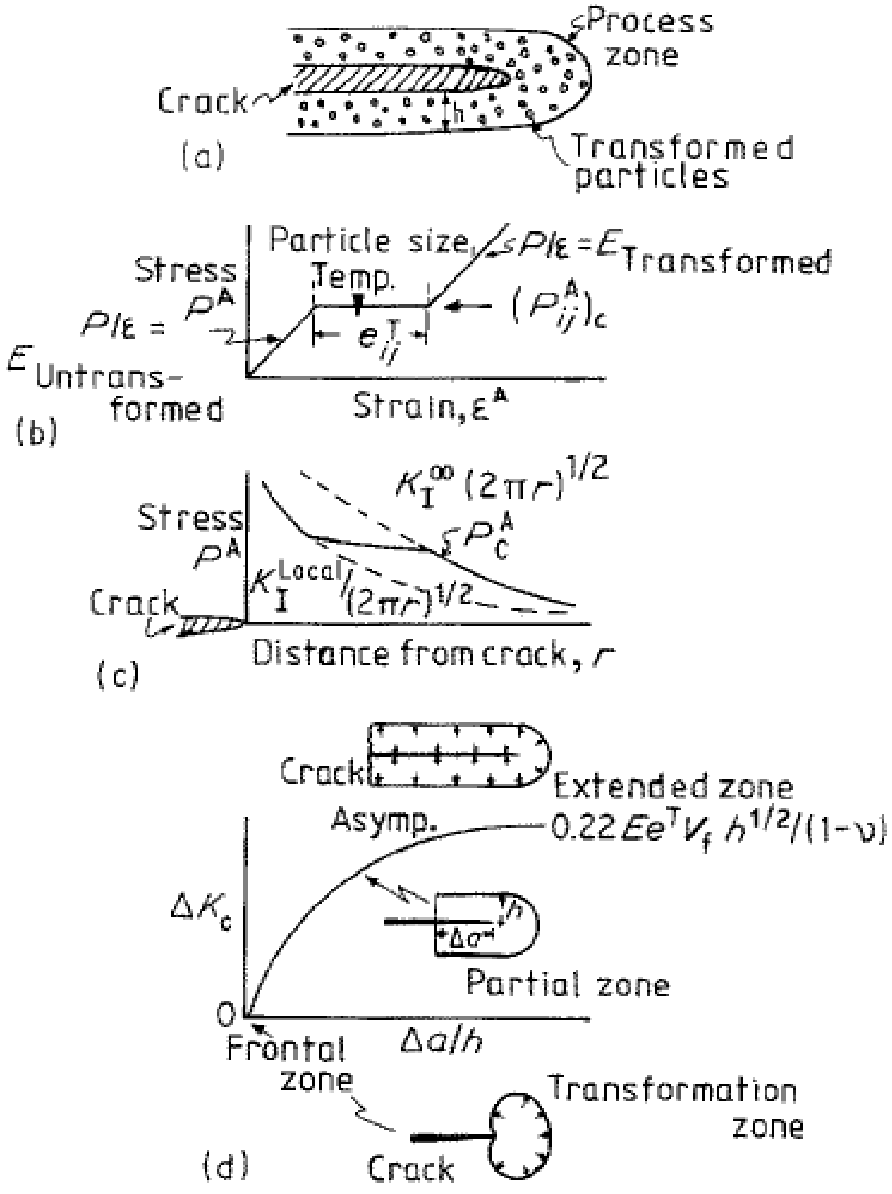

Fig.2.1. Schematic drawings of crack shielding mechanism by a transformation zone: [2.24]

In the end, it can be said that nature of transformation is dependent on material properties like grain size, dopant concentration, and volume fraction of ZrO_2 etc. and the theoretical prediction of toughness increment varies from model to model. However, closer matching of the theoretical and experimental toughness could be obtained for cases where the transformation was assumed to be subcritical and both shear and dilatant transformation strain was considered in the model.

2.3 Other Toughening Mechanisms for ZTA Ceramics

Besides transformation toughening two other toughening mechanisms are also effective for ZTA ceramics. They are toughening by crack deflection toughening through the generation of compressive surface layer, and other energy dissipating mechanisms.

2.3.1 Toughening by Crack Deflection

Localized residual stress fields are generated during any type of phase transformation involving volume change or due to thermal expansion mismatch between the two phases or arising from the fracture of a second phase. This residual stress field can deflect the main propagating crack thereby causing toughening of the composite. The extent of toughening depends on the reduction in the force on the deflected portion of the propagating crack. However, for crack deflection involving second phases particulates, the extent of deflection and thereby the toughness increment is dependent on the volume fraction of second phase particles, its morphology and aspect ratio [2.21-2.26].

2.3.2 Toughening by the Generation of Compressive Surface Stress

The compressive strains are generated during the volume expansion and shear strain developed during controlled $t \rightarrow m$ ZrO_2 transformation. The presence of these surface compressive stress (500 to 1000 MPa and concentrated in a depth of about 20 μm) acts to toughen and strengthen the ZTA ceramics because the crack has to overcome these compressive stresses before it can propagate. The compressive stress can be generated through various processes like grinding [2.25], impact [2.26] and low temperature quenching [2.27].

2.3.3 Toughening by other Energy Dissipating Mechanisms

The transformation twins due to $t \rightarrow m$ transformation and the associated coherency loss are energetic process and results in the lowering of crack tip stress intensity. This also can result in a toughness increment [2.9]. Usually, the stress induced transformation are irreversible in nature but under certain conditions the transformation becomes reversible

[2.2] on removal of the applied stress or in the wake zone. Rice [2.28] and Marshall [2.29] have noted that this transformation due to change of stress state can affect the extent of toughening in ZTA ceramics. Crack branching by secondary phase present in the matrix by the localized stress fields can also cause toughening effect. Wang [2.24] has noted crack branching effect in ZTA duplex structures, containing large PSZ or TZP agglomerates.

2.4 Toughening in Zirconia Toughened Al_2O_3 system

The two previous sections summarized the generalized toughening mechanisms in ZrO_2 and ZrO_2 based ceramics. In this section, the different toughening mechanisms operative in ZTA system has been briefly discussed. The main idea of introducing ZrO_2 in Al_2O_3 matrix is to increase the resistance to crack propagation or in the other words to increase the fracture toughness (K_{IC}). ZTA systems have been mostly used as grinding media, cutting tool inserts. The ZrO_2 has been introduced either as unstabilized ZrO_2 or as TZP. The toughening mechanisms that are operative in ZTA are stress induced transformation toughening, microcrack toughening as well as crack deflection. While the effect of stress induced transformation toughening and crack deflection on the toughness and strength are additive in the increase in toughness due to the combined effect of transformation, microcrack toughening may not cause a concurrent increase in strength. The decrease in strength in heavily microcracked ZTA is caused by a lowering of matrix elastic modulus. Evans [2.30] has discussed the characteristic features of crack shielding mechanisms exhibited by the nonlinearity in the stress – strain curve above a critical transformation stress (p_{ij}). At the transformation condition and within the transformation zone, the strain becomes discontinuous, which lowers stress state at the crack tip provided that the transformation strain has the same sign as that of crack tip. The lowering of crack tip stress causes crack shielding and helps to increase the fracture toughness.

2.5 ZTA Powder Processing

In the previous section, it has been elaborated that a uniform dispersion of ZrO_2 in Al_2O_3 matrix is required for significant improvement in strength and toughness of ZTA ceramics. An optimized processing route of sufficient quality ensures minimum density variation and small scale of the residual flaw population and absence of large scale porosity/flaws. These two factors result in a ZTA microstructure in which stress induced $t \rightarrow m$ transformation takes place during the crack propagation. Ideally, this calls for sufficient microstructural integrity for sustaining the stress level which is required for activating the $t \rightarrow m$ ZrO_2 transformation and necessitates a close control of processing parameters for achieving uniform dispersion of both the phases (Al_2O_3 and ZrO_2). The processing route also affects the morphology and size of ZrO_2 grains. Solid state route has been traditionally used to prepare the ZTA powder mix but the mixing is nonuniform (particularly at higher ZrO_2 loading) and may also cause segregation of Al_2O_3 and ZrO_2 due to wide difference in density. Chemical precipitation routes mostly ensure uniform mixing of Al_2O_3 and ZrO_2 at any concentration level, but it usually gives spherical and smaller particles which are usually difficult to transform. The other negative aspect of these routes is the tendency for hard agglomerate formation during powder processing and drying (due to the formation of Zr-O-Zr or Al-O-Al bonds). This hampers densification, which in turn affects the end properties. Other processes like alkoxide sol-gel, CVD or reactive processing has also been used and each of them has their specific advantages and disadvantages and depending on the desired properties or applications one or the other type of powder processing route are adopted by researchers. Besides powder processing, consolidation or shape forming method may also affect the microstructural integrity and the end properties. The function of the powder processing finishes at the powder stage itself, but even a homogeneous powder may not yield good properties due to problems in shape forming operations. Besides uniaxial dry pressing, the other major shape forming operations are cold isostatic pressing, slurry compaction, centrifugal casting, reactive hot pressing, hot isostatic pressing, spark plasma sintering etc. All of these different shape forming operations also aim to reduce the processing flaws as well as enhance the microstructural homogeneity and structural integrity. In this section, a summary of the literature on the different ZTA powder processing route as well as their shape forming results have been summarized.

The initial papers on Al_2O_3 – ZrO_2 composites were based on mixing of Al_2O_3 and ZrO_2 powders (solid state mixing). Usually two mixing methods – dry and wet mixing was being used. The wet mixing method generally produced a better dispersion and compositional homogeneity in comparison to dry mixing but the chances of segregation or agglomerate formation was higher in the latter case. However, due to ease of operation, till date, this method has been preferred by many researchers. Claussen [2.1] prepared Al_2O_3 – unstabilized ZrO_2 composite powder mix by wet mixing of Al_2O_3 and ZrO_2 in planetary mill. The wet slurry was dried and hot pressed in graphite die under vaccum at 1400^oC.

Lange [2.5] also prepared Al_2O_3-Y_2O_3(ZrO_2) composite containing different volume fractions of ZrO_2 by dry mixing of Al_2O_3 and ZrO_2 while yttrium nitrate was used for Y_2O_3. The powder mix was wet milled, dried and cold isopressed. The bars were sintered in air at 1400, 1500 and 1600^oC depending on the composition.

Liu et. al. [2.31] prepared Al_2O_3 - 2YTZP composites by ball milling a mixture of Al_2O_3 powder and hydrothermally prepared 2Y-TZP. The milled powder was calcined at 600^oC for 3 hours and sintered in air at 1450, 1550 and 1600^oC. Basu et al. [2.32] studied ZrO_2-Al_2O_3 (72:28 volume ratio) composites, where ZrO_2 was introduced either as Y-TZP or as a mixture of unstabilized ZrO_2 and Y_2O_3. The ZrO_2-Al_2O_3 powder mix was mixed in propanol medium. The composites were cold compacted and hot pressed at 1450^oC. Huang et al. [2.33] used solid state mixing to prepare Ce - TZP/Al_2O_3 composites.

Chemical synthesis routes like co-precipitation, chemical polymerization, destabilization of mixed sols, ammonolysis have been widely used for preparation of different single and bi-phasic composites. Debsikdar [2.34] prepared 80 Al_2O_3 – 20 ZrO_2(wt %) powders using three different processes like chemical polymerization, destabilization of mixed sols and co-precipitation. The primary particles were amorphous with sizes between 1.5 - 3 nm. The decomposition and crystallization behavior, surface area, pore size as well as tetragonal ZrO_2 retention was reported to be dependent on the synthesis chemistry. All the powders could be densified at 1200^oC. Chan et al. [2.35] prepared ZTA powder (15 ZrO_2/85 Al_2O_3 vol%) by co-precipitation route using $Al(NO_3)_3 \cdot 9H_2O$ and $ZrO(NO_3)_2 \cdot 2H_2O$. The precipitated gels were aged at room temperature for different time periods varying from 0.5 to 40 hours followed by washing with distilled water and ethyl alcohol. The desired composite powder was uniaxially compacted and sintered in air at 1550°C. Large number of intragranular ZrO_2 was observed in the as precipitated powder due to high grain growth of α-Al_2O_3. The aging treatment reduces the surface area and the grain growth rate was less. Thus most of the intragranular ZrO_2 was converted to intergranular ZrO_2 along with less number of entrapped pores.

Shi et al. [2.36] reported the processing of nano Y-TZP/Al_2O_3 composites obtained by co-precipitation from a mixed salt solution of Y^{3+}, Zr^{4+} and Al^{3+}. It was proposed that in the precipitated powder alumina existed as an amorphous phase within the Y-TZP lattice and later it crystallized as α-Al_2O_3. The presence of Al_2O_3 in the Y-TZP caused its lattice distortion due to which the crystallite growth of Y-TZP was slow.

Hong et al. [2.37] studied the crystallization behavior of Al_2O_3-ZrO_2 (20 mol %) solid solution powder prepared by co-precipitation method. $AlCl_3$ and $ZrOCl_2$ were used as the precursors. In the calcined gel powder, alumina crystallization followed the sequence bayerite $\rightarrow$ γ-Al_2O_3 $\rightarrow$ c-ZrO_2 + γ-Al_2O_3 $\rightarrow$ c-ZrO_2 + δ-Al_2O_3 $\rightarrow$ t-ZrO_2 + θ-Al_2O_3 $\rightarrow$ t-ZrO_2 + α-Al_2O_3. They concluded that the presence of ZrO_2 shifted the θ to α-Al_2O_3 transformation from 1100°C to 1300°C. It was also observed that the crystallization of c-ZrO_2 was influenced by the presence of Al^{3+} in ZrO_2 lattice.

Upadhyay et al. [2.38] studied the crystallization behavior of 3Y-TZP/Al_2O_3 (0-20 vol %) composite powder which were prepared by co-precipitation method using $ZrOCl_2$, $Y(NO_3)_3$ and $AlCl_3$ as the precursor. They observed that the presence of Al_2O_3 inhibited the crystallization of ZrO_2 and the shifting of the crystallization temperature was directly proportional to the Al_2O_3 concentration. It was further observed that the nucleation and growth of crystallites in the low temperature region (< 900°C), was interface controlled (inter agglomerate growth) involving short range migration of ions. At higher temperature (>900°C), the growth was intra-agglomerate type causing rapid densification of primary particles.

Enomoto et al. [2.39] made a process study of Al_2O_3-ZrO_2 (10 mol %) nano composite prepared by ammonolysis route. The mixed sol of Al_2O_3-ZrO_2 was prepared by adding $Al(NO_3)_3$ aqueous solution to a hydrolyzed ZrO_2 sol. Al_2O_3-ZrO_2 composite powder was precipitated (at pH 7) from the mixed sol via four different process (gaseous NH_3, concentrated NH_3 water (25%), diluted NH_3 water at 50°C and diluted NH_3 water at 70°C under N_2 atmosphere). It was observed that the gradual precipitation process using NH_3 gas (at 70°C) was preferable for avoiding the crystalline bayerite formation and for uniform dispersion of nano ZrO_2 particles in Al_2O_3 precursors.

Besides solid state mixing or precipitation, several investigators have also used aqueous solutions or sols of Al and Zr followed by either gelation or precipitation or by spray pyrolysis. These chemical routes often offer closer control over particle morphology and composition even in multicomponent oxide systems. A series of porous structure (meso & micro) can developed during the sintering process.

Low et al. [2.40] studied the crystallization behavior of gel derived alumina zirconia ceramics prepared from zirconium oxychloride and aluminium isopropoxide. The in situ gelation process allowed highly homogeneous structure. Zirconia accelerated the crystallization of transition alumina to corundum (α-Al_2O_3) through the formation of intermediate solid solution (γ-Al_2O_3 – 4 mol% ZrO_2). The microstructure was very fine and uniform which could be related to the microporous texture of gel structure.

Bala Gopal et al. [2.41] prepared Al_2O_3 – 10 wt% ZrO_2 and Al_2O_3- 5 wt% ZrO_2 powders using aqueous sols obtained through hydrolysis and peptization. The mixed sol was spray dried at a fixed inlet temperature of 175°C. The powders had spherical particles with narrow size distribution. The linear compaction response implied homogeneous powder and similar packing arrangement. Ceria addition was found to favor the densification of alumina.

Jayaseelam [2.42] used sol gel process to prepare three different series of alumina-zirconia compositions: (i) composites with unstabilized zirconia, (ii) composites with 12 mol% CeO_2 - stabilized zirconia and (iii) composites with 3 mol% Y_2O_3-stabilized zirconia of varying amount (5,10,15, 20 and 25 vol% ZrO_2). All the gel compositions were prepared using stable boehmite sol and oxalate of Zr, Ce and Y. It was noted that substantial amount of ZrO_2 remain dissolved in transition alumina lattice and during the transformation process of transition alumina to α-Al_2O_3 the zirconia comes out of the alumina lattice and enters the interstitial and vacant lattice sites causing expansion of the lattice along the *a*-axis. The Zr^{4+} exerts dragging force on Al^{3+} thereby shifting the α-

Al_2O_3 transition to higher temperature. Similarly, the presence of alumina grains provides a constraining force to the grain growth of ZrO_2 and it also helps to retain *t*-ZrO_2.

Chatterjee et al. [2.43] prepared Al_2O_3-ZrO_2 microspheres with Al_2O_3:ZrO_2 molar ratios as 87:13, 78:22, 74:26 and 64:36 by sol emulsion gel synthesis method. It was observed that the surfactant concentration and sol viscosity controlled the characteristics of derived microspheres. The gel crystallized at 900°C and retained some *t*-ZrO_2 even after sintering at 1600°C. The retention was related to the smaller grain growth of ZrO_2.

Lee et al. [2.44] studied the TEM microstructure of sol-gel synthesized Al_2O_3-50 wt% ZrO_2 (Y_2O_3) nano-composites. The composites were prepared through a sol-gel process using Al - sec butoxide and Zr-butoxide. The as prepared amorphous powder showed the normal $c \rightarrow t$ ZrO_2 transformation at 1200°C. However, due to the nano size powder, alumina remained in the amorphous state till 1050°C and converted to α-Al_2O_3 at 1200°C.

Chandradass et al. [2.45] prepared Al_2O_3- (5, 10 15 wt%) ZrO_2 composite microspheres by sol gel method using Al-tri-isopropoxide and $ZrOCl_2$. α-Al_2O_3 crystallization was shifted to 1290°C and the shift was attributed to the pinning effect of Zr^{4+} ions which came out of amorphous alumina during heating. While only α-Al_2O_3 and ZrO_2 was observed for Al_2O_3 – 5 wt% ZrO_2 composition, it was a mixture of α-Al_2O_3, *t*-ZrO_2 and m-ZrO_2 for 10 and 15 wt% ZrO_2 compositions. The appearance of *m*-ZrO_2 at higher ZrO_2 content was due to growth of ZrO_2 particles beyond the critical size.

Recently, Palmero et al. [2.46] has prepared Al_2O_3-ZrO_2 and Al_2O_3-YAG composite material by post doping of α-Al_2O_3 powder either with Zr-alkoxide or with yttrium methoxide respectively. The Al_2O_3-ZrO_2 composite had 95 vol% Al_2O_3 and 5 vol% ZrO_2. The synthesized powder was very fine and could be sintered at 1500°C for 3 hours.

Gilan et al. [2.47] prepared Al_2O_3-ZrO_2 (Y_2O_3) nano powders containing 5, 10, 15 wt% ZrO_2 by aqueous sol-gel method using Al—sec-butoxide and Zr-butoxide as precursors. An increase in ZrO_2 content reduced the powder surface area and it also shifted the transition alumina to α-Al_2O_3 temperature to a higher temperature.

Bhattacharyya et al. [2.49] have used a simple gel-precipitation method to prepare Al_2O_3-ZrO_2 (50 vol %) composites starting with inorganic precursors of $AlCl_3$ and $ZrOCl_2$. In this process, the concentration of the starting solution is increased to such an extent that during gelation process, when the gel becomes fully viscous, a substantial portion of the starting solute (or metal ions) are in solution. During the drying of gel, the solute precipitates out in the pores of the hydroxide network. In this process, the two cations may be precipitating at different rates between the hydroxide network and the liquid phase.

Colloidal processing is another important processing route which helps to achieve uniform dispersion of particles in single and multicomponent oxide systems. The particle dispersion is achieved by controlling the electroststic/electrosteric repulsion by changing the suspension pH. A homogeneous particle dispersion in suspension helps to improve the microstructure as well as the sintered density. In the following section, a summary of the available literatures on the colloidal processing of Al_2O_3-ZrO_2 is presented.

Novak et al. [2.50] correlated the electrokinetic properties of ZrO_2 to the rheology and microstructure of Al_2O_3-ZrO_2 suspensions. They observed that the adsorbed ions (CO_3^-, Cl^-) do affect the isoelectric point of both Al_2O_3 and ZrO_2 as well as of their mixed suspension. Washing/ageing of the ceramic particles prior to suspension making is expected to improve the dispersion and densification as well as the sintered microstructure.

Ramakrishnan et al. [2.51] noticed that due to the difference in pH range of stability of Al_2O_3 and ZrO_2, their mixed suspension exhibited heterocoagulation. Experimental results indicated while the suspension is stable either below pH 6; zirconia is stable either below pH 6 or above pH 8. For mixed suspension of Al_2O_3-ZrO_2, the suspension is unstable between pH 7 and 9. They concluded that at pH level where the surface charge is high enough to counter the vander waal attraction, the suspensions are stable and the reverse is true at pH level close to isoelectric point.

Suzuki et al. [2.52] studied the dispersion behavior of Al_2O_3-ZrO_2 suspension and observed that additional redispersion treatment like ultrasonication helps to produce dispersed suspension by preventing the agglomeration tendency of fine particles. Compacts prepared from ultrasonicated suspension (ultrasonication power 160 w) exhibited more that 55% elongation as a result of extremely fine and uniform microstructure resulting from colloidal processing.

Working with aqueous or nonaquous colloidal suspension allows one to go for complicated shaping. This particular aspect was studied by Daskobler et al. [2.53] who prepared ZTA composites with corrugated microstructure. They used non-polar suspension of alumina and zirconia of high solid loading for making thick Al_2O_3 and ZrO_2 tapes by tape casting. Corrugated composite structure was prepared by repeated rolling and folding of the stacked tapes.

Sarraf et al. [2.54] studied the fabrication of fine grained Al_2O_3-ZrO_2 composites through optimized colloidal processing. Highly dense and uniform sintered microstructure was obtained on sintering at 1510°C. The results suggested that the optimized rheological behavior of Al_2O_3-ZrO_2 suspension is likely to influence the microstructure of sintered Al_2O_3-ZrO_2 composites.

Combustion technique or solution combustion synthesis method uses the combustion of a redox mixture. The process is advantageous because (i) it is simple and can be up scaled easily, (ii) easier and faster (iii) with proper choice of fuel, α-Al_2O_3 can be obtained at a low temperature, and (iv) yields homogeneous powder mixture of high purity. An excellent review of different combustion processing and their applicability have been carried out by K. C. Patil et al. [2.55]. Following are the summary of the literatures on ZTA processing by combustion synthesis.

Wu et al. [2.56] reported the processing of nano powders of alumina and zirconia using sucrose as a chelating agent and using the corresponding metal nitrates as the precursors. The prepared powder was in the nano size range and had good sintered density. The authors commented that the sucrose template method could be applied to multicomponent nano oxide systems.

Biamino et al. [2.57] prepared nanostructured ZTA composites (Al_2O_3-20 vol% 3Y-TZP) by solution combustion route using urea as fuel. The authors tried a two step process in which firstly 3Y-TZP was obtained through the combustion reaction followed by dispersion of 3Y-TZP in a solution of $Al(NO_3)_3$ and urea which was then combusted for the second time. On the other hand, in single stage process, all the metal nitrates (Zr, Y, Al) were simultaneously added to prepare a mixed nitrate solution followed by the combustion in single step. They observed that in the single step processing a superior homogeneity of zirconia and alumina was achieved and it also allowed a higher retention of t-ZrO_2 at room temperature.

Kingsley et al. [2.58] developed a novel combustion process for the synthesis of α-Al_2O_3 and oxide materials including Al_2O_3-ZrO_2 composites. The authors used metal nitrates as the oxidizers and urea as fuel to produce ultrafine powders of Al_2O_3-t-ZrO_2 composites.

S.T. Aruna et al. [2.59] prepared nanocomposites through a modified solution combustion approach using a mixture of fuels. ZTA-1 was prepared from the corresponding metal nitrates and urea and had an average particle size of ~37 nm. ZTA – 2 was prepared from metal nitrates and a mixture of fuel (ammonium acetate, urea and glycine) with an average particle size of < 10 nm. It was observed that the above fuel mixtures changed the energetic of combustion reaction and the final properties of the composite.

Zhao et al. [2.60] prepared Al_2O_3-ZrO_2 (Y_2O_3) self growing composites prepared by combustion synthesis under high gravity condition (> 200g). The prepared ceramics had triangular dispersion of orderly nano-submicrometer t-ZrO_2 fibres, surrounded by either inter colony regions containing micrometer size –ZrO_2 spherical grains.

Kikkawa et al. [2.61] used two types of solution synthesis method for processing of (Y_2O_3) ZrO_2–Al_2O_3 binary system. In the first route, the precursors were yttrium chloride, zirconyl chloride, aluminium chloride with citric acid as fuel and the powder was prepared by combustion synthesis. In the second method, composites were prepared by coprecipitation of metal chlorides by freezing the mixed aqueous solution under microgravity. Microgravity was found to be effective in obtaining both good crystallinity and good mixing of metal salts precipitated from aqueous precursors.

Beitollahi et al. [2.62] studied the synthesis of Al_2O_3-ZrO_2 nanocomposite through a modified sol-gel route using sucrose, poly vinyl alcohol and metal nitrates. α-Al_2O_3 crystallized at 1200°C or above and t-ZrO_2 at lower temperature,

The available literature shows that ZTA are mostly prepared by one of the above discussed routes. Among them, sol-gel and co-precipitation have been commercially up scaled to prepare many ZTA components. Combustion synthesis has also become popular because of its certain distinct advantages in comparison to other solution based routes. However, two more routes (viz. hybrid route and hydrothermal route) have also been (and is being) used to process ZTA composites with properties comparable to those obtained by other routes and this review may remain incomplete without referring to those literatures.

Rao et al. [2.63] precipitated hydrous zirconia (from zirconyl chloride) on a suspension of Al_2O_3 for preparing ZTA composites. Subsequently, the composite powder was either slip casted (in the as prepared state) or it was calcined at 500°C followed by dry pressing. The compact from the as prepared powder did not undergo required coarsening and had lower strength after sintering.

Saha et al. [2.64] used the hybrid route to prepare Al_2O_3- Ce-TZP (10 vol%) composite. Ce-TZP was prepared from a sol containing Zr – n- propoxide and $Ce(NO_3)_3.6H_2O$. Al_2O_3 powder was coated by the zirconia sol and it was gelled, calcined compacted sintered at 1400°C. Fine integranular zirconia was observed in the Al_2O_3 matrix.

Rao et al. [2.65] processed Al_2O_3–ZrO_2 powders containing 15, 50 and 85 wt% Al_2O_3 via mixing of α-Al_2O_3 powder with $Zr(OH)_4$ gel. Their objective was to investigate the effect of Al_2O_3 content and the calcination temperature on the ZrO_2 phase composition. They observed that the crystallization temperature of ZrO_2 increased with Al_2O_3 content probably hinting that alumina distorts the ZrO_2 lattice and thereby delays the nucleation and growth of ZrO_2 crystallites.

Mills et al. [2.66] carried out the low temperature synthesis and zirconia doped alumina (5-20 wt% ZrO_2) nanopowder by hydrothermal process at a reaction temperature of

190°C and pressure 4 Kgf/cm^2. In the as synthesized powder, alumina was present as bayerite and boehmite while in the calcined samples it was α-Al_2O_3 and t-ZrO_2.

Chandradass et al. [2.67] reported the synthesis of zirconia doped alumina nanopowder by hydrothermal process. Al_2O_3-ZrO_2 composite precursor powder containing 5-20 wt% ZrO_2 had been prepared at 190°C and pressure 4 kgf/cm^2. Bayerite and boehmite was found in the as synthesized powder. The phases present in the powder calcined at 500 and 800°C are α-Al_2O_3 and t-ZrO_2. The particle size of alumina was found to be 60-70 nm whereas zirconia was 10-15 nm in the 800°C calcined powder.

2.6 General Literatures on Sintering

In ceramic manufacturing, sintering is a high temperature process which converts loosely bound particle compact in to a dense and cohesive body with a fine grained microstructure. This is usually achieved only when pores are uniformly distributed on grain boundaries which facilitate pore annihilation during final stage of sintering and avoids rapid grain growth [2.68, 2.69]. Usually a green compact made from an initial small particle size and narrow pore size distribution [2.70-2.75] usually sinters to a uniformly dense body.

Agglomerated powders, [2.74-2.76] on the other hand, disrupts the particle packing and produce a spatially heterogeneous green microstructure – a situation usually observed with nanopowder compaction. Such an inhomogeneous microstructure affects densification kinetics as well as the final sintered density achievable [2.76-2.78].

Sinterability could also be improved by controlling the agglomeration tendency during powder processing. The elimination of agglomerates by colloidal processing produces homogeneously packed green microstructure which could be sintered to high density at lower sintering temperature [2.70-2.75, 2.79]. Besides colloidal processing, two step sintering process can also produce a high density, fine grain size sintered body [2.82, 2.83].

The production of dense ceramics from nanocrystalline powders require clear understanding of the fundamental sintering theory as well as sintering models

[2.68,2.69,2.84-2.87]. Densification and microstructure evolution are interdependent and the densification process is influenced by the mechanism, material transport paths, material flux and mass transport distance [2.68-2.87]. An excellent review by Exner [2.88] discusses the initial stage of sintering kinetics and the controlling parameters. The particle – particle contact during sintering require simple geometrical assumptions for neck area, volume, radius of curvature and diffusion distance. The early models assumed several simple geometric approximations and ignored the possibility of multiple or parallel material transport paths. These simplified assumptions were less accurate when compared with the rigorous mathematical treatments obtained with exact neck shape. However, numerical analysis of the geometrical changes during sintering has been subject to criticism [2.89-2.96].

In the past, isothermal study was the major source of sintering data many of which did not agree well with the theoretical predictions. The discrepancy was partially due to the finite time required for reaching the isothermal sintering temperature and various corrections incorporated in the sintering result to account for the transient events during heating [2.97]. Two key decisions were made in an effort to minimize the experimental errors. Firstly, the use of constant heating rate measurements for establishing the initial events which did not require time or temperature corrections during the heating cycles [2.98-2.102] and secondly, both shrinkage and surface area were measured to monitor the geometric changes and sintering mechanisms. On the other hand, constant rate heating (CRH) method required lesser experimental work. In a single experiment involving slower heating rates, the temperature variation was less across a wide range and steady state could be reached at every temperature [2.103, 2.104].

Several methods had been used for the kinetic parameter calculation from the sintering curves obtained at different linear heating rates. The initial stage sintering activation energy had been obtained from the Arrhenius plots of the shrinkage rate (or densification rate) at equal values of the shrinkage (or density) [2.97, 2.98, and 2.105].

Several integer and differential methods had been applied for the kinetic analysis of a single sintering curve for Y-TZP [2.106-2.110] and result was the product of activation energy and kinetic law exponent and either of these two parameters needed to be known for evaluating the sintering mechanism. However, both the parameters could not be simultaneously determined from a single nonisothermal experiment. [2.107, 2.108].

2.7 Sintering of Al_2O_3 –ZrO_2 Composites:

Young and Cutler studied the kinetic analysis of the initial stage of sintering in CRH experiment [2.97] for YSZ which permitted simultaneous determination of activation energy as well as the kinetic model from a single CRH dilatometric curve. The results suggested that grain boundary (GB) diffusion dominated the initial stage sintering.

CRH sintering experiments had also been carried out for estimation of the sintering activation energy for sintering of Al_2O_3, Al_2O_3 - 5 vol% ZrO_2 or Al_2O_3 - 5 vol% TiO_2 [2.105]. The kinetic analysis was complicated by grain growth and the later was restricted by controlling powder characteristics by adopting improved colloidal processing. GB diffusion was the dominant densification mechanism. The sintering activation energies were 440 ± 40 kJ/mol for pure Al_2O_3, 585 ± 40 kJ/mol for Al_2O_3 - 5 vol% TiO_2, and 730 ± 60 kJ/mol for Al_2O_3 - 5 vol% ZrO_2.

Wang and Raj [2.109] had investigated the sintering activation energy in two phase Al_2O_3 –5 vol% ZrO_2 ceramics using both CRH and isothermal densification experiments. The activation energy was 700 ± 100 kJ/mol for ZrO_2 content 5 to 95 vol%. In contrast, the activation energy 615 ± 80 kJ/mol for pure ZrO_2 and 440 ± 45 kJ/mol for pure Al_2O_3. The addition of 2.8 mol% Y_2O_3 (as dopant) did not have any measurable influence on activation energy.

High density ultrafine Al_2O_3 - 5 vol% ZrO_2 ceramics had been processed by two-step sintering process [2.110]. First step was CRH experiment (1400-1450^{o}C) and the second step was isothermal sintering (1350-1400^{o}C) for varying time periods, the first step ensured high initial density and the second step increased the density further with a concurrent grain growth. It appeared that ZrO_2 acted to pin down the Al_2O_3 grain growth. The resultant Al_2O_3-ZrO_2 had high density (> 99%) and fine grain size (0.62-0.88 μm) of Al_2O_3.

Green sheets of YSZ/Al_2O_3 nanocomposite ceramics made from coprecipitated powder were densified by pressureless sintering [2.111]. The sintered YSZ/Al_2O_3 sheets were characterized for relative density, grain size, phase, and microstructure. The relative density >95% were obtained for 20-85 mol% YSZ composition. The average grain size of both ZrO_2 and Al_2O_3 decreased at higher YSZ content. YSZ also restricted the rapid grain growth of Al_2O_3.

Al_2O_3-ZrO_2 (1, 3, 5 vol %) nanocomposites prepared from commercial Al_2O_3 and YSZ powder [2.112] were sintered in microwave hybrid sintering. Microwave hybrid fast firing helped in arresting the grain growth of the composite. The resultant microstructure was uniform with small grains, the average grain to particle ratio being 2:1.

The isothermal shrinkage behavior of 2.9 mol% Y_2O_3-ZrO_2/Al_2O_3 (0-1 mol %) was investigated to ascertain the role of Al_2O_3 addition during initial stage of sintering (950-1050^oC) [2.113]. Al_2O_3 addition increased the densification rate and mass transport mechanism changed from GB diffusion to volume diffusion.

Huang et al. [2.114] studied the densification behavior of gel precipitated and heterogeneous azeotropic distillated ZrO_2-Al_2O_3 composite powder. High elastic modulus alumina caused pinning effect, blocks Zr^{4+}(Y^{3+}) mass transfer process as well as grain boundary movement. An increase in Al_2O_3 content inhibited ZrO_2 grain growth caused delayed crystallization of ZrO_2 and resulted in high dense and strong composite.

Grain growth behavior in Al_2O_3 -ZrO_2 (≤ 5 vol %) had been studied by Nagashima et al. [2.115]. It was observed that even a small amount of ZrO_2 could retard Al_2O_3 grain growth. At lower ZrO_2 percent, majority of ZrO_2 was at intragranular position and this tendency was reduced at higher sintering temperature. The grain growth inhibition of ZrO_2 was in agreement with modified Zener's pinning model.

Matsui et. al. [2.116] added small amount of Al_2O_3 to fine ZrO_2 powder either by direct powder mixing or alkoxide hydrolysis or homogeneous precipitation and observed the densification behavior by CRH method. Al_2O_3 addition slightly raised the densification onset temperature and simulated the densification above 1100^oC. In the isothermal densification analysis, Al_2O_3 addition retarded the densification rate (in comparison to Al_2O_3 free samples) just after the onset of sintering followed by a significant increase in the densification rate. These results implied that during the initial stage, Al_2O_3 particles pin ZrO_2 particles causing a reduction of densification and in the later stage, Al_2O_3 diffuses to the ZrO_2 surface and enhance the sintering rate.

The influence of Al_2O_3 on sintering and static grain growth behavior of high purity commercial 8YCSZ-Al_2O_3 (1-10 wt %) were investigated. The powders were made by colloidal processing which ensured uniform and homogeneous distribution of both phases. Till 0.5 wt% Al_2O_3 addition, sintering 8YCSZ-Al_2O_3 for 1hr between 1250-1400^oC resulted in density increase. At higher addition, the density decreased. Rearrangement of Al_2O_3 particles (at low addition) resulted in density increase. Higher (>0.5%) Al_2O_3 content reduced grain boundary diffusivity and grain mobility thereby reducing sintering.

2.8 Mechanical Properties

Chaim [2.120] studied the processing and mechanical properties of Alumina-20 wt% Zirconia and Zirconia- 20 wt% Alumina (ZTA) which had been prepared by pressureless sintering between 1400°C to 1600°C. They observed that due to the change in particle packing, higher green densities were obtained for powders having large particle size. The final sintered density was higher for finer particle size. The volume fraction of retained *t*-ZrO_2 was dependent on final density and *t*- ZrO_2 grain size. Many ZrO_2 had twinned feature characterizing *m*-ZrO_2. An increase in density resulted in an increase in Vickers hardness. Although the bending strength of ATZ composites was lower (250-500 MPa), the fracture toughness was significantly higher (9 MPa √m) in the sample containing about 96% retained t- ZrO_2 of critical size and the toughness resulted from transformation toughening effect. Due to presence of Al_2O_3, ZTA samples also showed improvement in hardness over that of pure ZrO_2 but at the same time had lower bending strength (due to porosity) but higher fracture toughness (due to higher t-ZrO_2 fraction and its transformability).

Krell et al. [2.121] studied the influence of microcrack density as well as dispersion homogeneity on the mechanical properties of Al_2O_3- ZrO_2 composites. The composites were prepared by two different routes. In the first route (Route-A), commercial Al_2O_3 and milled ZrO_2 (5-20 vol %) were mixed and the mixture was remilled in planetary milled, dried and granulated. In the second method (Route-B), aqueous $ZrOCl_2.8H_2O$ solution was added to Al_2O_3 and mixture was homogenized in planetary mill for 4 to 10 hours followed by freeze drying and calcination (950°C/2 hours). In all the specimens (prepared by both routes), 1400 ppm MgO (as $MgCl_2·6H_2O$) was added. The green compacts were sintered between 1560°C and 1625°C for 1 hour. Microcrack toughening was the dominant toughening mechanism and the maximum toughness was 8 MPa √m at 11.5 vol% ZrO_2 addition for Route-A samples. However, in Route-B, the highest toughness was 11.8 MPa √m which was attributed to finer and more homogeneous distribution of ZrO_2 in Al_2O_3 matrix.

Hirano et al. [2.122] studied the fracture toughness, strength and Vickers hardness of Y_2O_3-CeO_2 codoped ZTA composites. Dense composites were prepared by hot pressing. The ZTA composites were 75 wt% (Y-Ce) TZP and 25 wt% Al_2O_3. Three different compositions of (Y, Ce) TZP viz. (4 mol% $YO_{1.5}$ – 4 mole% CeO_2) TZP, (2.5 mol% $YO_{1.5}$ – 4 mole% CeO_2) TZP, (2.5 mol% $YO_{1.5}$ – 5.5 mole% CeO_2) TZP were studied. The HIPing operation was carried out 1400°C. $CeO_2 \rightarrow Ce_2O_3$ phase transformation took place in the reducing gas atmosphere during HIPing which resulted in lower amount of retained *t*- ZrO_2 for zero Al_2O_3 addition. However, Al_2O_3 addition suppressed the $t\rightarrow m$ phase transformation. It was further noted that the fracture toughness, strength and hardness of (Y, Ce) TZP/ Al_2O_3 composite were dependent on the hot pressing temperature. The strength and toughness decreased when the composites were hot pressed at 1600°C.

Grigoryev et al. [2.123] studied the effect of different volume fraction of 3Y-TZP addition Al_2O_3 on the strength, toughness, hardness and microstructure after hot pressing. They noted that in the hot pressed composite a non transformable *t*-ZrO_2 (*t*- ZrO_2) was also present besides *t* and *m*-ZrO_2. While the fracture toughness remained essentially unchanged (~7 MPa√m) at different 3Y-TZP volume fraction, the hardness decreased and the strength increased with 3Y-TZP volume fraction. The results were explained with reference to the fraction of *t*-ZrO_2, change in crack propagation path, microstructure refinement and change in the matrix hardness resulting at higher 3YTZP addition.

Srdic et al. [2.124] studied the effect of fine and homogeneous microstructure on the transformation toughening behaviour of Al_2O_3 – 20 wt% unstabilized ZrO_2.The composites were prepared through sol-gel method by mixing α- Al_2O_3 seeded alumina sol (containing 20 wt % boehmite) with three different concentration zirconia sols (hydrolyzed alcoholic solution of Zr-n-P). The composites had high sintered density (>90 %) at all sintering schedules (1400°C,1500°C and 1600°C). The average size of zirconia grains increased with sintering temperature. Uniformly dispersed ZrO_2 grains (0.45 μm) restricted the grain growth of Al_2O_3. However, at 1600°C, most of the ZrO_2 converted to m- ZrO_2. Although transformation toughening was dominant toughening mechanism, the rather low toughness (K_{IC} < 6 MPa√m) suggests that in these composites addition of a small fraction of unstabilized ZrO_2 are not effective for a significant improvement of fracture toughness.

Konsztowicz et al. [2.125] studied the effect of heteroflocculation on the mechanical properties of zirconia toughened alumina composite (ZrO_2 5-30 vol %). The composites were colloidally processed from dense aqueous suspensions (>50 vol% of solids). Three different type of ZrO_2 were used viz. unstabilized ZrO_2, partially stabilized with 2mol% Y_2O_3 and nontransformable t- ZrO_2 (t') with 3 mole% Y_2O_3. The microstructural changes of sintered composites indicated an increasing degree of hetero flocculation of ZrO_2 - Al_2O_3 at higher ZrO_2 content. For ZrO_2 content ≤ 10 vol%, the grains were well dispersed and at 30 vol% ZrO_2, large clusters were observed. At lower ZrO_2 content (≤ 10 vol %), the dispersed ZrO_2 phase primarily acts as grain growth inhibitor for Al_2O_3. With undoped ZrO_2, both peak strength (1000 MPa) and toughness (8 MPa√m) was obtained at 10 vol% ZrO_2 additions. For ZTA with 2 mole% YSZ, the peak strength (1500 MPa) was obtained at 20 vol% ZrO_2 addition and peak toughness (9 MPa√m) was at 30 vol% ZrO_2 addition. While stress induced microcracking was responsible for the property enhancement for the first case, both transformation toughening and microcracking accounted for the strength and toughness increment in the second case. In the third case, use of 3 mole% TZP for preparing ZTA resulted in nontransformable t-ZrO_2 in Al_2O_3 matrix and the strength , toughness were mainly governed by dispersion strengthening mechanism.

Balasubramanium et al. [2.126] used sol-gel method to prepare Al_2O_3-12.5 wt% ZrO_2 composites using different combinations of precursors, viz. (i) aluminium sulfate and zirconium oxychloride and (ii) aluminium sec butoxide and zirconium isopropoxide. While the mixed ZTA powders from the first route were spherical (average particle size 3 μm), the powders from the second and third route were irregular shape (average particle size 10μm). Due to the smaller particle size, the first route powders had higher sintered density (92%) than the other two (75 and 78% respectively).

Casellas et al. [2.127] studied the effect of thermally induced microstructural coarsening on the fracture toughness of zirconia-alumina composites containing 5, 15 and 30 vol% 3YTZP.The composites were cold isopressed at 200 MPa and sintered at 1600°C for 2hours.It was observed that microstructural coarsening of this dual phase ZTA was dependent on the volume fraction of the second phase. At low volume fraction (5 vol %) of 3YTZP, the grain growth of the matrix (Al_2O_3) is pinned by the dragging force of 3YTZP. However, at 10 vol% 3YTZP, zirconia clusters are formed which becomes more effective pinning the grain boundaries. When 3YTZP addition > 30 vol%, microstructural coarsening became difficult and Al_2O_3 grain growth was absent due to large volume of ZrO_2 which prevent grain to grain contact of Al_2O_3. The increase in fracture toughness with 3YTZP addition was correlated to transformation toughening effect.

Vleugels et al. [2.128] studied the mechanical properties of Y_2O_3/ Al_2O_3 coated YTZP ceramics. The mixed nanopowder was prepared from a suspension of aluminium nitrate, yttrium nitrate and ZrO_2 powder in an alcohol water mixture. Fully dense YTZP ceramic were obtained by hot pressing at 1400, 1450 or 1500°C. It was also noted that the fracture toughness of the Al_2O_3 /Y_2O_3 coated powder based YTZP ceramics could be tailored by optimum selection of overall Y_2O_3 content. The maximum toughness of Y-TZP with 2 wt% Al_2O_3 was obtained at 1.75 mole% Y_2O_3 content and at a hot pressing temperature at 1450°C.The yttria-coated ZrO_2 starting powder could result in Y-TZP ceramics having both wide distribution of yttria content (containing both c and transformable *t*-ZrO_2 grains) as well as grain size. The superior fracture toughness resulted from the presence of Y-TZP grains having wide variation in Y_2O_3 content thereby making some grains more transformable.

Adachi et al. [2.129] studied the effect of nano SiC dispersed (5 vol %) on the crack propagation behaviour of Al_2O_3 /3Y-TZP hybrid composites. The multilayer composite was prepared by doctor blade process through alternate stacking of 99.99 % pure α-Al_2O_3, 3Y-TZP and SiC. The microstructural analyses of the layer boundaries were smooth with no visible reaction between the phases. The magnitude of residual stress was dependent on the mismatch of CTE between the layer components and residual stress could be controlled by changing SiC dispersion. The study of crack propagation suggested that the crack deflection was influenced by the nature and magnitude of residual stress within the composites.

Celli et al. [2.130] utilized fractal geometry concept to analyze the Vickers indented path in alumina-zirconia composites. The fractal dimension parameter (η_s) for each crack referred to a corresponding three dimensional geometry of fracture surface. The study suggested that samples with high percentage of alumina as well as pure zirconia were characterized by intergranular of fracture surface. This class of composites had a correlation between microstructure, crack path and toughness. A higher population of larger alumina grains ,rough and irregular crack geometry as well as fracture surface geometry leads to higher toughness on account of crack deflection mechanism. However, in composites containing high zirconia content, transgranular fracture was predominant.

Han et al. [2.131] studied the microstructure of Al_2O_3-50 wt% ZrO_2 composites using insitu synthesized Al_2O_3-ZrO_2 composite powder. The composite powders were prepared via sol-gel process with aluminium iso-propoxide and zirconium butoxide as the precursors. The as received amorphous composite powder on being calcined between 900°C and 1100°C, crystallized to t-ZrO_2 and finally to m- ZrO_2 through the intermediate phase of c -ZrO_2. However, they claimed that alumina particles remained in an amorphous stage till 1100°C. The different pore sizes (400-1100 nm) of the sintered porous composites were uniformly distributed.

Cesari et al. [2.132] simulated the toughening effect in alumina-zirconia using a simple model based on two concentric spheres and a crack in the matrix near the interface of the inclusion. The model had taken into consideration the $t \rightarrow m$ phase transformation effect and the thermal stress developed during cooling of the composite from the sintering temperature. The authors had simulated the toughening effect by imposing a uniform temperature field both to the matrix and the inclusion and the effect was studied at different temperatures. The simulated fracture toughness results (at room temperature) correlated well with the experimentally data obtained fracture toughness for different volume fraction of zirconia.

Vasylkiv et. al. [2.133] prepared zirconia /alumina nano composite using Y-TZP (0.75 to 3 mol% Y_2O_3) with γ-alumina (0.2 to 0.7%) through a colloidal processing route (powder loading 18-20 vol %). The slip cast composites were sintered in air at 1150 ^{0}C for 2 to 30 hours. The authors observed that γ-alumina helped to enhance the densification rate and the average grain size was 92 nm. The fracture toughness was high (15.7 MPa√m) for 1.5-2 mol% Y-TZP/ 0.35 wt% alumina composites and it was 7.86 MPa √m for 3Y-TZP/0.35 wt% alumina composites.

Basu et al. [2.134] prepared ZrO_2–Al_2O_3 composite with tailored toughness .The composites were prepared from both commercial and precipitated ZrO_2 powder as well as a mixture of 3Y-TZP + Y free monoclinic ZrO_2 with 28 vol% Al_2O_3. The densification was via hot pressing in vacuum at 1450^{0}C for 1 hour. Different levels of toughness were obtained for the two composites which were explained in terms of yttria content, the yttria distribution and the residual stress due to the presence of Al_2O_3 particles in the matrix. Transformation toughening was the major toughening mechanism. They further observed that due to an inhomogeneous distribution of Y_2O_3 in the mixture Y-TZP + *m*-ZrO_2 it gave rise to high toughness probably due to auto catalytic effect.

The effect of residual stresses on the wear and friction behaviour during sliding in water of functionally graded alumina-ZTA composites were studied by Novak et. al. [2.135]. The predominant tribological mechanisms were assessed and analyzed using neutron diffraction, X-ray diffraction and scanning electron microscopy and using homogeneous alumina as base material. The authors observed that an increase in the residual compressive stresses of FGM reduced the wear and friction as well as produced thinner tribomechanical layer of detached debris from the surface.

Bermejo et al. [2.136] optimized the strength and toughness of ZrO_2–Al_2O_3 laminates through designing with external or internal compressive layers. The authors designed two alumina-zirconia laminates - one with external (ECS laminates) and the other with internal laminated (ICS laminates) compressive stress and the stress optimization was investigated using fracture mechanics weight fraction analysis. They observed that in general, ECS laminates had maximum apparent toughness at the first interlayer (A/AZ) for a relatively thin outer compressive layer. However, in the ICS laminates the maximum apparent toughness was realized at the second phase interface (AMZ/ATZ) for a relatively thick tensile (ATZ) layer. The strength optimization was found for a laminate design consisting of 9 layers and total thickness of 3 mm.

Gougalez et al. [2.137] studied the damage and R-curve behavior of alumina-zirconia-niobium multiphase composites by indentation strength method. They prepared different kinds of samples. The first variety had 3Y-TZP matrix which was strengthened by Al_2O_3 particles (ATZ). In the second variety, alumina matrix was strengthened with 3Y-TZP (ZTA). Both types of composites had further addition of niobium as reinforcement and were hot pressed. The authors studied the crack growth behavior of the composites and observed that both the stress induced transformation effect by ZrO_2 as well as crack bridging effect by Nb were the main factors for crack shielding as well as for exerting crack closure forces. The synergistic effect originated due to the interaction between toughening mechanism of Nb grains and zirconia grains in the Al_2O_3-ZrO_2-Nb composites.

Weimin et al. [2.138] studied the densification behavior, microstructure and transformation behavior of Al_2O_3-2YTZP and Al_2O_3-3YTZP (TZP 10, 15, 20, 25, 30 vol %). The volume fraction of Y-TZP affected the $t \rightarrow m$ ZrO_2 transformation. At 15 vol% TZP addition, the composites sintered to near theoretical density. Energy spectrum analysis confirmed different bonding level of Al^{3+} with 3Y-TZP and 2Y-TZP. High toughness values were obtained at TZP level 15-20 vol% with transformation toughening being the predominant mechanism.

Guimaraes et al. [2.139] worked on the Al_2O_3-ZrO_2 nanocomposites containing 1, 3 and 5 vol% m-ZrO_2 nanoparticles. The authors correlated the microstructure, mechanical properties and wear resistance of these composites. The microstructural analysis showed that zirconia addition helped to retard Al_2O_3 grain growth and improved the mechanical properties as well. At 5 vol% ZrO_2 addition, the improvement was 8% for microhardness, 11% for flexural strength and 23% for wear resistance in comparison to pure alumina. The results were explained in the light of microstructural refinement due to ZrO_2 addition.

Liu et al. [2.140] studied the effects of $Sr_2Nb_2O_7$ addition on the microstructure and mechanical properties of 3Y-TZP (45 vol %) /Al_2O_3 (55 vol %) composites. The volume fractions of $Sr_2Nb_2O_7$ were 0.005, 0.01, 0.015 and 0.02. During the sintering of composites (1500°C to 1600°C), the added $Sr_2Nb_2O_7$ reacted with Al_2O_3 to form elongated $SrAl_{12}O_{19}$ platelets which contributed positively towards the composite fracture toughness. The fraction of transformable *t*-ZrO_2 as well as fracture toughness firstly increased with $Sr_2Nb_2O_7$ addition (up to 0.005) and then decreased with further addition. The maximum toughness was 10.5 MPa√m and toughness enhancement is due to the combined effect of transformation toughening and elongated grain toughening.

Jin et al. [2.141] prepared ZTA/$LaAl_{11}O_{18}$ composites by two different methods and studied the effects of powder preparation on the microstructure and mechanical properties of ZTA/$LaAl_{11}O_{18}$ composites. Both type of composites retained *t*-ZrO_2 in non transformable form. When aqueous precursors were used for composite preparation, the obtained microstructure was homogeneous with smaller Al_2O_3 grain. The Al_2O_3 grains showed a higher tendency for transgranular fracture thereby increasing the fracture strength though the toughness did not improve.

Daguano et al. [2.117] studied the different mechanical properties of ZTA (20 wt %) ceramics as a function of isothermal holding time at 1600°C. The grain growth exponent (n) of the composite for ZrO_2 and Al_2O_3 were 2.8 and 4.1 respectively, indicating different grain growth mechanisms for ZrO_2 and Al_2O_3 . The hardness had a sintering time dependency. The high hardness (1300 to 1500 Hv) and fracture toughness (8 MPa√m) makes it suitable as dental implants.

Yang et al. [2.142] studied the influences of nano particles on the microstructure and the mechanical behavior of Ce-TZP/ Al_2O_3 nano composites. The five different compositions were prepared from synthesized Ce-TZP powder and commercial Al_2O_3 powder wherein Ce-TZP was varied from 10 to 50 wt% .The composites were hot pressed at 1450^{o}C at 20 MPa. The addition of 20 wt % nano Ce-TZP to Al_2O_3 improves the densification behavior of the composites. The mechanical properties and microstructure were also optimum at this level of Ce-TZP. TEM revealed dislocation structure formation in Al_2O_3 as well as in grain boundary and these could have helped crack deflection thereby providing strengthening effect.

Balakrishnan et al. [2.143] studied the effect of low thermal expansion MgO- Al_2O_3-SiO_2 glass infiltration at the surface on the mechanical properties of Al_2O_3 -10 wt% ZrO_2 (3Y-TZP).The glass infiltration improved both the room temperature as well as high temperature composite strength. The weibull modulus as well as thermal shock resistance increased significantly after glass infiltration. The strength increment could be correlated with surface residual stress generated by the thermo-elastic properties mismatch between the composite and the glass.

Rascon et al. [2.144] studied the influence of pressureless sintering on the Vickers hardness and fracture toughness of ZrO_2 reinforced with Al_2O_3 (ATZ) and Al_2O_3 reinforced with ZrO_2 (ZTA). 3Y-TZ particles situated at the grain boundaries inhibited Al_2O_3 grain growth. ZrO_2 (80 wt %) / Al_2O_3 (20 wt %) composites had high hardness (16.05 GPa) and fracture toughness (7.44 MPa√m). It is interpreted that submicron grain size and low residual porosity causes the hardness and fracture toughness to increase. The composite properties are well suited for use as dental implants.

Ganesh et al. [2.145] prepared ZTA composites of different compositions (containing 30 wt% 3Y-TZ) and ZTA-60 (containing 60 wt%).The composites were shaped by hydrolysis induced aqueous gel casting method.1.5 wt% Al_2O_3 in the precursor powder were replaced by an equivalent amount of AlN for co-promoting the green consolidation by aqueous gel casting method. The uniform microstructure obtained through gel casting process resulted in higher toughness (7.38 MPa√m) and strength (660 MPa).

Ahmad Azhar et al. [2.146] studied the effect of Al_2O_3/YSZ microstructure on wear and mechanical properties of ZTA cutting inserts. It was observed that composites with 20 wt% YSZ produced minimum wear area. However, Vickers hardness decreased with increasing in YSZ content .Above 60 wt% YSZ, the composite microstructure had microcracks and large grains of YSZ and these effects hindered the transformation toughening mechanism from being effective.

References

2.1. N. Claussen,"Fracture toughness of Al_2O_3 with an unstabilized ZrO_2 dispersed phase", J. Am. Ceram. Soc., 59**,** 49-51 (1976).

2.2. F. F. Lange, "Transformation Toughening, Part 1, Size effects associated with the thermodynamics of constrained transformation", J. Mat. Sci., 17, 225-234 (1982).

2.3. F. F. Lange, "Transformation Toughening, Part 2, Contribution to fracture toughness", J. Mat. Sci., 17, 235-239 (1982).

2.4. F. F. Lange, "Transformation Toughening, Part 3, Experimental observation in ZrO_2-Y_2O_3 system", J. Mat. Sci., 17, 240-246 (1982).

2.5. F. F .Lange, "Transformation Toughening, Part 4, Fabrication, fracture toughness and strength of Al_2O_3-ZrO_2 composites", J. Mat. Sci., 17, 247-254 (1982).

2.6. A. H. Heuer, "Transformation toughening in ZrO_2-containing ceramics", J. Am. Ceram. Soc., 70, 689–698 (1987).

2.7. A. G. Evans, "Perspective on the development of high-toughness ceramics", J. Am. Ceram. Soc., 73**,** 187–206 (1990).

2.8. D.J. Green, R.H.J. Hannink and M.V. Swain, "Transformation Toughened Ceramics", CRC Press, 1989.

2.9. A. G. Evans and R. M. Cannon, "Toughening of brittle solids by martensitic transformations", Acta Metall., 34, 761–800 (1986).

2.10. A.G. Evans and A.H. Heuer, "Review transformation toughening in ceramics: martensitic transformations in crack-tip stress fields", J. Am. Ceram. Soc., 63, 241– 248 (1980).

2.11. R. O. Ritchie, "Mechanisms of fatigue crack propagation in metals, ceramics, and Composites: Role of crack tip shielding", Mater. Sci. Eng., A103, 15–28 (1988).

2.12. R. M. Mc Meeking, "Effective transformation strain in binary elastic composites", J. Am. Ceram. Soc., 69**,** C-301–C-302 (1986).

2.13. B. Budiansky, J. Hutchinson, and J. Lambropoulos, "Continuum theory of dilatant transformation toughening in ceramics", Int. J. Solids Struct., 19**,**337–355 (1983).

2.14. P. F. Becher and M. V. Swain, "Grain-size-dependent transformation behavior in polycrystalline tetragonal zirconia", J. Am. Ceram. Soc., 75, 493–502 (1992).

2.15. W. M. Kriven, “Possible alternative transformation toughness to zirconia: crystallographic aspects,” J. Am. Ceram. Soc., 71, 1021–1030 (1988).

2.16. M. V. Swain, “Inelastic deformation of Mg-PSZ and its significance for strength–toughness relationship of zirconia-toughened ceramics”, Acta Metall., 33, 2083–91 (1985).

2.17. L. R. F. Rose, “The mechanics of transformation toughening*”,* Proc. R. Soc. London, *A,* 412, 169–197 (1987).

2.18. D. B. Marshall, M. C. Shaw, R. H. Dauskardt, R. O. Ritchie, M. J. Readey, and A. H. Heuer, “Crack-tip transformation zones in toughened zirconia” ,J. Am. Ceram. Soc., 73, 2659–2666 (1990).

2.19. C. S. Yu, D. K. Shetty, M. C. Shaw, and D. B. Marshall, “Transformation zone shape effects on crack shielding in ceria-partially-stabilzed (Ce-TZP)–alumina composites” , J. Am. Ceram. Soc., 75, 2991–2994 (1992).

2.20. A. G. Evans, “Transformation Toughening: An Overview”, J. Am. Ceram. Soc., 69 [3] iii (1986).

2.21. J. C. Lambropoulos, “Shear, shape, and orientation effect in transformation toughening”, Int. J. Solids Struct., 22 1083 (1986).

2.22. A. G. Evans, D B Marshall and N H Burlingame, in “Advances in Ceramics”, Vol 3, “Science and Technology of Zirconia I, edited by A H Heuer and L W Hobbs, The American Ceramic Society, Columbus, OH, 1981, p 202.

2.23. A. G. Evans , in “Advances in Ceramics”, Vol 12 “Science and Technology of Zirconia II, edited by N. Claussen, M Ruhle and A H Heuer, The American Ceramic Society, Columbus, OH, 1984, p 193.

2.24. J. Wang and R. Stevens, “Review- Zirconia toughened alumina (ZTA) ceramics”, J. Mat. Sci., 24, 3421-3440 (1989).

2.25. N. Claussen and M. Ruhle in “Advances in Ceramics”, Vol 3, “Science and Technology of Zirconia I, edited by A H Heuer and L W Hobbs, (The American Ceramic Society, Columbus, OH, 1981), p 137.

2.26. D. J. Green and B. R. Maloney, "Influence of surface stress on indentation cracking’’, J. Am. Ceram. Soc., 69, 223–225 (1986).

2.27. D. J. Green, F. F. Lange and M. R. James, “Factors influencing residual surface stresses due to a stress induced phase transformation” J. Am. Ceram. Soc., 66 623 (1983).

2.28. R.W. Rice, "Ceramic Matrix Composite Toughening Mechanisms: An Update," Cer. Eng. and Sci. Proc., 6, 589-607 (1985).

2.29. D. B. Marshall and M. R. James, “Reversible stress-induced martensitic transformation in ZrO_2”, J. Am. Ceram. Soc., 69, 215-217 (1986).

2.30. A.G. Evans, N. Burlingame, M. Drory and W.M. Kriven, “Martensitic transformations in zirconia particle size effects and toughening”, Acta Metall. 29,447-456 (1981).

2.31. G.J. Liu, H.B. Qiu, R. Todd, R.J. Rrook and J.K. Guo, “Processing and mechanical behaviour of $Al_2O_3|ZrO_2$ nanocomposites”, Mater. Res. Bull. 33 [2] 282-88 (1988).

2.32. B. Basu, J. Vleugels and O. Vander Biest, “ZrO_2-Al_2O_3 composites with tailored toughness”, J. Alloys and Compounds, 372, 278-284 (2004).

2.33. S. Huang, L. Li, J. Vleugels, P. Wang and O. Vander Biest, “Influence of Al_2O_3 addition on the microstructure and mechanical properties of pressure less sintered Ce-TZP”, Mat. Sci. Forum, 492-493, 783-793 (2005).

2.34. J.C. Debsikdar, “Influence of synthesis chemistry on alumina-zirconia powder characteristics”, J. Mat. Sci., 22, 2237-2247 (1987).

2.35. C-C Chan, F-S Yen and C-Y Huang, “Aging effects on the characteristics and sintering behaviour of co-precipitated Al_2O_3-ZrO_2 powder”, Ceram. Int., 20, 379-384 (1994).

2.36. J.L. Shi, B.S. Li, M.L. Ruan and T.S. Yen, “Processing of nano – Y- TZP/Al_2O_3 composite powder”, J. Eur. Ceram. Soc., 15, 959-965 (1995).

2.37. J.S. Hong, S.D. De La Torre, K. Miyamoto, H. Miyamoto and L. Gao, “Crystallization of Al_2O_3/ZrO_2 solid solution powder prepared by co-precipitation”, Mat. Letts., 37, 69, (1998).

2.38. D.D. Upadhayay, M.R. Goyal, R. Prasad, “Studies on crystallization behaviour of 3Y-TZP/Al_2O_3 composite powder”, Mat. Sci. & Engg.- A, 270, 133-136 (1999).

2.39. N. Enomoto, J-M Tang, M. Uehara, H. Maeda, J. Hojo and Z-e Nakagawa, “Process study on alumina-zirconia nanocomposite via ammonolysis route”, J. of Ceram. Proc. Res., 1, 88-91 (2000).

2.40. I.M. Low and R. Mc Pherson, “Crystallization of gel-derived alumina and alumina – zirconia ceramics”, J. Mat. Sci., 24, 892-98 (1989).

2.41. N. Balagopal, C. Sunil Kumar, A.D. Damodaran and K.G.K. Warrier, “Sintering of sol-sprayed alumina-zirconia composites”, J. Mat. Sci. Lett., 13, 789-786 (1994).

2.42. D.D. Jayaseelan, D. Amutha Rani, T. Nishikawa, H. Awaji and F.D. Gnanam, “Powder characteristics, sintering behaviour and microstructure of sol-gel derived ZTA composites”, J. Eur. Ceram. Soc., 20, 267-275 (2000).

2.43. M. Chatterjee, M.K. Naskar and D. Ganguli, “Sol-emulsion-gel synthesis of aumina-zirconia composite microspheres”, J. Sol-Gel Sci. & Tech., 28, 217-225 (2003).

2.44. B-T Lee, J-K Han and F. Saito, “Microstructure of sol-gel synthesized Al_2O_3 – ZrO_2 (Y_2O_3) nano composites studied by transmission electron microscopy”, Mat. Lett., 59, 355-360 (2005).

2.45. J. Chandradass, M. Balasubramanium, “Sol-gel Processing of alumina – zirconia minispheres”, Ceram. Int., 31, 743-748 (2005).

2.46. P. Palmero, V. Naglieri, J. Chevalier, G. Fantozzi, and L. Montanaro, “Alumina based nanocomposites obtained by doping with inorganic salt solutions: Application to immiscible and reactive systems”, J. Eur. Ceram. Soc., 9, 59-66 (2009).

2.47. A.T. Gilan, E.T. Nassaj and H. Akhondi, “The effect of zirconia content on properties of Al_2O_3-ZrO_2 (Y_2O_3) composite nanopowders synthesized by aqueous sol-gel method”, J. Non Cryst. Solids, 355, 311-316 (2009).

2.48. S. Bhattacharyya, S. K. Pratihar, R. K. Sinha, R. C. Behera and R. I. Ganguly, “Preparation of alumina–high zirconia microcomposite by combined gel-precipitation”, Mat. Lett. 53,425-431(2002).

2.49. R.P. Rana, S.K. Pratihar, S. Bhattacharyya, “Effect of powder treatment on the crystallization behaviour and phase evolution of Al_2O_3-High ZrO_2 nanocomposites”, J. Mat. Sci., 41, 7025-7032 (2006).

2.50. S. Novak, T. Kosmac and V. Ribitsch, “Investigation of the powder characteristics and microstructures of alumina-zirconia composites”, Mat. Sci. & Engg. A, 194 235-241 (1995).

2.51. V. Ramakrishnan, Pradip and G.S. Malghan, “The stability of alumina-zirconia suspensions”, Colloids and Surfaces A: Physicochemical and Engineering Aspects, 133, 135-142 (1998).

2.52. T.S. Suzuki, Y. Sakka, K. Nakano and K. Hiranga, “Effect of ultrasonication on the microstructure and tensile elongation of zirconia-dispersed alumina ceramics prepared by colloidal processing”, J. Am. Ceram. Soc., 84, 2132-34 (2001).

2.53. A. Dakskobler, T. Kosmac, “The preparation and properties of Al_2O_3-ZrO_2 composites with corrugated microstructures”, J. Eur. Ceram. Soc., 24, 3351-3357 (2004).

2.54. H. Sarraf, R. Herbig and M. Maryska, “Fine-grained Al_2O_3-ZrO_2 composites by optimization of the processing parameters”, Scrip. Mater., 59, 155-158 (2008).

2.55. K.C. Patil, S.T. Aruna and S. Ekamtaran, “Combustion Synthesis”, Current Opinion in Solid State & Materials Science, 2 158-165 (1997).

2.56. Y. Wu, A. Bandyopadhyay and S. Bose, “Processing of alumina and zirconia nano-powders and compacts”, Mat. Sci. and Engg. A, 380, 349-355 (2004).

2.57. S. Biamino, P. Fino, M. Pavese and C. Badini, “Alumina – zirconia - yttria nanocomposites prepared by solution combustion synthesis”, Ceram. Int., 32, 509-513 (2006).

2.58. J.J. Kingsley and K.C. Patil, “A novel combustion process for the synthesis of fine particles α-Al_2O_3 and related oxide materials”, Mat. Lett., 6, 427-432 (1988).

2.59. S.T. Aruna and K.S. Rajam, “Mixture of fuels approach for the solution combustion synthesis of Al_2O_3-ZrO_2 nanocomposites”, Mater. Res. Bull., 39, 157-167 (2004).

2.60. Z. Zhao, L. Zhang, Y. Song and W. Wang, “$Al_2O_3|ZrO_2$ (Y_2O_3) self growing composites prepared by combustion synthesis under high gravity”, Scrip. Mater., 58, 207-210 (2008).

2.61. S. Kikkawa, A. Kijima, K. Hirota and O. Yamaguchi, “Soft solution preparation methods in a ZrO_2-Al_2O_3 binary system”, Solid State Ionics, 151, 359-164 (2002).

2.62. A. Beitollahi, H. H-Bay and H. Sarpoolaki, “Synthesis and characterization of Al_2O_3-ZrO_2 nanocomposite powder by sucrose process”, J. Mater. Electron, DOI: 10.107/S10854-009-9880-9, Published online: 04 April 2009.

2.63. A.S. Rao and W.R. Cannon, “Alumina-Zirconia composites produced from commercial alumina and synthesized hydrous zirconia”, Ceram. Int., 15, 179-188 (1989).

2.64. A. Saha and D.C. Agrawal, “Microstructure development in hybrid sol-gel prepared Al_2O_3-ZrO_2 composites”, J. Mater. Sci., Lett., 17, 1333-1336 (1998).

2.65. P. Rao, M. Iwasa, J. Wu, J. Ye and Y. Wang, “Effect of Al_2O_3 addition on ZrO_2 phase composition in the Al_2O_3-ZrO_2 system”, Ceram. Int., 30, 923-926 (2004).

2.66. H. Mills and S. Blackburn, “Zirconia toughened aluminas by hydrothermal processing”, J. Eur. Ceram. Soc., 20, 1085-1090 (2000).

2.67. J. Chandradass, J. H. Yoon and D-S Bae, “Low temperature synthesis and characterization of zirconia doped alumina nanopowder by hydrothermal process”, Materials and Manufacturing Processes, 23, 138-142 (2008).

2.68. R. L. Coble, ‘‘Sintering of crystalline solids I: Intermediate and final stage diffusion models’’, J. Appl. Phys., 32, 787–792 (1961).

2.69. R. J. Brook, ‘‘Pore–Grain boundary interactions and grain growth’’, J. Am. Ceram. Soc., 52, 56–57 (1969).

2.70. E. A. Barringer and H. K. Bowen, ‘‘Formation, packing and sintering of monodispersed TiO_2 powders’’, J. Am. Ceram. Soc., 65, C199–201(1982).

2.71. C. P. Cameron and R. Raj, ‘‘Better sintering through green-state deformation processing’’, J. Am. Ceram. Soc., 73, 2032–2037 (1990).

2.72. A. Krell, P. Blank, H. W. Ha, T. Hutzler, and M. Nebelung, ‘‘Processing of High-Density Submicrometer Al_2O_3 for New Applications,’’ J. Am. Ceram. Soc., 86, 546–53 (2003).

2.73. A. Krell and J. Klimke, ‘‘Effect of the homogeneity of particle coordination on solid-state sintering of transparent alumina’’, J. Am. Ceram. Soc., 89, 1985–1992 (2006).

2.74. W. H. Rhodes, ‘‘Agglomerate and particle size effects on sintering yttria- stabilized zirconia’’, J. Am. Ceram. Soc., 64, 19–22 (1981).

2.75. T. S. Yeh and M. D. Sacks, ‘‘Effect of green microstructure on sintering of alumina’’; pp. 309–331 in Ceramics Transactions, Vol. 7, Sintering of Advanced Ceramics, Edited by C. A. Handwerkers, J. E. Blendell, and W. A. Kaysser. The American Ceramic Society, Westerville, OH, 1990.

2.76. F. F. Lange and B. J. Kellet, ‘‘Thermodynamics of densification, II. grain growth in porous compacts and relation to densification’’, J. Am. Ceram. Soc., 72, 735–741 (1989).

2.77. K. G. Ewsuk, J. G. Arguello, D. N. Bencoe, D. T. Ellerby, S. J. Glass, D. H. Zeuch, and J. Anderson, ‘‘Characterizing powders for dry pressing, sintering’’, Bull. Am. Ceram. Soc., 82, 41–47 (2003).

2.78. K. G. Ewsuk, ‘‘Consolidation of Bulk Ceramics’’; pp. 77–101 in Characterization of Ceramics, Edited by R. E. Loehman. Butterworth-Heinemann, Greenwich, 1993.

2.79. F. F. Lange, ‘‘Sinterability of agglomerated powders’’, J. Am. Ceram. Soc., 67, 83–89 (1984).

2.80. P.-L. Chen and I.-W. Chen, ‘‘Sintering of fine oxide powders: I, Microstructure evolution’’, J. Am. Ceram. Soc., 79, 3129–3141 (1996).

2.81. X.-H. Wang, P.-L. Chen, and I.-W. Chen, ‘‘Two-step sintering of ceramics with constant grain size: I. Y_2O_3’’, J. Am. Ceram. Soc., 89, 431–437 (2006).

2.82. K. Maca, M. Trunec, and P. Dobsak, ‘‘Bulk zirconia nanoceramics prepared by cold isostatic pressing and pressureless sintering’’, Rev. Adv. Mater. Sci., 10, 84–88 (2005).

2.83. K. Matsui, I. N. Ohmich, M. Ohgai, M. Enomoto and J. Hojo, ‘‘Sintering kinetics at constant rates of heating: Effects of Al_2O_3 on the initial sintering stage for fine zirconia powder’’, J. Am. Ceram. Soc., 88, 3346–3352 (2005).

2.84. K. G. Ewsuk and G. L. Messing, ‘‘A theoretical and experimental analysis of final-stage densification of alumina during hot isostatic pressing’’; pp. 23–33 in Hot Isostatic Pressing: Theory and Applications, Edited by R. J. Shaefer and M. Linzer. ASM International, Metals Park, OH, 1991.

2.85. M. P. Harmer, ‘‘Use of solid-solution additives in ceramics processing’’; pp. 679–96 in Advanced Ceramics, Vol. 10, Edited by W. D. Kingery. The American Ceramic Society, Westerville, OH, 1984.

2.86. H. H. Su and D. L. Johnson, ‘‘Master sintering curve: A practical approach to sintering’’, J. Am. Ceram. Soc., 79, 3211–3217 (1996).

2.87. J. D. Hansen, R. P. Rusin,M. H. Teng, and D. L. Johnson, ‘‘Combined stage sintering model’’, J. Am. Ceram. Soc., 75, 1129–1135 (1992).

2.88. H.E. Exner, "Principles of single phase sintering", Revs. Powder Met. Phys. Ceram. 1 (1979) 7.

2.89. K. S. Hwang and R. M. German, in "Sintering and heterogeneous catalysis", edited by G. C. Kuczynski, A. E. Miller and G. A. Sargent (Plenum Press, New York, NY, (1984) p. 35.

2.90. F.A. Nichols and W. W. Mullins, "Morphological changes of a surface of revolution due to capillarity-Induced surface diffusion”, *J. Appl. Phys.* 36, 1826 (1965).

2.91. R. M. German and J. F. Lathrop, “Simulation of spherical powder sintering by surface diffusion”, J. Mater, Sci., 13, 921 (1978).

2.92. D.L. Johnson, “New method of obtaining volume, grain-boundary, and surface diffusion coefficients from sintering data”, J. Appl. Phys., 40 ,192 (1969).

2.93. H.E. Exner and P. Bross, “Material transport rate and stress distribution during grain boundary diffusion driven by surface tension”, Acta Mat., 27, 1007 (1979).

2.94. P. Bross and H. E. Exner, “Computer simulation of sintering processes”, Acta Met. 27 (1979) 1013.

2.95. R.M. German, “Problems with computer simulation of sintering kinetics” Scripta Mat., 14, 955 (1980).

2.96. H.E. Exner, in "Sintering '87", Vol. 1, edited by S. Somiya, M. Shimada, M. Yoshimura and R. Watanabe (Elsevier, London, 1988) p. 291.

2.97. W.S. Young and I. B. Cutler, **“**Initial sintering with constant rates of heating”, J. Am. Ceram. Soc., 53, 659-663, (1970).

2.98. J.L. Woolfrey and M. J. Bannister, “Nonisothermal techniques for studying initial-stage sintering”, J. Am. Ceram. Soc, 55, 390-394 (1972).

2.99. J.J. Bacmann and G. Cizeron, “Dorn method in the study of initial phase of uranium dioxide sintering”, **J**. Am. Ceram. Soc, 51 ,209 (1968).

2.100. T.S. Wei and R. M. German, in "Modern developments in powder metallurgy", Vol. 15, edited by E. N. Aqua and C. I. Whitman (Metal Powder Industries Federation, Princeton, NJ, 1985) p. 307.

2.101. Y. Tomita, “Application of nonisothermal dilatometry for evaluation of kinetic parameters in nonreversing reactions”, J. Mater. Sci., 24, 731–735 (1989).

2.102. H. Hillman and R. M. German, “Constant heating rate analysis of simultaneous sintering mechanism in alumina”, J. Mater. Sci., 27, 2641–2648 (1992).

2.103. E. Sato and C. Carry, “Effect of powder granulometry an pretreatment on sintering behaviou of submicron-grained -alumina”, J. Eur. Ceram. Soc., 15, 9–16 (1995).

2.104. E. Sato and C. Carry, “Yttria doping and sintering of submicrometer-grained-alumina”, J. Am. Ceram. Soc., 79, 2156–2160 (1996).

2.105. J. Wang and R. Raj, “Estimate of the activation energies for boundary diffusion from rate-controlled sintering of pure alumina, and alumina doped with zirconia or titania”, J. Am. Ceram. Soc., 73, 1172–1175 (1990).

2.106. P. Duran, M. Villegas, F. Capel, and C. Moure, “Low temperature fully densified nanostructured Y-TZP ceramics”, J. Mater. Sci. Lett., 15, 741–744 (1996).

2.107. P. Duran, M. Villegas, F. Capel, and C. Moure, “Low temperature sintering and microstructural development of nanocrystalline Y-TZP Powders”, J. Eur. Ceram. Soc., 16, 945–952 (1996).

2.108. G. S. A. M. Theunissen, A. J. A. Winnubst, and A. J. Burggraf, “Sintering kinetics and microstructure development of nanoscale Y-TZP ceramics”, J. Eur. Ceram. Soc., 11, 315–324 (1993).

2.109. J. Wang and R. Raj, “Activation energy for the sintering of two-phase alumina/zirconia ceramics”, J. Am. Ceram. Soc., 73, 1172–1175 (1990).

2.110. V. Trombini, E.M.J.A. Pallone, U. Anselmi-Tamburini, Z.A. Munir and R. Tomasi, “Characterization of alumina matrix nanocomposite with ZrO_2 inclusions densified by spark plasma sintering**”,** Mat. Sci. and Engg. A*,* 501, 26-29 (2009).

2.111. Y. Ye, J. Li, H. Zhou and J. Chen, “Microstructure and mechanical properties of yttria-stabilized ZrO_2/Al_2O_3 nanocomposite ceramics”**,** Ceram. Int., 34, 1797-1803 (2008).

2.112. R.R. Menezes and R.H.G.A. Kiminami, "Microwave sintering of alumina-zirconia nanocomposites**"**, J. of Mat. Proc. Tech., 203, 513-517 (2008).

2.113. K. Matsui, T. Yamakawa, M. Uehara, N. Enomoto and J. Hojo, "Mechanism of alumina-enhanced sintering of fine zirconia powder: Influence of alumina concentration on the initial stage sintering"**,** J. Am. Ceram. Soc., 91, 1888-1897 (2008).

2.114. H. Huang, Z. Shao, G. Wang and H. Ai, "Preparation of ZrO_2 and Al_2O_3 composite powder by gel co-precipitation method"**,** Chin. J. Mat. Res. 22 , 246-250 (2008).

2.115. M. Nagashima and M. Hayakawa, "Grain growth behavior of Al_2O_3-ZrO_2 with a small amount of zirconia", Mat. Sci. Forum 561-565 (PART 1), 535-538 (2007).

2.116. K. Matsui, T. Yamakawa, M. Uehara, N. Enomoto and J. Hojo, "Sintering mechanism of fine zirconia powders with alumina added by various ways", Key Eng. Mat., 352, 219-222 (2007).

2.117. J.K.M.F. Daguano, C. Santos, R.C. Souza, R.M. Balestra, K. Strecker and C.N. Elias, **"**Properties of ZrO_2-Al_2O_3 composite as a function of isothermal holding time", Int. J. Ref. Met. and Hard Mat., 25, 374-379 (2007).

2.118. R.P. Rana, S.K. Pratihar, S. Bhattacharyya, **"**Powder processing and densification behaviour of alumina-high zirconia nanocomposites using chloride precursors", J. Mat. Proc. Tech., 190, 350-357 (2007).

2.119. S. Tekeli, U. Demir, "Colloidal processing, sintering and static grain growth behaviour of alumina-doped cubic zirconia", Ceram. Int., 31, 973-980 (2005).

2.120. R. Chaim, "Pressureless sintered ATZ and ZTA ceramic composites", J. Mat. Sci., 27, 5597-5602 (1992).

2.121. A. Krell, P.Blank and T. Weiss, "Influence of microcracking and homogeneity on the mechanical behavior of (Al_2O_3+ZrO_2) ceramics", J. Mat.Sci., 22, 3304-3308 (1987).

2.122. M. Hirano and H. Inada , "Fracture toughness ,strength and Vickers hardness of Yttria-Ceria- doped tetragonal zirconia/alumina composites fabricated by hot isostatic pressing", J. Mat.Sci.,27, 3511-3518 (1992).

2.123. O. N. Grigoryev, S. A. Firstov, O. A. Babiy, N. A. Orlovskaya and G.E. Homenko, “Effect of zirconia (3 mol% yttria) additive on mechanical properties and structure of alumina ceramics”, J. Mat.Sci.,29, 4633-4638 (1994).

2.124. V.V. Srdic and R.Radonjic, “Transformation toughening in sol-gel derived alumina-zirconia composites”, J. Am. Ceram. Soc., 80, 2056-2060 (1997).

2.125. K.J. Konsztowicz and L. Radonjic, “Effects of heteroflocculation of powders on mechanical properties of zirconia alumina composites”, J. Mat.Sci., 31 1633-1641 (1996).

2.126. M. Balasubramanian, S. K. Malhotra and C.V. Gokularathnam, “Sintering and mechanical properties of sol-gel derived alumina-zirconia composites”, J. Mat. Proc. Tech., 67, 67 -70(1997).

2.127. D. Casellas, I. Rafols,L. Llanes and M. Anglada , “Fracture toughness of zirconia-alumina composites”, Int. J. of Ref. Metals and Hard Materials, 17,11-20 (1999).

2.128. J. Vleugels, Z.X. Yuan and O. Van Der Biest, “Mechanical properties of Y_2O_3/Al_2O_3-coated Y-TZP ceramics”, J. Eur. Ceram. Soc., 22, 873–881(2002).

2.129. T.Adachi, T.Sekino, T.Kusunose, T.Nakayama, A.Hikasa, Y.H.Choa and K.Hihara, “Crack propagation behaviour of nano-sized SiC dispersed multilayered Al_2O_3-3Y-TZP hybrid composites”, J.Ceram. Soc. Jpn, 111, 4-7 (2003).

2.130. A.Celli, A.Tucci, L.Esposito and C.Palmonasi, “Fractal analysis cracks in alumina-zirconia composites”, J. Eur. Ceram. Soc., 23,469–473 (2003).

2.131. J.K. Han, F. Saito and B.T.Lee, “Microstructures of porous Al_2O_3–50 wt % ZrO_2 composites using in-situ synthesized Al_2O_3–ZrO_2 composite powders”, Mat. Lett. 58, 2181–2185 (2004).

2.132. F. Cesari, L. Esposito, F.M. Furgiuele, C. Maletta, and A. Tucci, “Fracture toughness of alumina-zirconia composites”, Ceram. Int., 32,249-255 (2005).

2.133. O. Vasylkiv, Y. Sakka and V.V. Skorohod, “High-toughness of tetragonal zirconia/ alumina nano-ceramics”, Key Engg. Mats. , 317-318, 615-618 (2006).

2.134. B. Basu, J. Vleugels and O. Van Der Biest, “ZrO_2 –Al_2O_3 composites with tailored toughness”, J. Alloys and Compounds, 372, 278-84 (2004).

2.135. S. Novak, M. Kalin, P. Lukas, G. Anne, J. Vleugels and O. Van Der Biest, "The effect of residual stresses in functionally graded alumina–ZTA composites on their wear and friction behaviour", J. Eur. Ceram. Soc., 27,151–156 (2007).

2.136. R.Bermejo, J.Pascual, T.Lube and R.Danger, "Optimal strength and toughness of Al_2O_3–ZrO_2 laminates designed with external or internal compressive layers", J. Eur. Ceram. Soc., 28, 1575–1583 (2008).

2.137. C.F. Gutiérrez-González and J.F. Bartolomé, "Damage tolerance and **R**-curve behavior of Al_2O_3–ZrO_2–Nb multiphase composites with synergistic toughening mechanism", J. Mater. Res., 23, 570-578 (2008).

2.138. M. Weimin, W. Lei, G. Renguo, S. Xudong and L. Xikun, "Sintering densification, microstructure and transformation behavior of Al_2O_3/ZrO_2 (Y_2O_3) composites", Mat. Sci. & Engg. A 477, 100–106 (2008).

2.139. F. A.T. Guimarães, K. L. Silva, V. Trombini, J.J. Pierri, J. A. Rodrigues, R. Tomasi and E.M.J.A. Pallone, "Correlation between microstructure and mechanical properties of Al_2O_3/ZrO_2 nanocomposites", Ceram. Int., 35,741-745 (2009).

2.140. X. Q. Liu and X. M. Chen, "Effects of $Sr_2Nb_2O_7$ additive on microstructure and mechanical properties of 3Y–TZP/Al_2O_3 ceramics", Ceram. Int., 28,209-215 (2002).

2.141. X.Jin and L. Gao, "Effects of powder preparation method on the microstructure and mechanical performance of ZTA/$LaAl_{11}O_{18}$ composites", J. Eur. Ceram. Soc., 24,653–659 (2004).

2.142. G. Yang, J. Li, G. Wang, M. Yashima and S. Min, "Influences of ZrO_2 nanoparticles on the microstructure and mechanical behavior of Ce-TZP/Al_2O_3 nanocomposites", J. Mat.Sci., 40, 6087-6090 (2005).

2.143. A. Balakrishnan, B.B. Panigrahi, K.P. Sanosh, Min-Cheol Chu, T.N. Kim and Seong-Jai Cho, "Mechanical properties of MgO–Al_2O_3–SiO_2 glass-infiltrated Al_2O_3–ZrO_2 composite", J. Mat. Proc. Tech., 209, 5271 -5275 (2009).

2.144. A. N-Rascon, A. A-Elguezabal, E. Orrantia and M.H. B-Bernal, "On the wide range of mechanical properties of ZTA and ATZ based dental ceramic composites by varying the Al_2O_3 and ZrO_2 content", Int. J. of Ref. Metals and Hard Materials, (2009).

2.145. I. Ganesh, S. M. Olhero, P. M.C. Torres, F. J. Alves and J.M.F. Ferreira, "Hydrolysis-induced aqueous gelcasting for near-net shape forming of ZTA ceramic composites", J. Eur. Ceram. Soc., 29, 1393–1401 (2009).

2.146. A. Z. A. Azhar, M.M. Ratnam and Z.A. Ahmad, "Effect of Al_2O_3/YSZ microstructures on wear and mechanical properties of cutting inserts", J. Alloys and Compounds, 478 ,608–614 (2009).

Chapter III

Statement of Problem

Extensive literature review on Al_2O_3–ZrO_2 composites led to conclude that in recent times, solution chemistry routes (sol – gel, gelation, combustion synthesis etc) were mainly used for the composite powder processing, though solid state route of composite preparation was not totally neglected. Most of the investigations involving Al_2O_3–ZrO_2 composites were carried out either in the ZTA zone (ZrO_2= 5-35 vol %) or in ATZ zone (ZrO_2=70 – 95 vol %). In all the investigations on Al_2O_3-ZrO_2, ZrO_2 was added as stabilized ZrO_2 (Y-TZP/Ce – TZP being most common), although some investigators have studied Al_2O_3 – undoped ZrO_2 composites. However, very few literatures were available for Al_2O_3–ZrO_2, prepared from equal volume fraction of Al_2O_3 and ZrO_2. There may be two possible reasons why this particular composition was not investigated. One of them relates to the possible instability of tetragonal ZrO_2 (on account of lowered composite elastic modulus) and the other reason may be the increased softness of the composite which may limit the use of this composite.

But it is quite possible that through controlled processing, Al_2O_3– high ZrO_2 composite may be developed in which as a result of transformation toughening, reasonable strength, toughness and hardness will result. Thus, the present study aims to study these specific aspects from a processing view point:

I Use of different powder processing methods on the powder properties, its optimization and t-ZrO_2 retention. This aspect will be studied using three different powder processing routes, viz. gelation, precipitation and washing of the precipitates prior to calcination.

II Effect of precursor type (or nature of anions) on the metastable phase evolution and densification behaviour as well as properties of similar composites. To study this effect two different precursor combination will be used- all chloride ($AlCl_3$ and $ZrOCl_2$) and nitrate- chloride combination ($Al(NO_3)_3$ and $ZrOCl_2$)

III Detailed densification mechanism of the composites during initial stage sintering. This particular study is being planned using isothermal and non isothermal sintering behavior.

IV Effect of stabilizer on the composite properties, microstructures, strength, toughness and hardness. This part will be studied in Al_2O_3-Y-ZrO_2 composites where Y_2O_3 of different concentration (viz 1, 2, 2.5,3 mol %) will be added during powder preparation stage with a view to stabilize the tetragonal ZrO_2.

V Exploring the possible strengthening and toughening mechanism in these composites. To study this part, the observed strength, toughness and hardness values will be correlated with microstructure, density and different toughening and strengthening models. An attempt will also be made to explore the possibility of a second phase on the strength, toughness thermo-mechanical properties of the composites.

Chapter IV

Experimental Work

Alumina-zirconia composites having nominally equal volume of Al_2O_3 and ZrO_2 were prepared by gel-precipitation and precipitation method. The precursors for Al_2O_3 were $AlCl_3$ (Merck,India), $Al(NO_3)_3 .9H_2O$ (Merck,India) and $ZrOCl_2.8H_2O$(Loba,India) for zirconia. Separate stock solution of individual precursors $AlCl_3$, $Al(NO_3)_3 .9H_2O$ and $ZrOCl_2.8H_2O$ were prepared by dissolving them in double distilled water. Each of the solution was 0.75 mol/Lit. Before proceeding with powder preparation from these precursors, it was necessary for quantitative estimation of these precursor stock solutions.

4.1 Estimation of $AlCl_3$, $Al(NO_3)_3$, and $ZrOCl_2$ stock solution

3 ml of respective stock solution was taken in a clean and dried 250 ml volumetric flask. 2-3 drops of methyl-red indicator was added to the solution and the colour changed to pink for $ZrOCl_2$ and light pink for both $AlCl_3$ and $Al(NO_3)_3$ solution. The stock solution was titrated with AAC buffer solution (NH_4OH & NH_4Cl) with continuous stirring. The complete precipitation of $Al(OH)_3$ (or $Zr(OH)_4$) took place between pH of 9 and 10. The end point of the reaction was marked by the change in the solution colour from pink to light pink to pale yellow. The precipitate was warmed and filtered through Whatman 40 filter paper and washed with hot water to make the precipitate free from chloride, nitrates and excess AAC buffer. The washing was continued till the precipitate colour changed to white. The precipitate along with the filter paper was transferred to a preweighed platinum crucible and fired at 1000°C for 1 hr. The weight of the calcined precipitate on firing was equivalent to weight of the oxide per 3 ml of solution. The possible chemical reactions during precipitation are as follows:

$$AlCl_3 + NH_4OH = Al(OH)_3 + 3NH_4Cl \qquad (4.1)$$

$$Al(NO_3)_3 + NH_4OH = Al(OH)_3 + 3NH_4NO_3 \qquad (4.2)$$

$$ZrOCl_2 + NH_4OH = ZrO(OH)_2 + 3NH_4Cl \qquad (4.3)$$

$$ZrO(OH)_2 + NH_4OH = ZrO(OH)_2 + 2NH_4Cl \qquad (4.4)$$

The precipitated $Al(OH)_3$ and $Zr(OH)_4$ could be correlated to their respective oxides according to the following equations:

$$Zr(OH)_4 = ZrO_2 + 2H_2O \qquad (4.5)$$

$$ZrO(OH)_2 = ZrO_2 + H_2O \qquad (4.6)$$

$$2Al(OH)_3 = Al_2O_3 + 3H_2O \qquad (4.7)$$

4.2 Powder Synthesis

Al_2O_3-50 vol% ZrO_2 composite powder was prepared from solution chemistry routes using aluminum chloride and zirconium oxychloride as precursors. Three different processing routes, viz gelation (ROUTE 1), precipitation (ROUTE 2) and precipitation followed by washing (consisting of hot water and alcohol washing) (ROUTE 3) were employed for preparing the composite powder. In the later stage, further modification of ROUTE 3 was made by replacing $AlCl_3$ with $Al(NO_3)_3$ (ROUTE 4).

4.2.1 Synthesis of Alumina-Zirconia Powder by Gelation Method (ROUTE 1)

Alumina-zirconia powder, containing 50 vol% Al_2O_3 and ZrO_2 has been prepared from the pre-estimated precursor solutions of aluminum chloride ($AlCl_3$, AR grade) and zirconium oxychloride ($ZrOCl_2.8H_2O$, AR grade). The two precursor solutions were mixed thoroughly at room temperature; the pH of the mixed solution was found to be less than 2. The mixed precursor solution was subjected to gelation by drop wise addition of NH_4OH (AR grade) while the mixed solution was being vigorously stirred on a magnetic stirrer. The colour of the mixed solution changed from pale yellow to colourless on addition of few initial drops of NH_4OH. Further addition of NH_4OH resulted in the formation of few white flocks of precipitates which increased in number finally leading to the complete gelation of the formed precipitates (pH 6.5 - 6.7) [4.1]. Figure 4.1 shows the process flow diagram and the gelation route (ROUTE 1) is step 1-3 and 9.

4.2.2 Synthesis of Alumina-Zirconia Powder by Precipitation from Chloride Precursors (ROUTE 2)

In the precipitation route, $AlCl_3$ and $ZrOCl_2$ precursor solutions were mixed as before (section 4.2.1). With addition of NH_4OH, at first gelation of the entire solution took place in the pH range 6 - 6.5. Following this, the gel network was mechanically disturbed by high speed stirring and NH_4OH addition was continued till the precipitation was complete (pH range 8.7 - 9.1) [4.2]. The precipitates were allowed to settle and the clear supernatant liquid contained NH_4OH, NH_4Cl and NH_4NO_3 which was removed by decantation. The precipitate was dried and ground to a fine powder and characterized. Figure 4.1 shows the process flow diagram and the precipitation route (ROUTE 2) is steps 1-6 and 8-9.

4.2.3 Preparation of Alumina-Zirconia Composite Powder from Washed Precipitates using Chloride Precursors (ROUTE 3)

The precipitates were prepared following the steps mentioned in section 4.2.2. The precipitates were allowed to settle and the clear supernatant liquid was removed. Following this, the precipitates were washed with hot water for several times. Between each washing step, the precipitate was settled and the clear liquid was removed. The washing was continued till the precipitate was white in colour. This water washed precipitated was further washed with isopropyl alcohol. In order to facilitate better and faster washing by isopropyl alcohol, this stage of washing was carried in a laboratory centrifuge to separate the liquid and precipitates. Figure 4.1 shows the process flow diagram and the washed precipitate route (ROUTE 3) is steps 1-9.

4.2.4 Preparation of Alumina-Zirconia Composite Powder from Washed Precipitates using Chloride-Nitrate combined Precursors (ROUTE 4)

It has been reported that entrapped ions (Cl^-) as well as water affects the densification process and therefore, it was necessary to remove both of these during the powder preparation steps. In ROUTE 4 this was realized by replacing $AlCl_3$ by $Al(NO_3)_3$ and making the precipitate by similar route as in section 4.2.2 and carrying out the post precipitation washing process (water and alcohol washing) as mentioned in section 4.2.3. Later on, a further modification of ROUTE 4 was made when $Y(NO_3)_3$ was also introduced in the system. The partially modified ROUTE 4 was used to prepare Al_2O_3-Y-ZrO_2 composite powder from co-precipitation of $Al(NO_3)_3$, $ZrOCl_2$ and $Y(NO_3)_3$ solution. Thus, for the preparation of Al_2O_3-Y- ZrO_2 composite powder (Y_2O_3 = 1, 2, 2.5 and 3 mol%), the required amount of Y_2O_3 (Loba India) was added to 1:1 HNO_3 and the mixture was warmed for complete dissolution of Y_2O_3 in HNO_3 .The $Y(NO_3)_3$ solution thus prepared was added to the mixed solution of $Al(NO_3)_3$ and $ZrOCl_2$ and the precipitation was carried out following similar method as discussed in the section 4.2.3. Figure 4.1 shows the process flow diagram and the washed precipitate route (ROUTE 4) is steps 1-9 using precursors given in second column.

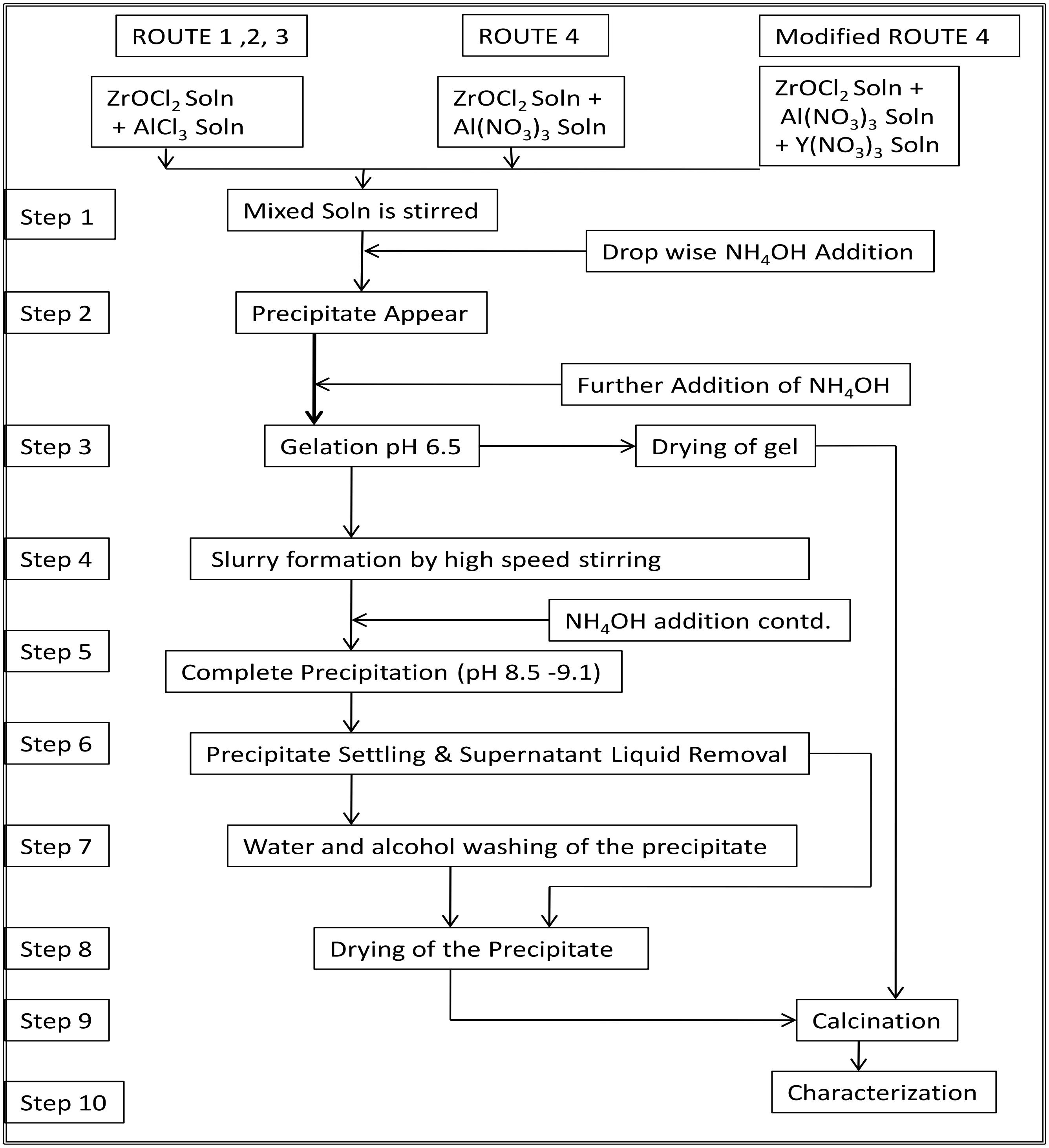

Fig.4.1. Generalized flow diagram for processing of Al_2O_3-50 vol% ZrO_2 composite powder preparation by different routes

4.3 Characterization of Dried Gel and Calcined Powder

The dried gel was characterized for its thermal decomposition behaviour by (DSC/TG), the presence of different ions and hydroxides by FTIR, and phase analysis by XRD. Subsequently, the gel powder was calcined for 4 hrs. at different temperatures between 350-1050°C and the phase evolution, particle size distribution, surface area, compaction behaviour and particle morphology of the calcined powder has also been studied.

4.3.1 DSC/TG of Dried Gel/Precipitate

The thermal analysis of the dried gel/precipitate gives an idea about the decomposition and crystallization behavior of hydroxides present in the gel/precipitate. A small quantity of finely ground dried gel/precipitate was subjected to DSC/TG study (Netzsch STA409 C) in an ambient atmosphere at a heating rate of 10°C/minute using α-Al_2O_3 as reference material.

4.3.2 Fourier Transform Infrared Spectroscopy (FTIR)

The different ions and metal hydroxides in the dried gel/precipitate and calcined powder have been studied through FTIR. The powder sample was mixed with KBr in an agate mortar and pressed to a pellet of 0.1 mm thickness. The spectra were taken in a diffuse reflectance (DRIFT) mode in a Shimadzu FTIR instrument (Model 84005) in the wave number range 4000 - 400 cm^{-1}.

4.3.3 Calcination

All the powder prepared by ROUTE 1- ROUTE 4 calcined at different temperature 350 – 1050°C with a 4 hrs holding time at the peak temperature.

4.3.4 Crystallite Size, Phase Analysis of Dried Gel, Precipitate and Calcined Powder

The phase analysis of dried gel, precipitate as well as calcined powder was carried out with an X-ray diffractometer (Phillips PW 1830, Holland) with Cu-Kα radiation in the 2θ range 20-80 ° at a scan speed of 2°/min. The accelerating voltage and current were 35kV and 30mA respectively. The crystallite size of the powder was calculated from X-ray line broadening using Scherrer’s formula [4.3].

$$D = \frac{0.9\lambda}{B\cos\theta} \tag{4.8}$$

where, D is the crystallite size, λ is the wavelength of the radiation, θ is the Bragg's angle and B is the full width at half maximum

$$B^2 = B^2_{meas.} - B^2_{inst.} \tag{4.9}$$

where, B_{meas}= Observed full width at half maximum from peak values, $B_{inst.}$ = Instrumental broadening.

The fraction of tetragonal zirconia was calculated by comparing the peak intensities of tetragonal [111] and monoclinic [111] and [$11\bar{1}$] obtained from X-ray diffraction of calcined as well as sintered samples using the following Eqn. [4.4, 4.5].

$$V_m = \frac{1.311X_m}{(1+0.311X_m)} \tag{4.10}$$

where, $$X_m = \frac{I_m(111) + I_m(11\bar{1})}{I_m(111) + I_t(111) + I_m(11\bar{1})} \times 100 \tag{4.11}$$

where, V_m is the volume fraction of monoclinic ZrO_2, *I*= integrated intensity of the respective diffracting plane, X_m is the intensity of m-ZrO_2 with respect to total ZrO_2, subscript m and t stands for monoclinic and tetragonal ZrO_2.

4.3.5 Particle Size Distribution

The particle size and size distribution of the calcined powder has been studied by laser scattering technique (Malvern MASTER SIZER 2000, U.K.). The scattering of the light by the particle depend on the refractive index of the powder, dispersant and medium. The refractive index and bulk density of both the medium and samples was determined before carring out the particle size distribution. The density of the powder was determined by pycnometer method using kerosene as medium. The calcined powder was ultrasonically dispersed in water using sodium hexametaphosphate as dispersant. The D_{50} was determined from the size frequency curve which was calculated on the basis of the surface to volume ratio of particle.

4.3.6 Surface Area of Calcined Powder

The specific surface area of the calcined powder was measured by BET surface area analyzer (Quantachrome Instruments, U.S.A.) which is based on the adsorption of nitrogen gas on the sample surface. The calcined powder was degassed at 100^{o}C and measurement was done at five different points. The average particle size is the diameter of the spheres equivalent to exterior surface area. Assuming spherical particles, the particle size (d_{BET}) has also been calculated from surface area according to Eqn. (4.10).

$$d_{BET} = \frac{6}{S_p \rho} \text{(Spherical approximation)} \qquad (4.12)$$

where, d_{BET} = average particle diameter, Sp = specific surface area (m^2 gm^{-1}); ρ= true density of the material.

4.3.7 Compaction Behaviour of Powder

The packing characteristic of particles, stress induced flow behaviour and the agglomeration strength of calcined powder were studied from the logarithmic pressure-relative density diagram. Compaction behaviour and agglomerate strength of the powder has been measured by uniaxially compaction of the powder in circular die and punch. The weighed amount of powder was taken in a stearic acid lubricated die and punch. The powder was properly leveled and the initial height was of the powder was measured. The punch movement was measured using universal testing machine (UTM) (Hounsfield H50KT, UK) at a constant crosshead speed of 0.2 mm/min. The green density of the powder compact has been calculated from the punch movement and the initial height of the powder.

4.3.8 Microstructure of Calcined Powder

The morphology of the calcined powder i.e. agglomeration behaviour, particle size and shape were studied in TEM (PHILIPS CM200T, CANADA). The TEM sample was prepared by dispersing a small amount of powder in isopropyl alcohol followed by ultrasonication (20 KHz, 500 W) for 20 min. One drop of the well-dispersed suspension was deposited on a 400 mesh carbon coated copper grid. The grid was dried in an IR lamp for solvent evaporation. The powder was observed in bright field at an accelerating voltage of 200 KV.

4.4 Densification Behaviour

4.4.1 Sintering Kinetics

The sintering kinetics of Al_2O_3-ZrO_2 composite powder was studied by both isothermal and constant rate heating method. In the constant rate heating method, the green rectangular bars of Al_2O_3-ZrO_2 composite was sintered at different heating rate (5,10, 15, 20°C/min) till 1450°C in ambient atmosphere in a dilatometer (NETZSCH DL 402C).The activation energy for mass transport during initial stage of sintering was calculated from the shrinkage data at different temperatures. In isothermal method, the green compact was rapidly heated @ 20°C/min to the desired temperatures (1050-1450°C) and held at that temperature for 2 hrs.

4.4.2 Sintering of Green Compacts

The green compacts were placed on alumina substrate and heated from room temperature to 650°C at a rate 4°C /min and held there for 30 min. for binder removal. Thereafter, the samples were heated at a rate 3°C/min to the final sintering temperature (1400-1600°C) at 50°C interval with a hold time of 4 hrs. at each sintering temperatures. The samples were also sintered for various soaking periods i.e. 6 hrs, 8 hrs at 1600°C. The samples were cooled at 3°C /minute till 900°C followed by furnace cooling.

4.5 Characterization of Sintered Samples

The sintered samples were studied for phase analysis of Al_2O_3 and ZrO_2, density, mechanical properties, thermal expansion behaviour and microstructural study by SEM.

4.5.1 Phase analysis of Sintered Sample

The phase in the sintered compacts was studied by X-ray diffraction using Cu K_α radiation. The samples were scanned in the 2θ ranges 20-80° and the obtained XRD pattern was analyzed using Schmid's formula as described in section 4.3.4.

4.5.2 Bulk Density and Relative Density of Sintered Specimen

The bulk density and apparent porosity of the sintered specimen were measured by Archimedes’ principle using kerosene as the immersion liquid. The bulk density was calculated using the suspended and soaked weights.

$$Bulk\ Density = \left(\frac{D \times Density\ of\ Kerosene}{W - S}\right) \qquad (4.13)$$

where, D, W, and S are the dry weight, soaked weight and suspended weight of the sample.

The relative densities of the sintered samples were measured from the bulk density and the theoretical density calculated from the x-ray phase analysis.

$$Relative\ Density = \frac{Bulk\ Density}{[(X_t \times 6.1 + X_m \times 5.89) \times 0.2] + (3.98 \times 0.8)} \qquad (4.14)$$

where, X_t and X_m are the volume fraction of tetragonal and monoclinic ZrO_2.

4.5.3 Microstructure of Sintered Specimen

The microstructures of the sintered ZTA composites were observed by SEM, FE-SEM and TEM. The samples were polished using automatic grinding & polishing unit (Buehler, Ecomet 3-Automet 3). At first, the specimen surface was ground successively using 240 and 600 grit SiC paper disks respectively. Following this, the samples were polished in 1μm diamond paste on a texmet cloth. The polished samples were washed by acetone and cleaned with in an ultrasonic bath. The polished samples were chemically etched for 15 min in a 1:1:2 :: HF: HNO_3: H_2O solution. The chemically etched samples were washed, dried and thermally etched for 20 min at 150^0C below the sintering temperature.

4.5.3.1 SEM/FE-SEM Analysis

The polished and etched samples were sputter coated with palladium-platinum coating in a sputtering unit for 2-3 min. to make the surface conducting. The specimens were observed by SEM (JEOL- JSM 6480 LV, Japan) in BSE and SE mode at 15 KV accelerating voltage. Fracture and indented surface of some samples were also observed by SEM in both SE and BSE mode. Some selected sintered and thermally etched samples were also observed in FE-SEM (SIRION, PHILIPS, Eindhoven, Holland) at an accelerating voltage of 10 KV in SE and BSE mode.

4.5.3.2 TEM of bulk sintered samples

Some selected bulk sintered samples were also observed in TEM (TECNAI-G2, FEI USA), at 200 KV. The samples were prepared by argon ion milling.

4.6 Hardness, Strength and Toughness

Hardness, flexural strength and toughness of the sintered samples were measured on rectangular bars of size 45 x 4 x 4 mm^3. All the surfaces of the samples were polished and the edges were also chamfered. The dimetral compression test was carried out on cylindrical pellet (2-4 mm thick and 10-12 mm dia.) which were polished to remove roughness. The longitudinal edges of the specimens were chamfered by polishing to eliminate the edge cracks and stress.

4.6.1 Vickers Hardness

The hardness was studied by a Vickers semi-macro hardness tester (LV-700 Leco, Japan).The indentations were carried out at different loads (5, 10, 15, 20 Kgf) with 15 sec dwell time. The hardness (H_v) was determined from the diagonal length using the formula given below [4.6].

$$H_v = 0.47 \times \frac{P}{a^2} \tag{4.15}$$

where, P is the applied load in Newton and a is the half diagonal length in µm. The hardness was calculated from the slope of the plot of applied load and square of the half diagonal (a^2) at no crack condition of the indent using the above relation.

4.6.2 Flexural Strength

Flexural strength was determined in three-point bending as per ASTM standard C1161-90 [4.7] and by Brazilian disk test methods in UTM (Hounsfield H10KS, U.K). For three point bending, the span length was 25 mm and cross head speed was 0.2 mm/min. The flexural strength was calculated from the following equation [4.7].

$$\sigma_{flexural} = \left(\frac{3PL}{2WD^2} \right) \tag{4.16}$$

where, P is the fracture load, *L* is the span length, W is the width and D is the breadth of the sample**.**

The biaxial flexural strength of sintered samples was measured on the cylindrical samples. This test is also known as Brazilian disc test. In this test, the samples were broken in compression at a cross head speed of 0.2 mm/sec. The strength was calculated from the formula [4.8].

$$\sigma_{biaxial\ \ flexural\ \ strength} = \frac{2P}{\pi D t} \tag{4.17}$$

where, P is the breaking load, D is the diameter of the pellet and t is the thickness of the pellet.

4.6.3 Fracture Toughness

The fracture toughness of the sintered and notched specimen was determined in three point bending using SENB method [4.9] on notched samples. The notches were made using a Buehler low speed saw. The notched samples were pre-cracked by putting an indentation at notch tip. The fracture toughness K_{IC} was calculated by the following Eqn. [4.10].

$$K_{IC} = \frac{3PLC^{1/2}}{2WD^2}\left[A_0 + A_1\left(\frac{C}{D}\right) + A_2\left(\frac{C}{D}\right)^2 + A_3\left(\frac{C}{D}\right)^3 + A_4\left(\frac{C}{D}\right)^4\right] \tag{4.18}$$

where, P is the breaking load, C is the notch depth, W is the width, L is the span length, D is the depth or thickness of the sample. A_0, A_1, A_2, A_3 and A_4 are the constants and their values are calculated as following:

$$A_0 = 1.9 + 0.0075(L/D)$$

$$A_1 = -3.39 + 0.08(L/D)$$

$$A_2 = 15.4 - 0.2175(L/D)$$

$$A_3 = -26.24 + 0.2815(L/D)$$

$$A_4 = 26.38 - 0.145(L/D)$$

4.7 Thermal Shock Resistance

The thermal shock resistance of the sintered specimen evaluates the resistance to crack initiation or its propagation under thermal stress when subjected to a thermal shock from high temperature (such as rapidly cooling down from high temperature to low temperature). The thermal shock resistance was studied by heating the samples at 5°C /min up to a temperature of 1000, 1100 and 1200°C with a soaking time of 30 min at each temperature and followed by rapid cooling in air till the samples attained room temperature following the method of Li et al. [4.11]. The thermal shock resistance was determined by measuring flexural strength, tensile strength and fracture toughness after thermal shock. The phase analysis of the thermally shocked sample was also carried out to study the phase change due to thermal shock.

References

4.1 R.P. Rana, S.K. Pratihar and S. Bhattacharyya, “Effect of powder treatment on the crystallization behaviour and phase evolution of alumina- high zirconia nanocomposites”, J. Mater. Sci. 41, 7025–7032 (2006).

4.2 R.P. Rana, S.K. Pratihar and S. Bhattacharyya, “Powder processing route and densification behaviour of alumina – high zirconia composites using chloride precursors” J. Mat. Pro. Tech., 190, 350-357 (2007).

4.3 B.D. Cullity, Elements of X-Ray Diffraction, 2nd Ed, Addison-Wesley. INC, (1978).

4.4 R. Garvie and P. S. Nicholson, “Phase analysis in zirconia system”. J. Am. Ceram. Soc., 55, 303–305 (1972).

4.5 H. Toraya, M. Yoshimura and S. Somiya, “Calibration curve for quantitative analysis of the monoclinic-tetragonal ZrO_2 system by X-ray diffraction”. J. Am. Ceram. Soc., 67, 119–121(1984).

4.6 ASTM: C1327-99, Standard test method for Vickers indentation hardness of advanced ceramics, pp.1-8 (1999).

4.7 ASTM C1161-90, Standard test method for flexural strength of advanced ceramics at ambient temperature, Annual Book of ASTM Standards, Vol. 15.01. ASTM, pp. 327-333 (1991).

4.8 A.T Procopio, A. Zavaliangos and J.C. Cunningham, “Analysis of the diametrical compression test and the applicability to plastically deforming materials”, J. Mat. Sc. 38, 3629-3639 (2003).

4.9 ASTM: C-1421-99, Standard test method for determination of fracture toughness of advanced ceramics at ambient temperature, pp.1-32 (1999).

4.10 D.R. Larson, J.A. Coppola, D.P.H. Hasselman and R.C. Bradt, “Fracture Toughness and spalling behavior of high-Al_2O_3 refractories”, J.Am.Ceram.Soc, 57, 417-421(1974).

4.11 Z Li, J Liu , S Li and H Du, “Microstructure, mechanical properties and thermal shock resistance of ZrO_2–$LaPO_4$ composites”, Journal of Alloys and Compounds Vol 480, Issue 2, Pages 863-866, 8 July 2009.

Chapter V

Results and discussion

Section A

Processing and Characterization of Al_2O_3-ZrO_2 (undoped) Composites

5.1 Preparation of Al_2O_3-ZrO_2 Composite by Gelation Method (ROUTE 1)

The powder processing of Al_2O_3-ZrO_2 composites containing nominally equal volume fraction of Al_2O_3 and ZrO_2 prepared by gelation technique have been elaborated in section 4.2.1. The properties of the powder and the sintered compacts are discussed in the following sections.

5.1.1 Phase Analysis of Dried Gel

The XRD pattern of the dried gel is shown in Fig.5.1. The XRD pattern shows that the dried gel is amorphous with crystalline peaks superimposed on the amorphous broad background. These crystalline peaks were identified as NH_4Cl [JCPDS 73-0365], which formed during the gelation process due to the reaction between $AlCl_3$, and $ZrOCl_2$ with NH_4OH.

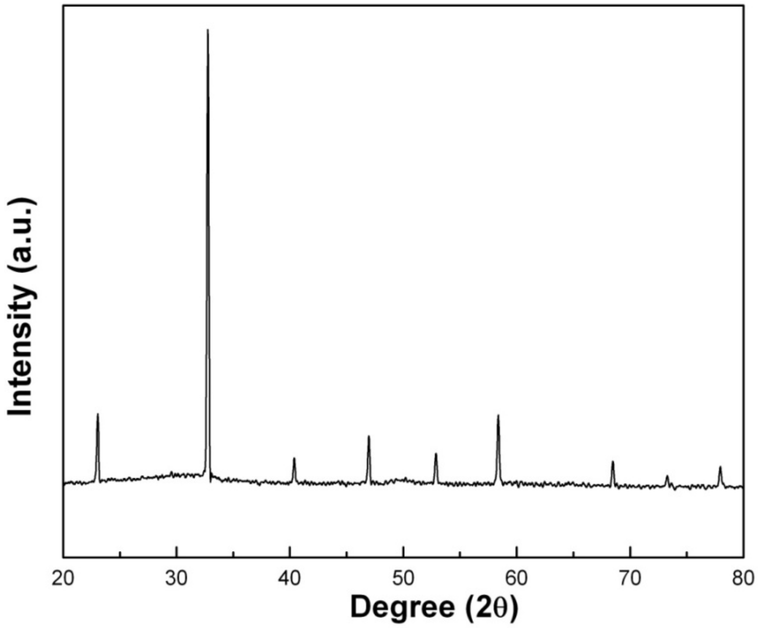

Fig.5.1. XRD pattern of dried gel (ROUTE 1)

5.1.2 Thermal Analysis of Dried Gel

Figure 5.2 shows the DSC/TG curve of as dried gel. The first broad endothermic peak at 100°C is associated with a weight loss of 13.7% (which continues till about 200°C).This endothermic peak and the weight loss is due to the dehydroxylation of $Al(OH)_3$. The governing chemical reaction is given by:

$$2AlCl_3 + 6NH_4OH = 2Al(OH)_3 + 6NH_4Cl \quad (5.1)$$

$$2Al(OH)_3 = Al_2O_3 + 3H_2O \quad (5.2)$$

Beside the decomposition of $Al(OH)_3$, the other chemical reactions occurring during the gelation can be written as follows:

$$ZrOCl_2 + 2NH_3 + 3H_2O = Zr(OH)_4 + 2NH_4Cl \quad (5.3)$$

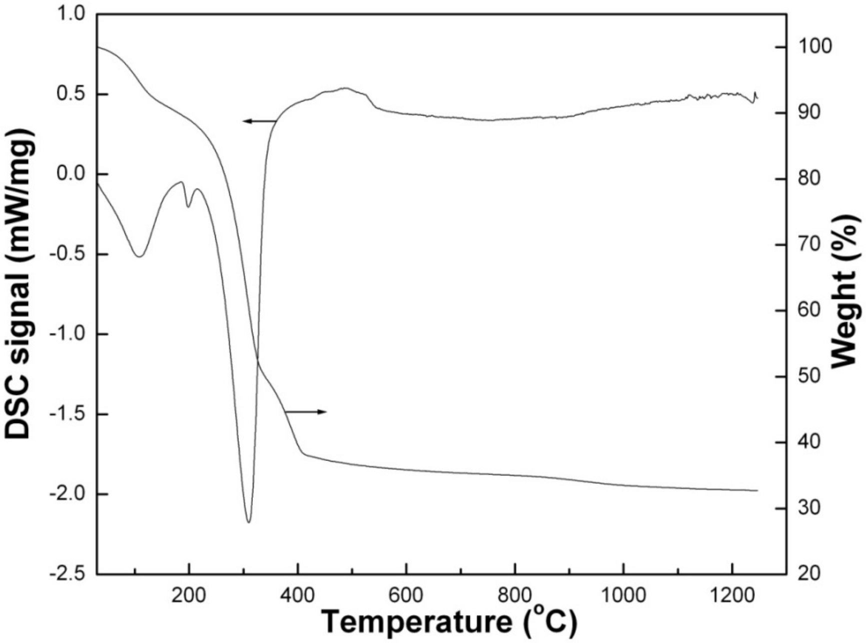

Fig.5.2. DSC/TG thermogram of as synthesized Al_2O_3-ZrO_2 dried gel (ROUTE 1)

The decomposition of $Al(OH)_3$ to Al_2O_3 is associated with 13.8% weight loss. The observed weight loss is 13.7% which matches well with the theoretical weight loss for the composite powder containing 40% wt% Al_2O_3 and 60% wt% ZrO_2. It may be mentioned here that the decomposition of $Al(OH)_3$ to Al_2O_3 is a two step process which takes place via an intermediate amorphous Al_2O_3 phase formation. The exothermic peak for amorphous to crystalline Al_2O_3 is masked by the strong endothermic peak at 300°C. This feature has been clearly indicated in a later section which discusses the effect of washing on the crystallization behavior

The second endothermic peak at 194°C is a sharp one without a corresponding weight loss in the TG curve. This peak, therefore, corresponds to reactions other than decomposition reactions. The decomposition of NH_4Cl is a two step process involving melting (220°C) and sublimation (338°C) [5.1]. Thus the endothermic peak at 194°C corresponds to the melting and sublimation of NH_4Cl.The later peak is associated with a weight loss of 48.4% which matches well with the theoretical weight loss (47.3%) for the sublimation of NH_4Cl.

The third stage of weight loss starts right after the second stage of weight loss and it continues till about 425°C. The weight loss recorded in this stage is 13.3%. It is anticipated that in this stage, $Zr(OH)_4$ decomposes according to the following reaction:

$$Zr(OH)_4 = ZrO_2 + 2H_2O \qquad (5.4)$$

The theoretical weight loss for this reaction is 22.7%. For equal volume fraction of Al_2O_3 - ZrO_2 composites, this comes out to be 13.58%, which matches well with the observed weight loss of 13.3%.

Immediately after the completion of weight loss, two broad and shallow exothermic peaks are observed between 490°C and 500°C. The exothermic peaks are because of crystallization of γ-Al_2O_3 and c-ZrO_2 respectively which are identified from their characteristic d-spacing.

5.1.3 FTIR Spectra of Dried Gel

The FTIR spectrum of the dried gel sample is shown in Fig. 5.3. The different peaks obtained in the wave number range 3500-400 cm^{-1} are assigned to different stretching and bending vibrations listed in Table 5.1. The broad peak in the wave number range 3500 –2800 cm^{-1} is assigned to O-H stretching vibration indicating the presence of molecular water and adsorbed water [5.2].

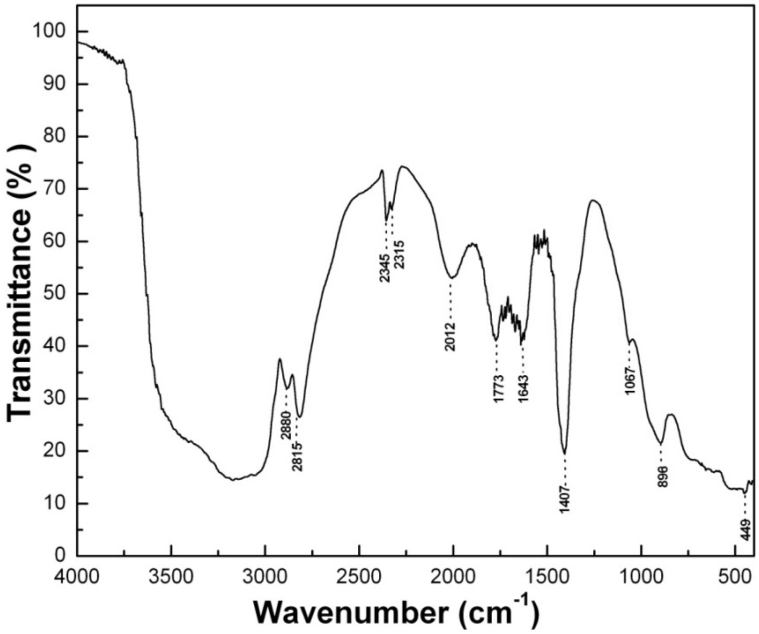

Fig.5.3. FTIR spectra of dried gel powder (ROUTE 1)

Table 5.1 FTIR spectra of dried gel (ROUTE 1)

Adsorption Peak (cm^{-1})	Nature of Peak	Identification
3500-3000	strong stretching	molecular water
2880	weak bending	H bonded OH
2813	sharp bending	N-H
2345	weak stretching	Cl^-
2012	weak stretching	-OH
1773	shoulder peak	N-H
1643	weak bending	Zr-OH
1407	strong stretching	N-H bending
1070	weak bending	Al-O (six coordinated)
896	broad peak	Al-O (four coordinated)
449	weak bending	Zr-O vibration

The shoulder peak around 2800 – 2750 cm^{-1} as well as at 1773,1400 cm^{-1} are due to N–H bending from NH_3 [5.3]. The absorption peaks at 2345 cm^{-1} correspond to the stretching of Cl^- ions and that of 2012 cm^{-1} is due to bending vibration of (-OH) groups of the hydroxides [5.4]. The peak appearing at 1643 cm^{-1} is due to the bending vibration of Zr-OH group. The six and four coordinated Al-O vibrations are shown at 1070 and 800 cm^{-1} respectively [5.5]. The broad bands in the range 550-500 cm^{-1} are due to Zr-O vibration [5.6]. The weak absorption peaks of Zr-O are due to the partial masking effect by the stronger intensity of Al-O vibration.

5.1.4 Phase Evolution in Calcined Gel

The XRD pattern of the gel calcined at different temperature is shown in Fig. 5.4. The powder calcined at 350°C show broad peaks of cubic ZrO_2 (JCPDS 81-1550), boehmite (JCPDS 83-1505) and bayerite (JCPDS 20-0011). The broadening indicates fine crystallites of ZrO_2. The average crystallite size of the powder calcined at 450°C is 4.71 nm, which increases at higher calcination temperature (Table 5.2). At higher calcination temperature the ZrO_2 peaks become sharp and strong in intensity due to growth of crystallites. Till 500°C, only *c*-ZrO_2 peaks could be detected and identified. At 850°C, *t*-ZrO_2 also starts to appear. The presence of *t*-ZrO_2 was identified on the basis of $(002)_t$ and $(200)_t$ split peaks. At still higher calcination temperature (950°C), a mixture of *t* and *m*-ZrO_2 and γ-Al_2O_3 could be detected. The amount of retained *t*-ZrO_2 at this temperature is 79%. Shi et al. [5.7] and Hong et al. [5.8] have reported that the lattice distortion of ZrO_2 by Al_2O_3 particle restrict the crystallite growth of ZrO_2 and can help to retain metastable ZrO_2 phases. However, crystalline phase of transition Al_2O_3 could not be detected at lower temperatures and at 750°C γ-Al_2O_3 was observed which was retained till 950°C.

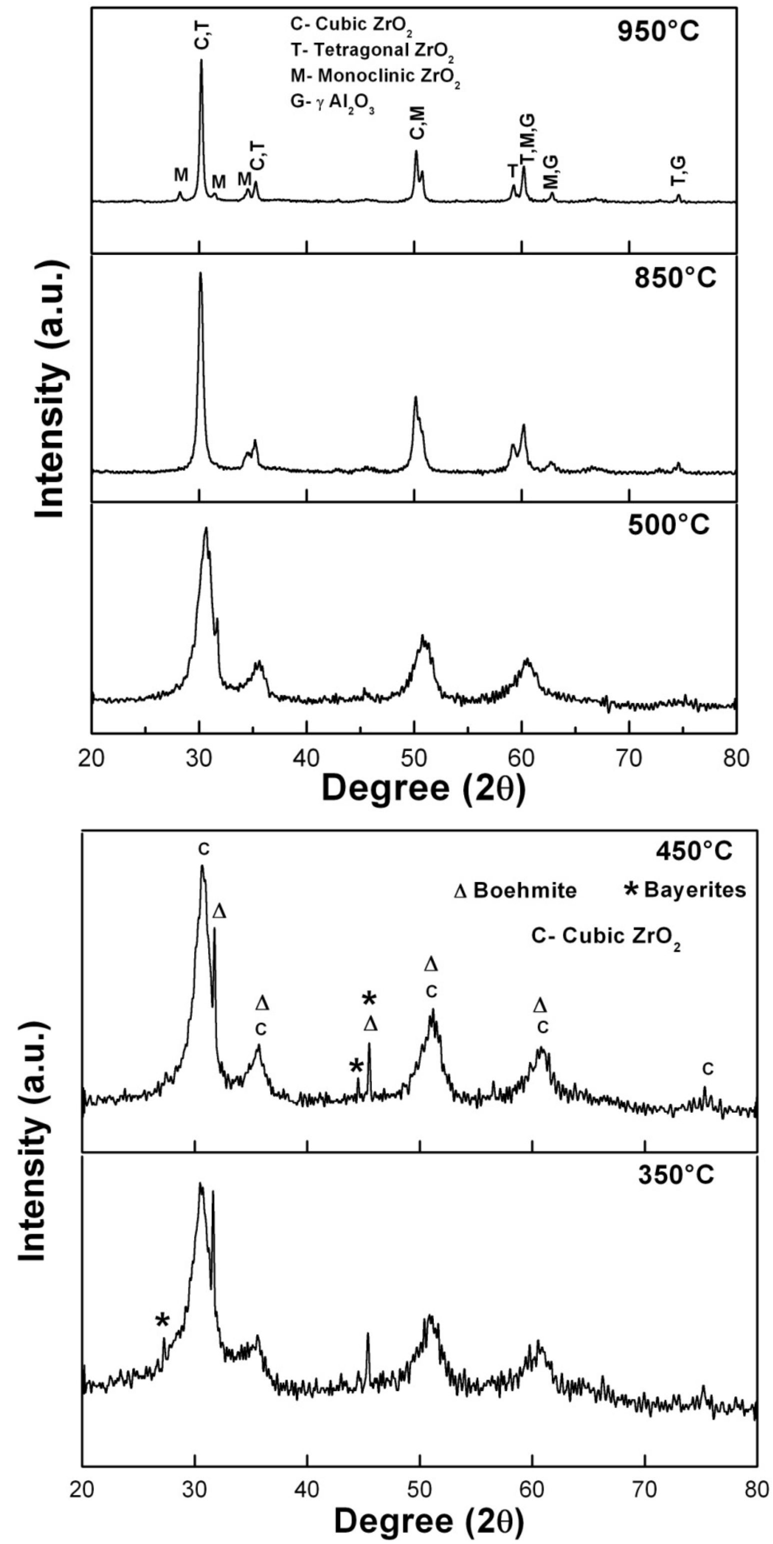

Fig.5.4. Phase evolution of Al_2O_3-ZrO_2 gel as a function of calcination temperature (ROUTE 1)

Table 5.2 Crystallite size of ZrO_2 as a function of calcination temperature in the Al_2O_3-ZrO_2 composite powder (ROUTE 1)

Temperature (°C)	Crystallite Size of ZrO_2 (nm)	Phase
350	3.62	*c*-ZrO_2 ,boehmite, bayrite
450	4.71	*c*-ZrO_2, boehmite, bayrite
500	5.1	*c*-ZrO_2 boehmite, bayrite
850	15.29	*c,t,m*-ZrO_2(tr), γ-Al_2O_3
950	22.99	*c,t,m*-ZrO_2, γ-Al_2O_3

5.1.5 Particle Size and TEM Analysis of Calcined Gel

The particle size distribution of calcined gel (Fig.5.5) is broad. The fine fraction (<10 μm) is 16 vol% and the coarse fractions (>80 μm) is 86 vol%. The mean particle size (d_{50}) is 35.47 μm. The characteristic features of calcined gel are given in Table 5.3. The BET surface area of the calcined gel is 49 m^2gm^{-1} and calculated particle size (d_{BET}) is 51 nm.

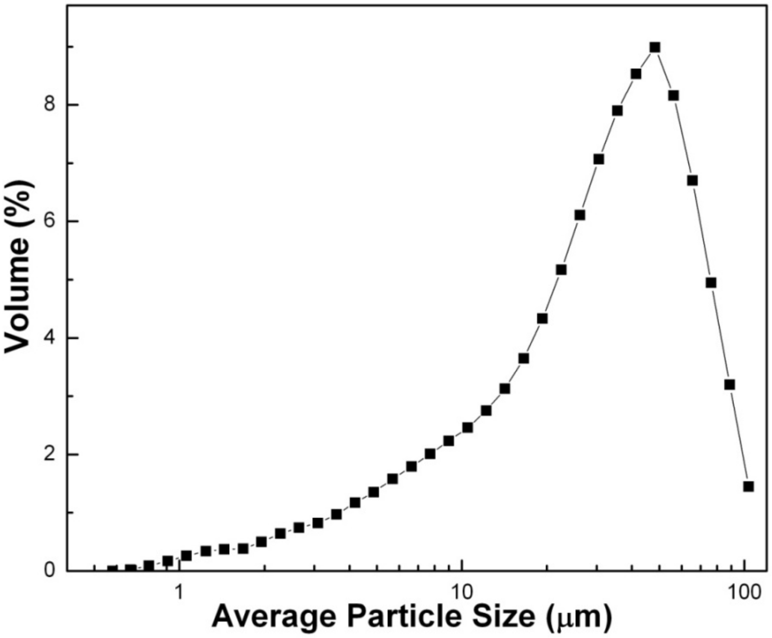

Fig.5.5. Particle size distribution of Al_2O_3-ZrO_2 calcined (850°C) powder (ROUTE 1)

Table 5.3 Properties of (850^{o}C) calcined powder (ROUTE 1)

D_{50} (μm)	D_{BET} (nm)	D_{TEM} (nm)	P_j (MPa)	S (m^2/gm)	AF
35.47	51	25	134	49	1418

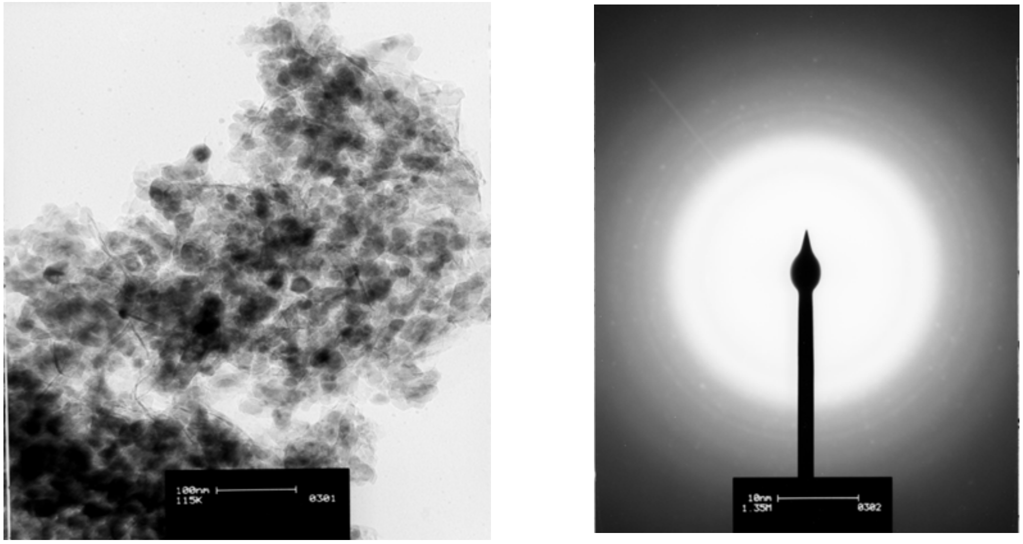

Fig.5.6. TEM photograph of calcined (850°C) Al_2O_3-ZrO_2 powder (ROUTE 1)

The TEM micrograph of calcined powder (Fig. 5.6) show agglomerated powder containing primary particles. The electron diffraction pattern show diffused ring pattern indicating very fine crystallites. X-ray diffraction pattern shows that the fine crystallites are boehmite [JCPDS 83-1505]. The strong inter-particle bonding resulting from the inter-particle solvent removal during drying; this brings the particles closer because of capillary action resulting in particle cluster formation. Subsequently, during calcination, these particle clusters form strong bridges among themselves thereby forming hard agglomerates. It is also possible that the cluster of primary particles can have weak inter-particle bonding thereby forming soft agglomerates. The TEM microstructure of the calcined gel shows high degree of agglomeration. The degree of agglomeration is expressed by Agglomeration Factor (AF), which is the ratio of mean agglomerate or particle size to primary particle size. A higher value of AF is an indication of greater degree of agglomeration.

5.1.6 Compaction Behaviour of Calcined Gel

Figure 5.7 shows the semi logarithmic plot of compaction pressure as a function of density of the green compacts for as prepared calcined gel. The graph of green density vs log (compaction pressure) provides important information about the powder compaction behaviour. Usually, compaction of ceramic powders takes place in two stages:

Stage-I	Granule flow and rearrangement
Stage-II	Granule deformation combined with granule densification.

The crushing strength (P_j) of particles is the intersection of the two linear segments and the P_j value varies with size, shape and extent of particle breakage from brittle fracture.

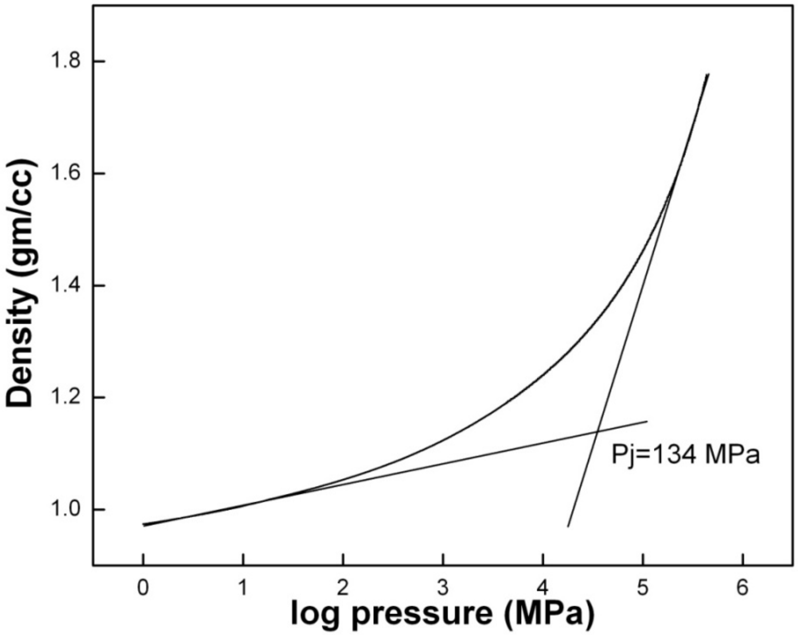

Fig.5.7. Compaction behaviour of calcined (850°C) Al_2O_3-ZrO_2 powder (ROUTE 1)

Stage-I take place at lower pressure, where a small amount of sliding and granule rearrangement takes place. Stage-II occurs above P_j and begins with granule deformation, which subsequently shifts to granule densification process. The dependence of agglomerate break point P_j on the granule parameter during stage –II compaction can be described by the following equation [5.9].

$$\rho_{compact} = \rho_{fill} + M \log \frac{P_a}{P_j} \tag{5. 5}$$

where, $\rho_{compact}$ is the compact density at an applied pressure P_a, ρ_{fill} is the filled density and '*M*' is the compaction constant that depends on the deformability and densification characteristics of the granules.

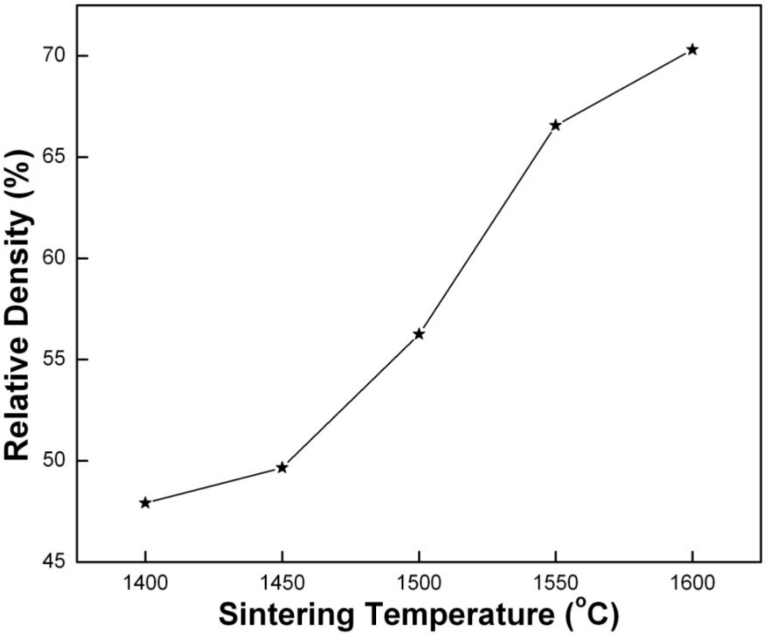

Fig.5.8. Relative density as a function of sintering temperature for sintered Al_2O_3-ZrO_2 composites (ROUTE 1)

The critical pressure (P_j) or the agglomerate break point denotes the strength of the agglomerate. The lower is the agglomerate strength; the softer will be the agglomerate which will easily break under compaction load leading to better compaction and high green density. The as prepared calcined powder shows higher P_j value (134 MPa). It is usually observed that powder containing high density granules produce a high compact density with a lower value of m (up to 5). Soft or low density granules, on the other hand have '*M*' in the range 7-10 [5.9]. For the gel prepared powder '*M*' is 2.2 which indicate that the powder has high-density granules.

5.1.7 Densification Behaviour of Sintered Pellets

The relative density of the sintered samples as a function of sintering temperature is shown is Fig. 5.8. The relative densities were calculated using rule of mixture and the theoretical densities of monoclinic ZrO_2 (5.89 gm/cm^3) and Al_2O_3 (3.98 gm/cm^3). It is seen that the density increases with sintering temperature and exhibit '*S'* type behaviour. Although a large linear shrinkage (15% - 19%) was observed during the sintering process, the sintered samples had poor sintered density. It is presumed that the presence of hard agglomerates and flaws restrict pore removal during sintering which reduces the sintered density [5.10].

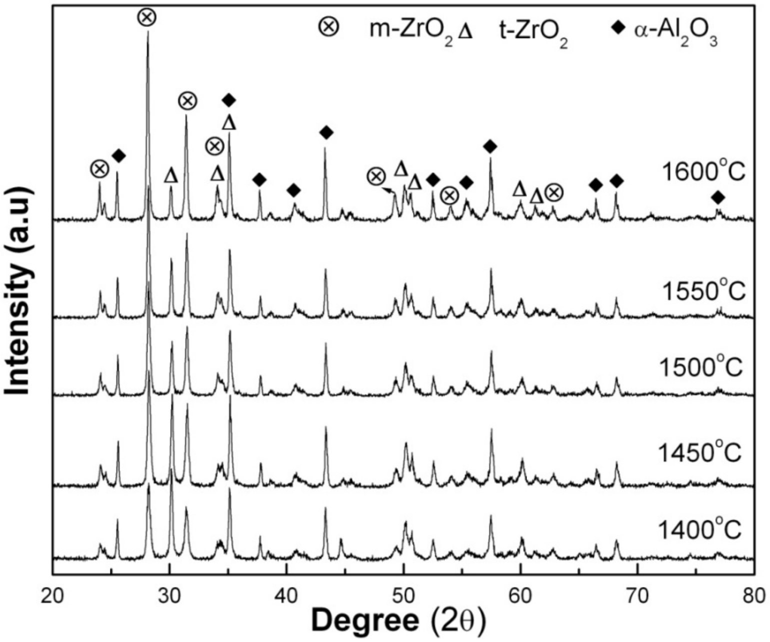

Fig.5.9. XRD pattern of Al_2O_3-ZrO_2 composites sintered at different temperature (ROUTE 1)

5.1.8 Phases and Microstructure in the Sintered Sample

The XRD pattern of the samples sintered at different temperature is shown in Fig. 5.9. The volume fraction of *m*-ZrO_2 and *t*-ZrO_2 has been calculated using Schmid's formula [5.11] and is shown in Fig. 5.10. X-ray diffraction pattern of sintered pellets show monoclinic ZrO_2 (d= 3.15 A^o, JCPDS 83-0944) and α-Al_2O_3 (d= 2.09A^o, JCPDS 82-1467) as the major phase in the sintered sample along with small amount of *t*-ZrO_2 phase (d= 2.96 A^o, JCPDS 81-1544). The fraction of retained *t*-ZrO_2 decreases on increasing the sintering temperature probably due to the combined effect of low matrix constraint provided by the porous compacts as well as due to an increase in grain size.

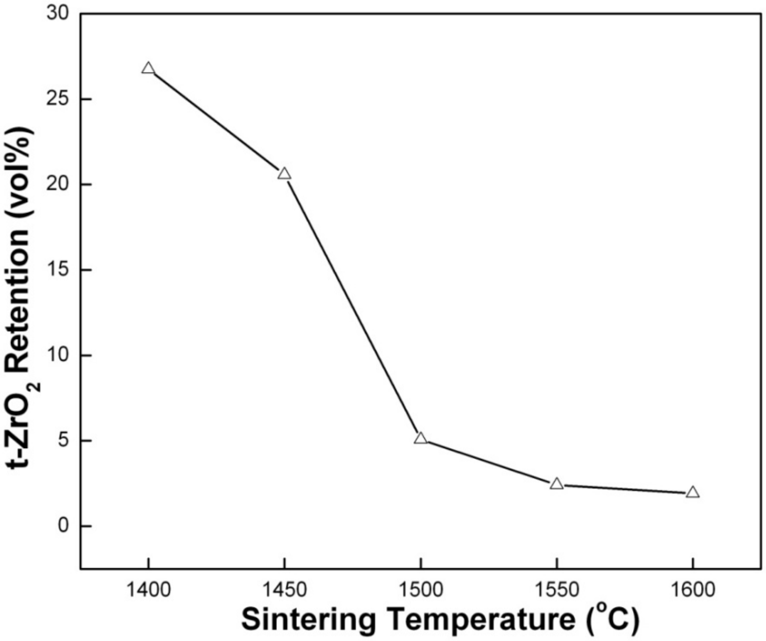

Fig.5.10. Tetragonal ZrO_2 retention as a function of sintering temperature (ROUTE 1)

Figure 5.11 show the sintered microstructure of Al_2O_3-ZrO_2 composite. The dark grains are Al_2O_3 and bright grains are ZrO_2. The microstructure is porous and shows both intergranular and intragranular ZrO_2. The grain size distribution of both Al_2O_3 and ZrO_2 has wide variation. The average grain size for ZrO_2 are 1.43 ± 0.45 *μm* and that of Al_2O_3 are about 1.67 ± 0.57 *μm*.

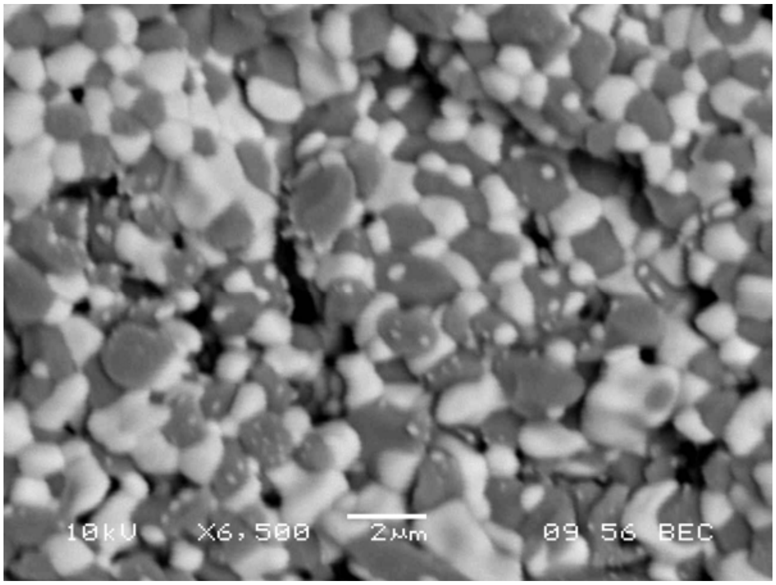

Fig.5.11. SEM micrograph of Al_2O_3-ZrO_2 composites sintered at 1600°C (ROUTE 1)

The present section on the processing of Al_2O_3-ZrO_2 composites by gelation could be concluded with the following findings. Although, the prepared Al_2O_3-ZrO_2 powder had fine crystallites, it also had high agglomeration strength. The maximum sintered density of the composite after sintering at 1600^{o}C was 70% with low fraction of retained *t*-ZrO_2 (9.3%). The sintered sample had porous microstructure with both inter and intragranular ZrO_2 in Al_2O_3 matrix. The porous microstructure probably resulted from the sintering of agglomerated powder. Therefore, further processing optimization are needed to improve the sintered density as well as *t*-phase retention. It is proposed that the same may be achieved either by modifying the powder processing route or by adopting post powder preparation processing steps.

5.2 Preparation of Al_2O_3-ZrO_2 Composite by Precipitation Method Using Chloride Precursors (ROUTE 2)

In the previous section, it was observed that the composite powder prepared by gelation method did not densify to high density and it was thought that the gelation method might be responsible for poor sintered density. The logic behind this assumption is the fact that in the gelation process, upon the addition of NH_4OH, partial precipitation of the $AlCl_3$ and $ZrOCl_2$ to the respective hydroxide takes place. The system pH at this stage is about 6.5. Subsequently, the hydroxides forms a network and results in a gel which entraps the unreacted $AlCl_3$ and $ZrOCl_2$ as well as the solvent. The presence of residual chlorides helps in lowering the crystallization temperature of Al and Zr hydroxides. Due to low temperature crystallization, the crystal growth continues even at higher temperature and therefore, at the sintering temperature the crystallite size becomes large which most likely has affected *t*-phase retention and density. Secondly, due to the large volume of the entrapped solvent (water), hard agglomerate formation is favoured and this also has affected densification. Washing of the gel to remove the excess ions and the solvent cannot be adopted here because it will also remove the water soluble unreacted salts which may affect the stoichiometry. Thus, a different powder processing route, viz, precipitation from the salt is being adopted as a process optimization step. In the precipitation process, the pH is maintained between 8.7 and 9.1 and the system is thoroughly stirred during the precipitation process so that complete reaction of $AlCl_3$ and $ZrOCl_2$ with NH_4OH takes place. This precipitate if required can be washed for the removal of unwanted anions. This section will therefore, discuss the properties of Al_2O_3-ZrO_2 composite powder and compact prepared from the precipitated powder.

The method of the Al_2O_3-ZrO_2 composite powder preparation by precipitation route has already been detailed in section 4.2.2. In the following sections, the thermal decomposition, crystallization, phase evolution and densification behaviour of those powder and that of the sintered compacts will be discussed.

5.2.1 Thermal Analysis of Dried Precipitates

Figure 5.12 shows the DSC/TG plot of the precipitated Al_2O_3 -ZrO_2 uncalcined powder. The graph is distinctly different from that of dried gel. It has two endothermic peaks; the first one is broad and occurs in the temperature range 30°C -180°C followed by a sharp endothermic peak at 290°C. The TG curve exhibit a total weight loss of 52% which takes place in three stages. In the first stage (RT- 180^0C), the weight loss is 14%. The second stage of weight loss (24%) is observed between 180^0C - 320°C and the third and final stage of weight loss (13%) is observed between 320°C - 350^0C. The first endothermic peak doublet and the associated weight loss correspond to the dehydroxylation of hydrated Al_2O_3 (pseudo boehmite). The decomposition of pseudo boehmite takes place in two stages. In the first stage, pseudo boehmite loses its 15% excess water and transforms to bayerite which subsequently decomposes to amorphous Al_2O_3. The crystallization of amorphous to transition Al_2O_3 is masked by the strong endothermic peak of NH_4Cl decomposition.

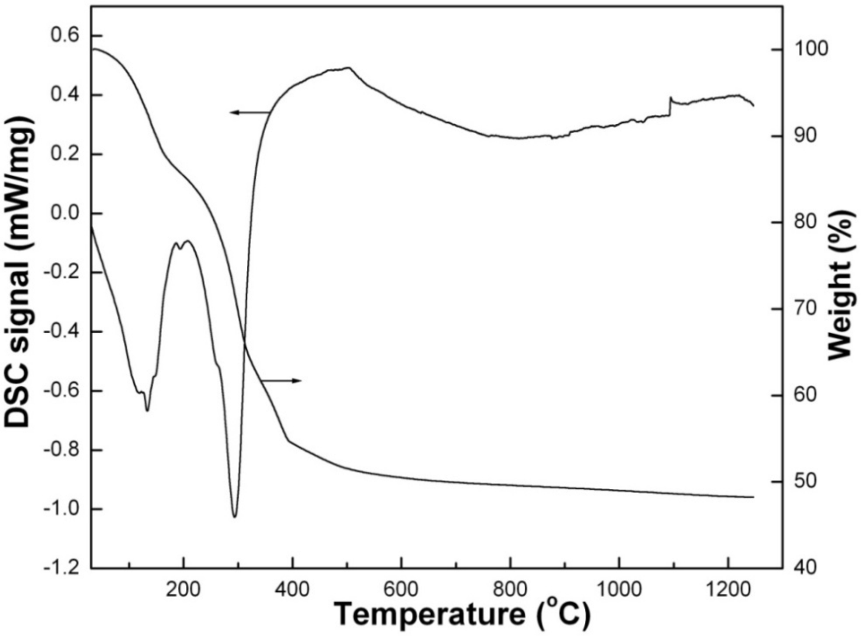

Fig.5.12. DSC/TG of as synthesized dried Al_2O_3-ZrO_2 precipitates (ROUTE 2)

The second endothermic peak and the associated weight loss is due to the decomposition of NH_4Cl (Eqns. 5.1 and 5.3) and the third stage weight loss relate to the dehydroxylation of $Zr(OH)_4$ (Eqn. 5.4). The observed weight loss for the dehydroxylation of $Al(OH)_3$ and $Zr(OH)_4$ matches with that of theoretical value. Since the precipitation was carried out at higher pH (8.7-9.1), it ensured complete precipitation of both $AlCl_3$ and

$ZrOCl_2$ to $Al(OH)_3$ and $Zr(OH)_4$ respectively. In this case, the dehydroxylation of $Zr(OH)_4$ to ZrO_2 is a single step process (Eqn. 5.4). Due to the partial removal of NH_4Cl during solvent extraction from the precipitates, the observed weight loss for NH_4Cl is less (24%) as against 48% for the gel.

5.2.2 FTIR Spectra of Dried Precipitates

The FTIR spectrum of the amorphous precipitates is presented in Fig. 5.13. The different absorption peaks and the possible vibration frequencies have been listed in Table 5.4.

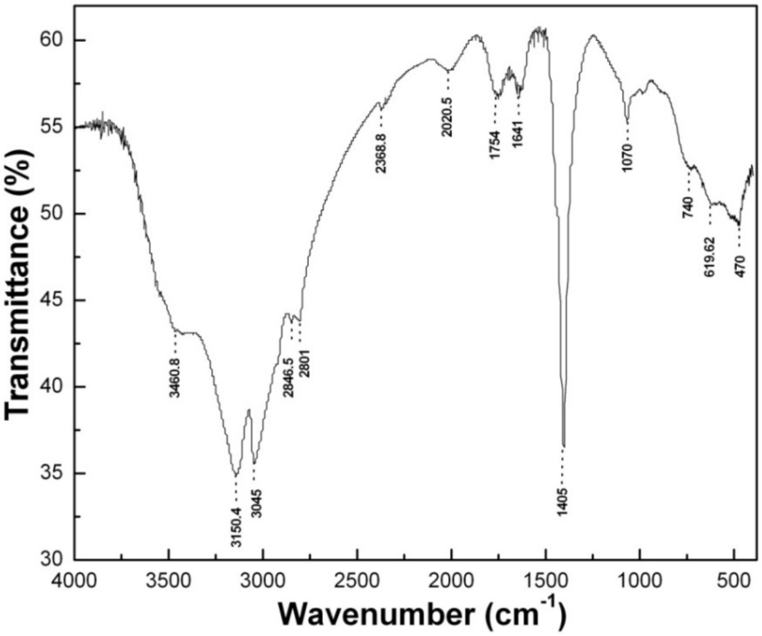

Fig.5.13. FTIR spectra of dried Al_2O_3-ZrO_2 precipitates (ROUTE 2)

A comparison of this spectrum with that of the gel (Fig. 5.3) shows that due to a lower fraction of residual water and anions in the precipitates the absorption peaks are well resolved. The absorption peaks at 3150, 3045 and 1070 cm^{-1} are clearly distinguishable (Fig. 5.13). It is also noticed that the absorption peaks of Zr-O is weak due to the partial masking effect from the stronger intensity peaks of Al-O and N-H stretching. The shoulder peaks at 620 and 470 cm^{-1} are due to cubic ZrO_2 [5.6].

Table 5.4 FTIR spectra of dried precipitates (ROUTE 2)

Adsorption Peak (cm^{-1})	Nature of Peak	Identification
3460	stretching vibration	Molecular water
3150,3045	strong Bending	H bonded OH
2800-2850	shoulder peak	N-H
2370	weak stretching	Cl^-
1750	shoulder peak	N-H bending
1641	weak bending	Zr-OH
1405	strong stretching	N-H bending
1070	sharp bending	Al-O
470,620	weak bending	Zr-O vibration

5.2.3 Phase Evolution of Calcined powder

The XRD patterns of Al_2O_3-ZrO_2 calcined (350 to 950^oC) precipitates are presented in Fig 5.14. The powder calcined at 350^oC show broad peaks of cubic ZrO_2 (crystallite size 4.4 nm). The average crystallite size increases with increasing temperature due to the nucleation and growth of crystals. Tetragonal ZrO_2 appears at 850°C but monoclinic ZrO_2 could not be detected till 950°C. γ- Al_2O_3 could be detected from 850^0C onwards.

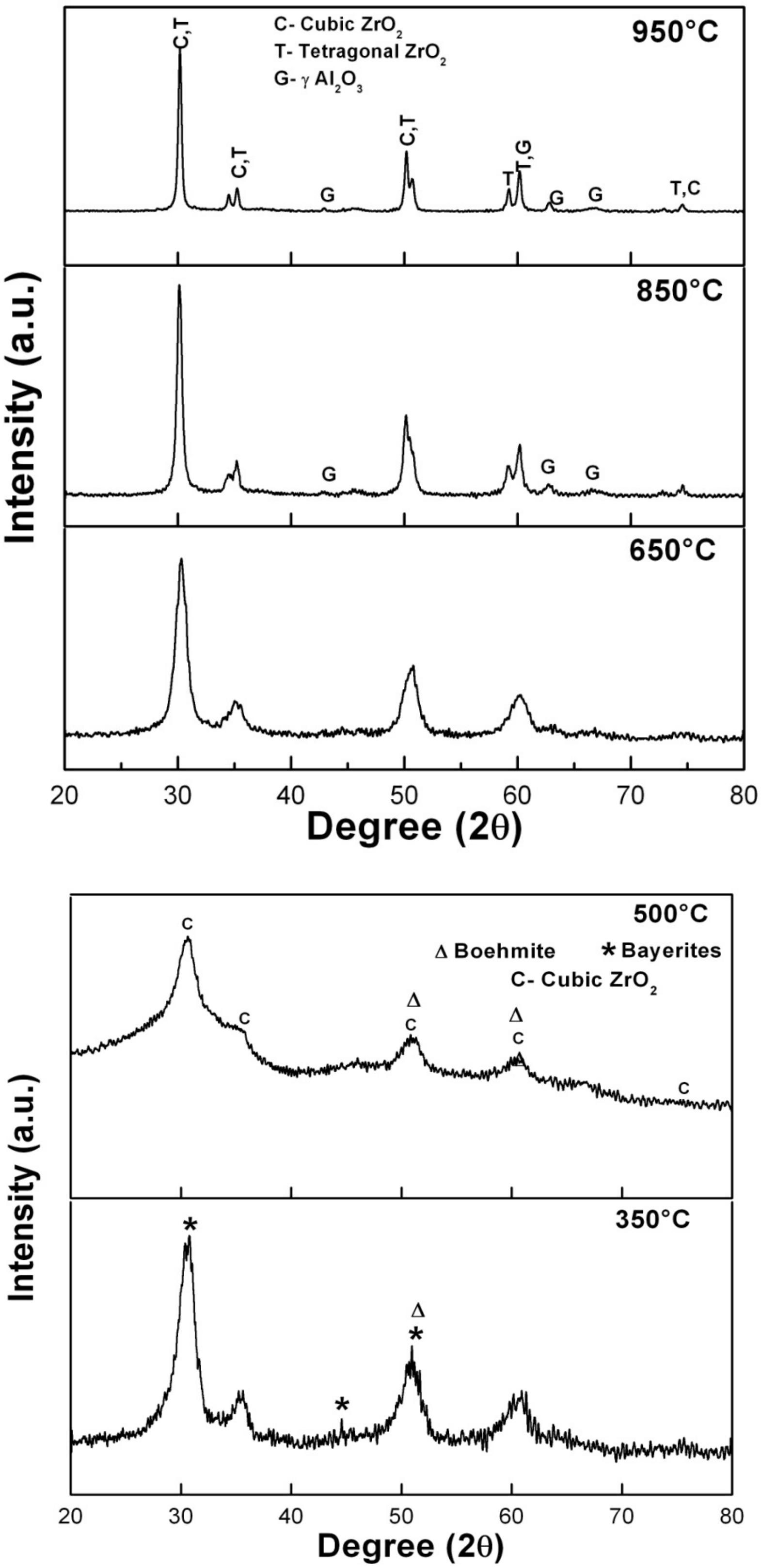

Fig.5.14. XRD pattern of Al$_2$O$_3$-ZrO$_2$ precipitates at different calcination temperature (ROUTE 2)

5.2.4 Particle Size and Surface Area of Calcined Precipitates

The particle size distribution of calcined precipitates is shown in Fig. 5.15. The agglomerates have a wide size distribution ranging from 1-100 μm. The distribution shows that 40% of the agglomerates are in the size range of 30-60 μm with very few (~ 20%) on the lower size (<10 μm) range. The specific surface area of the calcined powder is 71 m^2 gm^{-1} and the calculated particle size (D_{BET}) is 17.42 nm.

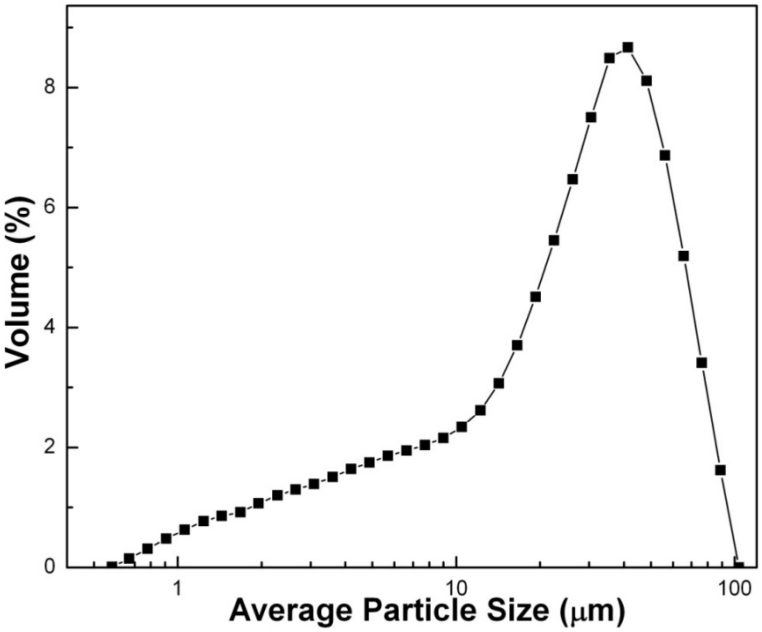

Fig.5.15. Particle size distribution of 850°C calcined precipitates (ROUTE 2)

5.2.5 TEM Analysis

Figure 5.16 (a) shows the bright field TEM image of calcined precipitates. The selected area diffraction pattern of the powder (Fig 5.16 (b)) shows ring pattern indicating polycrystalline nature of the calcined precipitates. The micrograph shows that although the primary particles are spherical, they are agglomerated. The dark particles are ZrO_2 and the lighter ones are Al_2O_3. While the crystallite size calculated from X-ray line broadening is 12.78 nm, TEM micrograph indicate that the average particles size is 22.5 nm. A larger particle size in TEM is due to the agglomeration of crystallites or primary particles caused due to the high surface energy of the fine crystallites.

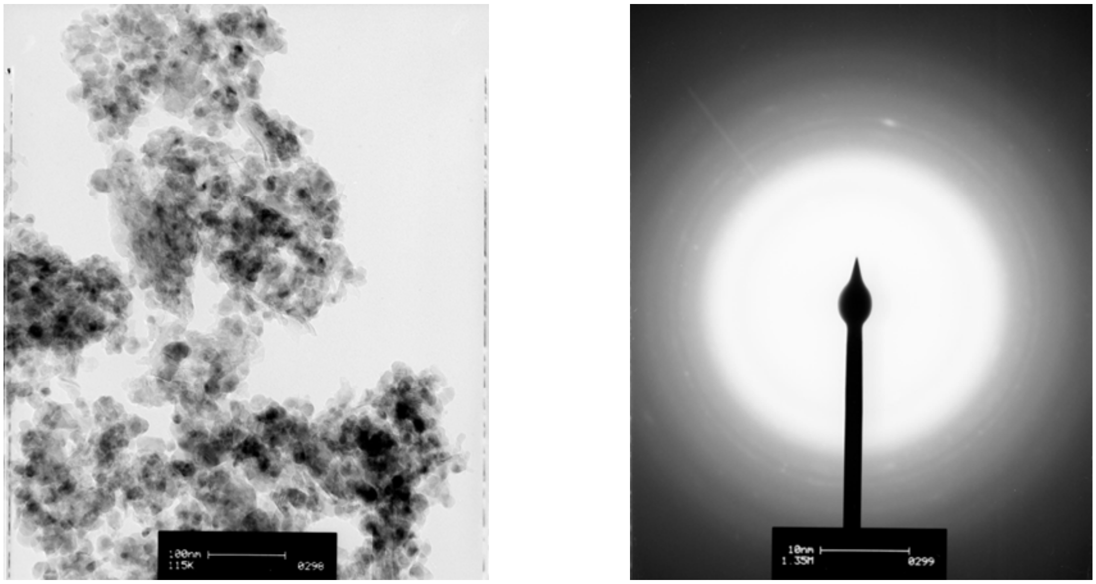

Fig.5.16. (a) TEM micrograph and (b) diffraction pattern of Al_2O_3-ZrO_2 powder calcined at 850°C (ROUTE 2)

Table 5.5 Properties of calcined (850°C) powder (ROUTE 2)

D_{50} (µm)	D_{BET} (nm)	D_{TEM} (nm)	P_j (MPa)	S ($m^2\ gm^{-1}$)	AF
30.4	17.42	22.5	126	71	1216

5.2.6 Compaction Behaviour of Calcined Powder

Figure 5.17 shows the plot of log compaction pressure vs. green density of calcined precipitate compacts. The P_j value is 126 MPa which is lower than that of gel (134 MPa). The compaction behaviour graph shows that higher initial green density of the compacts can be achieved by pressing in second segment of compaction (>126 MPa). The elimination of intergranular pores during the second stage of compaction increases the density.

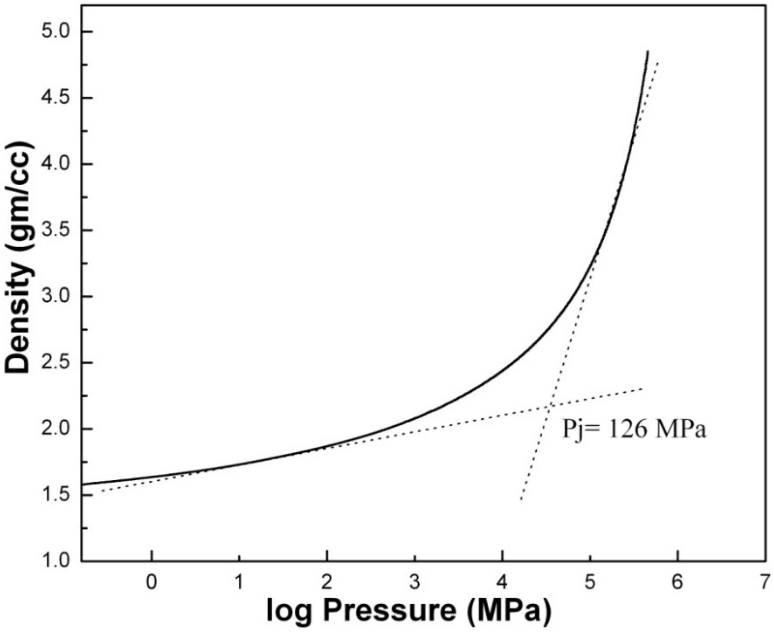

Fig.5.17. Compaction curve of precipitated Al_2O_3-ZrO_2 composite (ROUTE 2)

A wider distribution of agglomerate size is expected to increase the green density owing to better particle packing efficiency. This powder also has very high AF (1216) and 'M' (2.6) which signifies that the powder contains hard agglomerates.

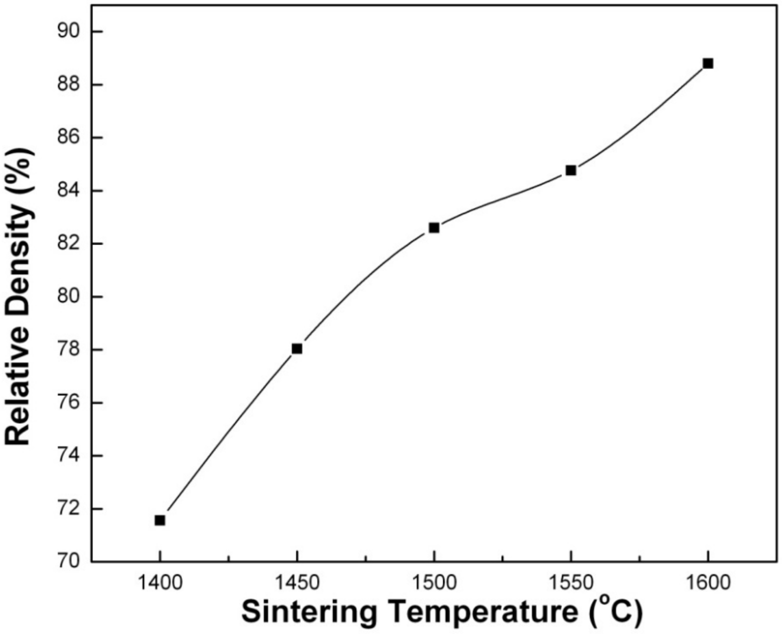

Fig.5.18. Effect of sintering temperature on relative density of Al_2O_3- ZrO_2 composite (ROUTE 2)

5.2.7 Densification Behaviour and Phase Retention of Sintered Sample

The relative density increases with sintering temperature as shown in Fig. 5.18. At 1600°C, the linear shrinkage of the sample is 25% and the relative density is 88%.

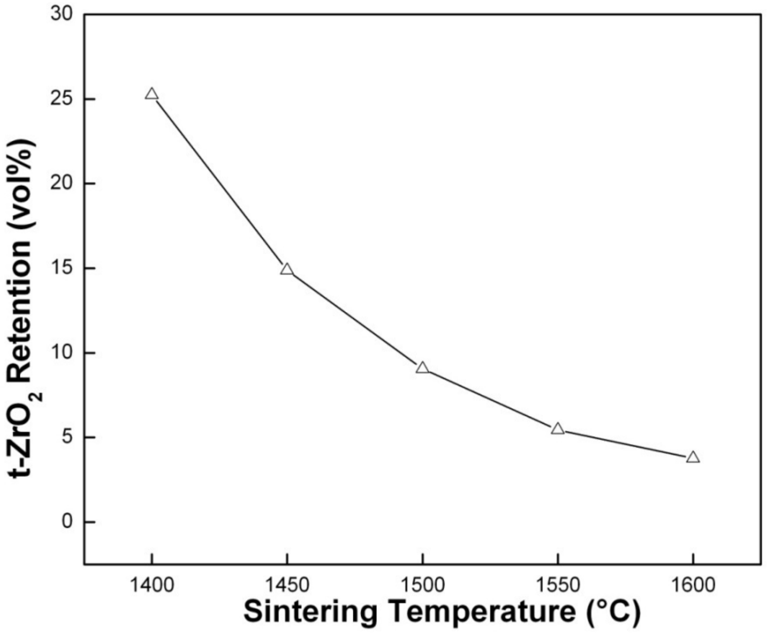

Fig.5.19. Tetragonal ZrO_2 retention as a function of sintering temperature (ROUTE 2)

5.2.8 Microstructure of Sintered Sample

The microstructure of sintered pellet in Back Scattered Electron (BSE) mode is shown in Fig. 5.20. The bright grains are ZrO_2 and the dark grains are Al_2O_3. A near uniform distribution of ZrO_2 and Al_2O_3 grains is observed throughout the matrix. The average grain size of Al_2O_3 and ZrO_2 is 1.7 ± 0.74 μm, and 1.9 ± 0.61 μm respectively. The ZrO_2 mostly appears at the grain boundaries of Al_2O_3. However, some submicron intragranular ZrO_2 grains are also found within the Al_2O_3 matrix and very few intragranular Al_2O_3 grains are also found in ZrO_2. Micropores are present at the triple junctions of the ZrO_2 grains. The presence of pores tends to increase the diffusion distance between particles thereby reducing the driving force for pore shrinkage. SEM observation also revealed that many of these pores could not be removed even during the later stage of sintering.

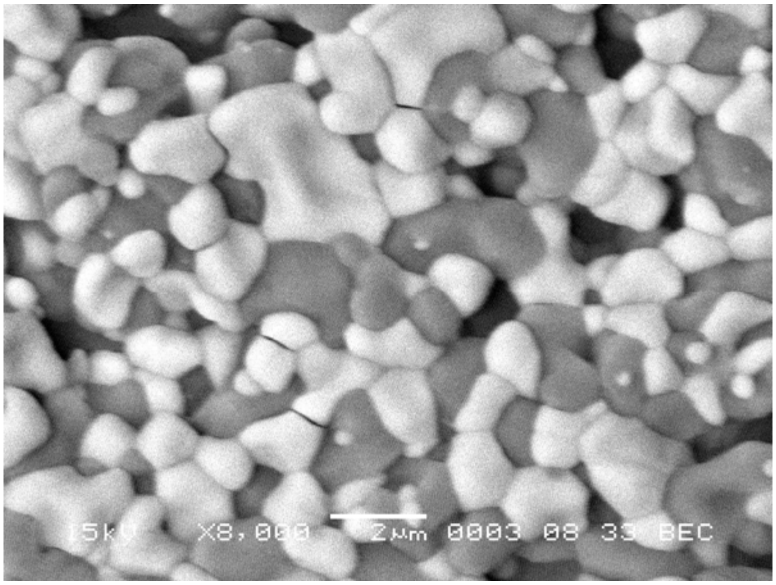

Fig.5.20. SEM micrograph of sintered sample (ROUTE 2)

This section discussed the powder processing and characterization of Al_2O_3- ZrO_2 composites prepared by precipitation route using $AlCl_3$ and $ZrOCl_2$. DSC/TG of the as precipitated powder show single stage decomposition of $Zr(OH)_4$. The calcined powder shows a wide size distribution of agglomerate and low agglomeration strength (126 MPa). It was expected that a finer initial particles and removal of entrapped anions may improve the densification of composites. However, the maximum sintered density was only 88% after sintering at 1600^oC with only 4% *t*-ZrO_2 retention. The sintered samples have porous microstructure with both intragranular and intergnalular ZrO_2 dispersed in Al_2O_3 matrix and vice versa. The relative density of the composite although is higher than gelation route but is still low enough for mechanical property evaluation of the composite. It was also noticed that the composites undergoes a weight loss of 7.7 % during the sintering stage which is more as compared to binder content. This may be due to the removal of chlorides at higher temperature. Similar observations have been made by Scott and Reed [5.12] while working on the effect of laundering on the densification of ZrO_2. Sarkar also noted that OH- remains attached to Al_2O_3 till 1000^oC [5.22]. Thus the additional weight loss during sintering of the composites can be linked to these two factors and therefore, it is necessary to remove chloride as well as hydroxyls after the complete precipitation and before calcination and sintering.

Thus the precipitated powders were subjected to hot water and alcohol washing to remove the chloride ions as well as for minimizing the hard agglomerates formation by changing the nature of surface bonding.

5.3 Effect of Hot Water and Alcohol Washing on Al_2O_3-ZrO_2 Composite Prepared by Precipitation Using Chloride Precursors (ROUTE 3)

As discussed in the previous section, Al_2O_3 - ZrO_2 composite has been prepared by precipitation route at pH 8.7-9.1 using $AlCl_3$ and $ZrOCl_2.8H_2O$ as the precursor. The precipitate was washed with hot water to remove the excess NH_4OH and NH_4Cl followed by propanol washing for removing the surface hydroxyl groups from $Al(OH)_3$ and $Zr(OH)_4$ (which are likely to produce hard agglomerate after drying). The effect of washing on the properties of Al_2O_3-ZrO_2 composite is discussed in the following sections.

5.3.1 Thermal Analysis of Dried Washed Precipitates

The DSC/TG plot of the as dried washed precipitates is shown in Fig. 5.21. The DSC plot shows two broad exothermic peaks at 105^oC and 209^oC (this is indicated by a slope change and a peak in the derivative DSC curve), a combination of exothermic, endothermic and exothermic peak between 280 and 305^oC and another broad exothermic peak at 800^oC. The first endothermic peak refers to pseudo boehmite to bayerite transformation. This bayerite further transforms to boehmite with a weight loss of 6% at 209^oC. Subsequently, bayerite crystallizes to γ-Al_2O_3 at 280^oC. The next endothermic peak is for $Zr(OH)_4$ decomposition followed by another exothermic peak due to the crystallization of cubic ZrO_2.The TG plot shows a total weight loss of 28.6% which takes place in two stages. X-ray diffraction pattern of 'as dried' precipitate shows that pseudo-boehmite is present. The pseudo-boehmite has a disordered structure and it contains >15% water in the lattice. On heating, dehydroxylation of pseudo-boehmite takes place and the structure changes to bayerite. On further heating, bayerite changes to Al_2O_3 through the intermediate step of boehmite [5.13, 5.14]. Assuming that there are no impurities (i.e.NH_4Cl or NH_4OH, which have been mostly removed during washing), the weight loss in TG is due to two processes, viz. decomposition of $Al(OH)_3$ (single stage decomposition) and decomposition of $Zr(OH)_4$. For equal volume fraction of Al_2O_3 and ZrO_2, $Al(OH)_3$ dehydroxylation weight loss should be 13.9% (Eqn. 5.2).

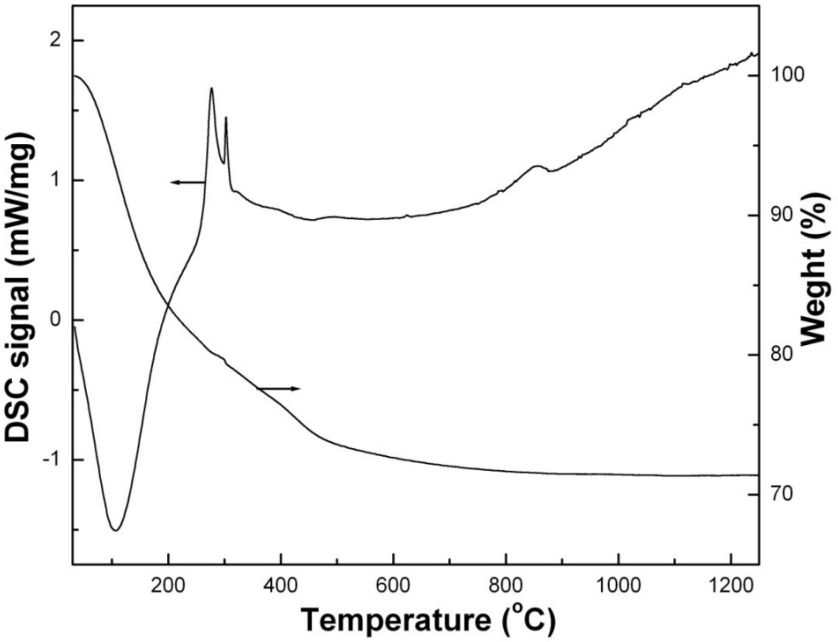

Fig.5.21. DSC/TG of dried washed precipitates (ROUTE 3)

The observed weight loss of 14% matches well with theoretical value and thus the first stage weight loss up to 300°C corresponds to the decomposition of $Al(OH)_3$ and its crystallization to Al_2O_3.The DSC curve also shows an exothermic peak at the end of the first stage weight loss. The second stage weight loss is 14.6%. For the $Zr(OH)_4$ decomposition reaction (Eqn. 5.4), the calculated weight loss is 13.82% for powder having equal volume fraction of Al_2O_3 and ZrO_2.The observed weight loss 14.6% corresponds well with the theoretical value. This weight loss is also associated with an exothermic peak at 400°C.Thus the exothermic peak at 400°C and the weight loss of 14.6% between 300 and 400°C is due to the decomposition of $Zr(OH)_4$ and the crystallization of ZrO_2. XRD confirms that cubic ZrO_2 is formed at around that temperature. The exothermic peak at 825°C is due to the transformation of cubic to tetragonal ZrO_2.The phase transition of amorphous to cubic and tetragonal follows the reported transformation sequence [5.15].

5.3.2 FTIR Analysis

The nature of the surface radicals of the washed precipitates (uncalcined and calcined) was observed using FTIR spectroscopy (Fig. 5.22). The crystallization behaviour and phase evolution during calcination is dependent on the nature of bonding in the Zr and Al hydroxides in the raw powder.

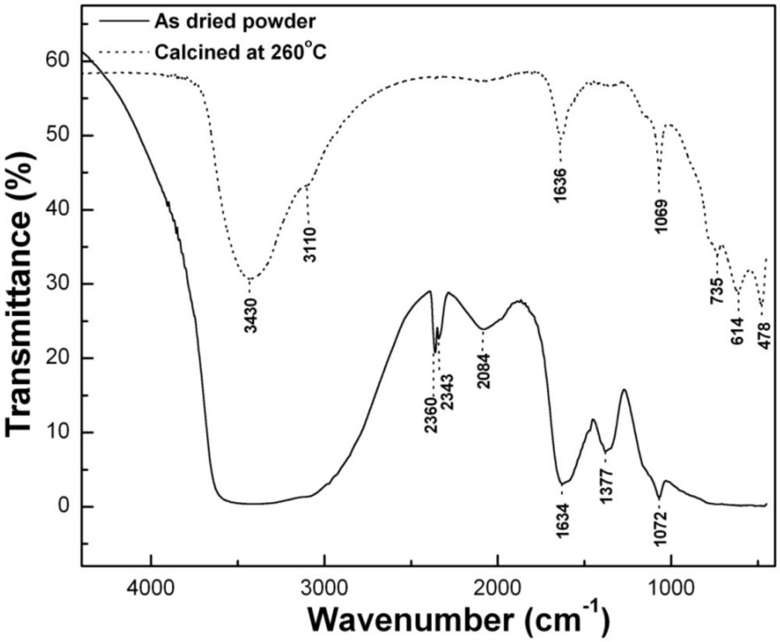

Fig.5.22. IR spectra of dried and calcined washed precipitates (ROUTE 3)

The stretching positions of raw powder as well as calcined powder are quite similar to those reported in earlier sections (Sections 5.1.3 and 5.2.2). The relative intensity of all possible peaks is higher for calcined powder. A comparative study of the different peak positions for both the powder is given in Table 5.6.The broad band at 3200-3600 cm^{-1} in the raw powder is due to asymmetric and symmetric stretching vibration of (OH)$^{-1}$ group, and this broad peak became narrow on calcination. The sharp peaks at 2361 and 2343 cm^{-1} are due to coupled effect of stretching and bending vibration of (OH)$^{-1}$ group. The calcined powder does not have any H-bonded (OH)$^{-1}$ group. The bending at 3430 and 3110 cm^{-1} are the non-hydrogen bonded (OH)$^{-1}$ group which confirms the presence of Zr(OH)$_4$ in raw powder. The peaks at 1070 and 735 cm^{-1} correspond to Al-OH and Al-O bonds. The stretching vibration at 605 and 472 cm^{-1} in calcined powder is attributed to cubic ZrO$_2$. There is no N-H stretching for both the powder which confirms the absence of ammonium chloride.

Table 5.6 FTIR spectra of dried and calcined (260°C) washed precipitates (ROUTE 2)

Adsorption Peak (cm^{-1})		Identification
Raw Powder	Calcined at 260°C	
3000-3500		Molecular water
	3430	-OH
	3110	-OH
2360, 2343		Cl-
2084		H bonded OH
1634	1636	Sharp Zr-OH
1377		Zr-OH
1072	1070	Al-OH
	735	Al-O
	614,478	Zr-O

5.3.3 Phase Evolution of Calcined Washed Precipitates

The XRD pattern of washed Al_2O_3-ZrO_2 washed precipitates is shown in Fig. 5.23. The as dried precipitates have pseudoboehmite. This precipitate when heated at 260°C, the pattern changes to that of bayerite. At 550°C, broad peaks consisting of cubic ZrO_2 and transition Al_2O_3 appears. At 850°C, while ZrO_2 changes to a mixture of cubic + tetragonal, Al_2O_3 is present as γ-Al_2O_3. At 1050°C, the XRD pattern is consists of all the three forms of ZrO_2 (*m, t and c*) as well as γ-Al_2O_3. The crystallite size of ZrO_2 is 21.55 nm at this temperature.

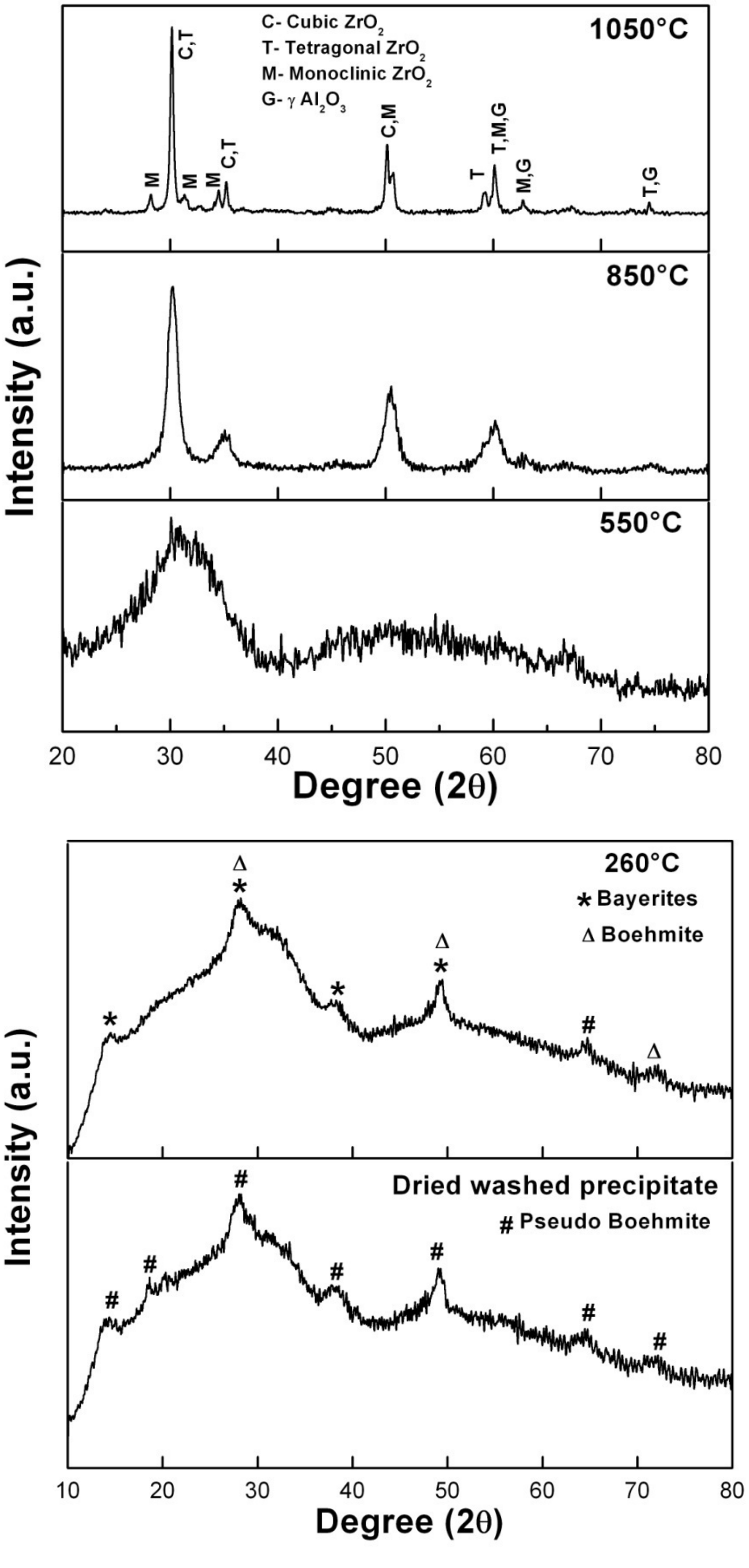

Fig.5.23. X-ray diffraction of Al_2O_3-ZrO_2 washed precipitates calcined at different temperature (ROUTE 3)

Table 5.7 Properties of calcined washed precipitates (ROUTE 3)

D_{50} (µm)	D_{BET} (nm)	D_{TEM} (nm)	P_j (Mpa)	S (m^2 gm^{-1})	AF
19.25	10	10-20	99	123	770

5.3.4 Particle Size, Pore Size distribution and Surface Area Analysis of Calcined Washed Precipitates

The particle size distribution of calcined washed precipitates is shown in Fig. 5.24. The agglomerate size has a wide distribution ranging from 1-100 µm. It is seen that 50% of the agglomerates are in the size range of 1-19 µm. The finer size fractions (1-3 µm) become distinct on water and alcohol washing.

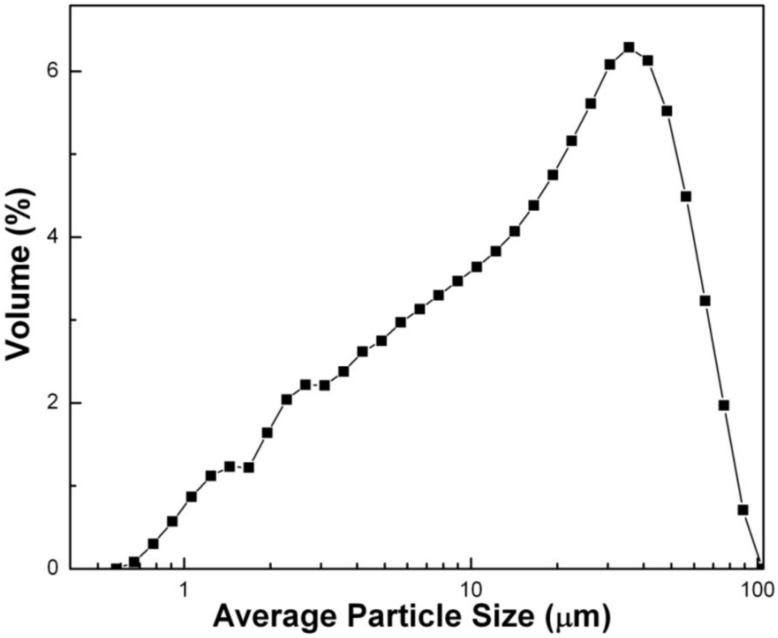

Fig.5.24. Particle size distribution of washed precipitates calcined at 850°C (ROUTE 3)

Thus the washing process is at least partially effective in breaking the agglomerates and reducing the apparent particle size. The specific surface area of the calcined powder is 123 m^2 gm^{-1} and the calculated particle size (D_{BET}) is 10 nm. The predominant pore width is around 1.5, 2.7 and 6.2 nm indicating a combination of micro and mesopore (pore size >2 nm).

5.3.5 TEM Analysis

Figure 5.25 (a, b) shows the bright field image and diffraction pattern respectively of the calcined powder. Both Al_2O_3 and ZrO_2 have comparable particle sizes (10 – 20 nm). Thus the particle size obtained from TEM matches well with the crystallite size (7.53 nm) obtained from X-ray line broadening. The corresponding electron diffraction pattern shows distinct ring pattern. Thus the calcined composite powder is well crystallized at 850^{o}C.

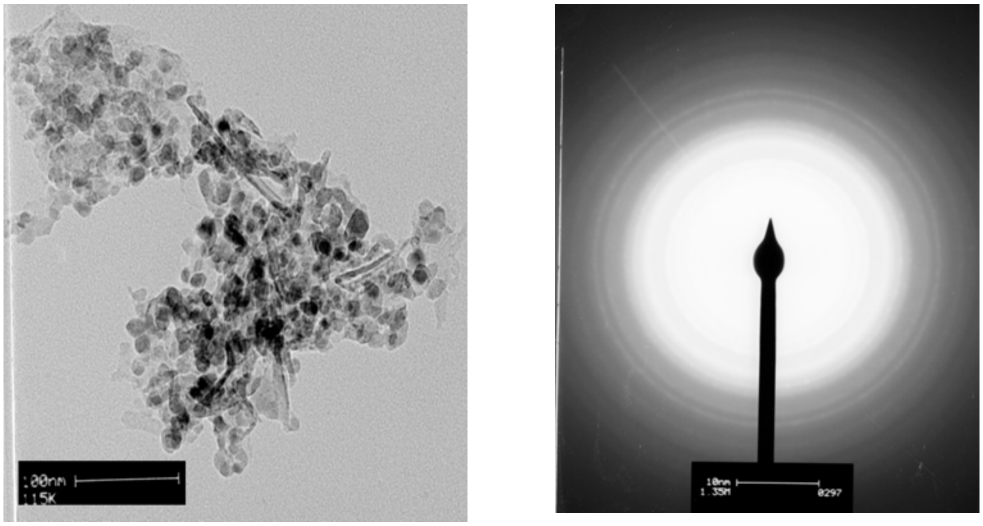

Fig.5.25. (a) TEM micrograph and (b) diffraction pattern of Al_2O_3-ZrO_2 washed precipitates calcined at 850°C (ROUTE 3)

5.3.6 Compaction Behaviour of Calcined Washed Precipitates

The calcined powder was uniaxially pressed and the green densities were plotted as a function of log applied pressure (Fig. 5.26). The agglomerate strength of the powder is found to be 99 MPa. The agglomerate strength is much lower than the unwashed powder (126 MPa). The calcined powder has smaller AF (770) which signifies lesser agglomeration tendency of these powders. The water washing followed by alcohol washing prevents strong interparticle bonding during drying process thereby reducing the capillary forces. The dried powder is fluffy and softly agglomerated.

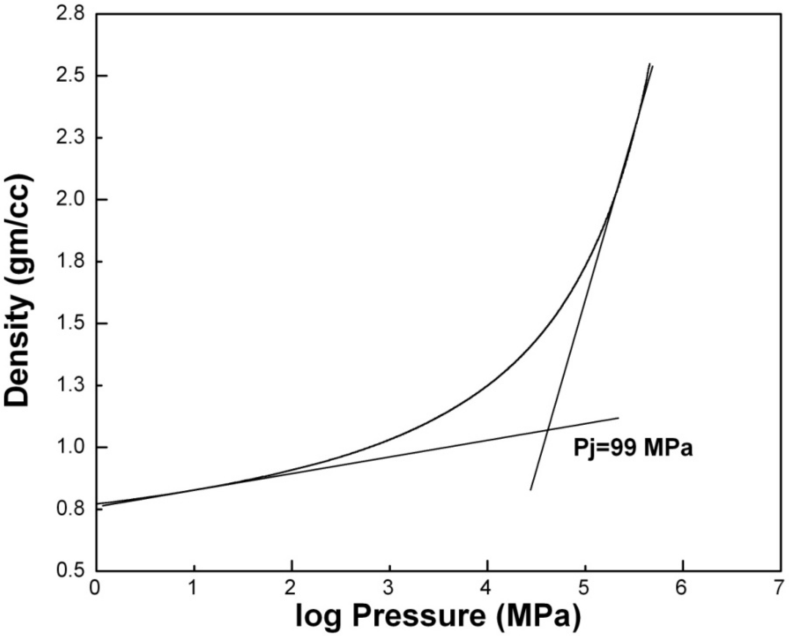

Fig.5.26. Compaction behaviour of calcined Al_2O_3-ZrO_2 washed precipitates (ROUTE 3)

5.3.7 Sintered Density and Microstructure

The effect of sintering temperature on the density of Al_2O_3–ZrO_2 composite is shown in Fig. 5.27. The sintering of the pellets showed nearly isotropic shrinkage over the temperature range 1400-1600^oC with the anisotropy factor (ratio of radial to transverse shrinkage) varying between 1.03-1.04.The relative sintered density increases with temperature with complete transformation of tetragonal ZrO_2 to monoclinic phase. In the present study, the Al_2O_3–ZrO_2 composite could be densified only up to 90%, the lower sintered density resulted from the incomplete pore removal. It may be noted that during the sintering process, a further sample weight loss of 9.4% was recorded. This magnitude of the weight loss is definitely more than that expected for the binder burnout. It is postulated that this extra weight loss comes from the residual chlorides or hydroxyl ions (in hydrated Al_2O_3) which go off at high temperature leaving behind a porous structure. This enables the grains to grow at a rapid rate without a corresponding decrease in porosity or pore removal. Thus the final microstructure becomes porous with relatively large grains (in μm) of Al_2O_3 and ZrO_2.The microstructure of polished and etched sample of sintered Al_2O_3-ZrO_2 composites is shown in Fig. 5.28. The Al_2O_3 has a narrow grain size distribution.

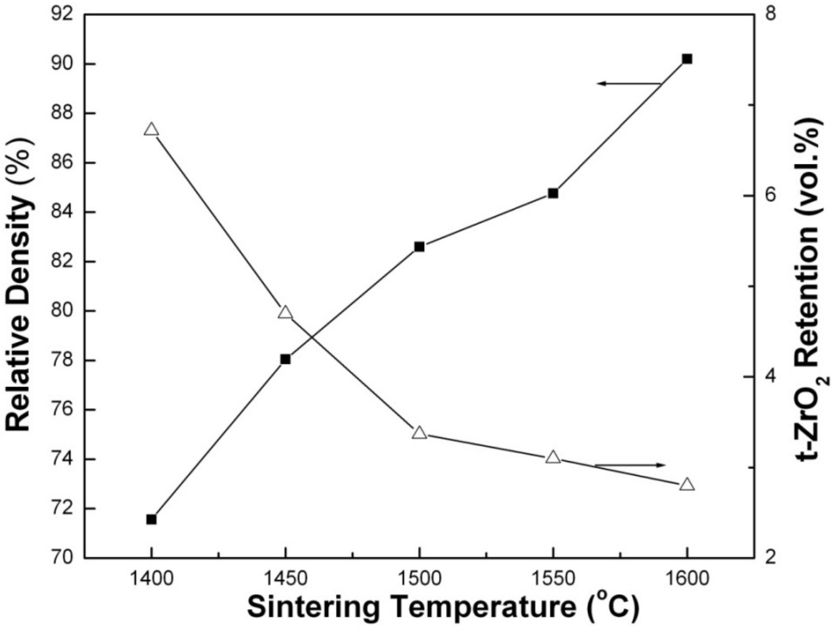

Fig.5.27. Relative density and t-ZrO_2 phase retention as a function of sintering temperature for the Al_2O_3-ZrO_2 composites (ROUTE 3)

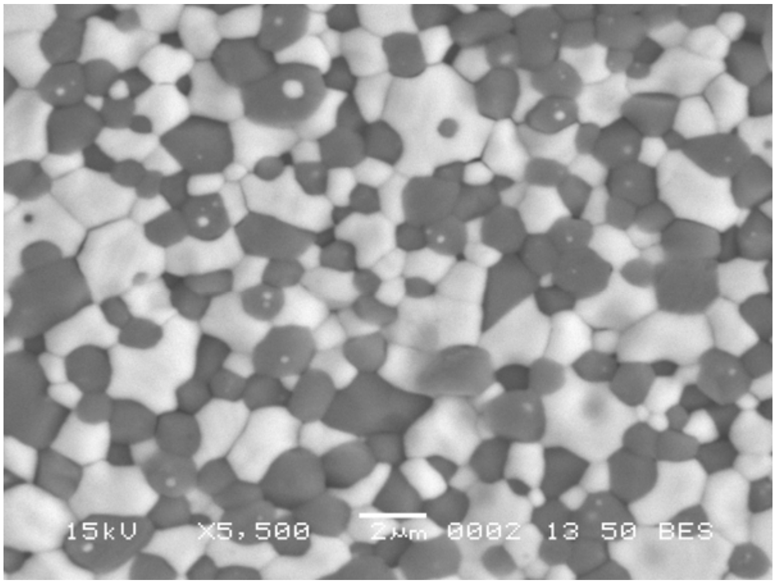

Fig.5.28. (A) SEM micrograph of Al_2O_3-ZrO_2 composite sintered at 1600°C

The microstructure is homogeneous but has both inter and intragranular ZrO_2 was observed in the matrix Fig.5.28 (A) TEM image shows that microcracks are present at the Al_2O_3- ZrO_2 grain boundary [Fig.5.28 (B)] along with twining cracks (arrow marked). The coarsening of the microstructure probably results due to the limited solid solubility of

Al_2O_3 and ZrO_2 phases. The average grain size of Al_2O_3 and ZrO_2 are 1.9 ±.7 μm, 1.5 ± 0.60 μm respectively.

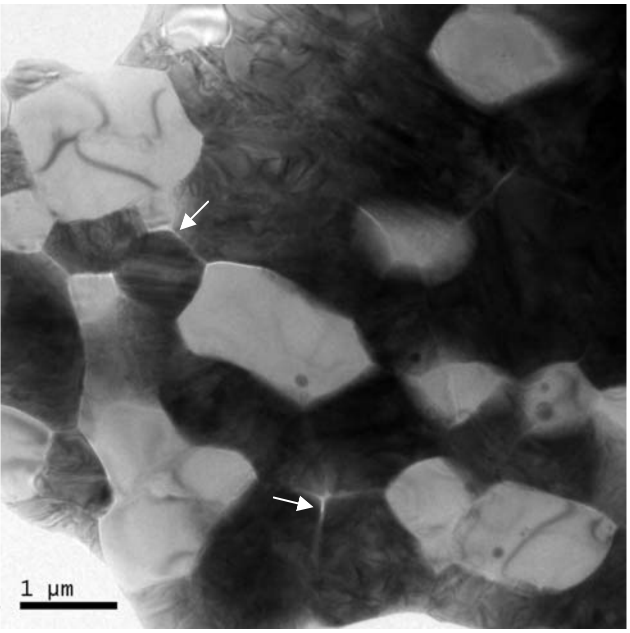

T

Fig.5.28. (B) TEM micrograph of sintered Al_2O_3-ZrO_2 composite (ROUTE 3)

5.3.8 Hardness and Biaxial Flexural Strength

The Vickers hardness of the sintered Al_2O_3-ZrO_2 composite sample is shown in Fig. 5.29.

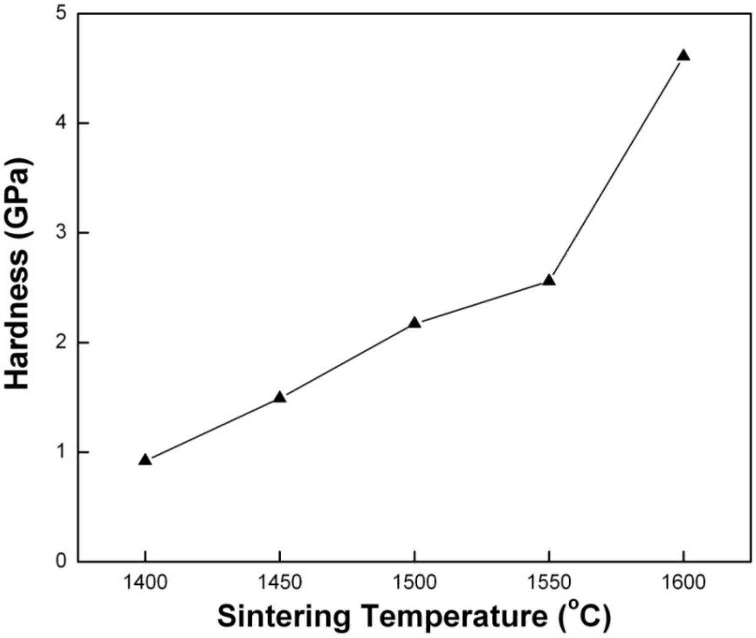

Fig.5.29. Variation of hardness with sintering temperature (ROUTE 3)

Although the fraction of retained *t*-ZrO_2 decreases with sintering temperature, the hardness as well as sintered density continuously increases with sintering temperature till 1600°C.The above increase in the hardness of the Al_2O_3-ZrO_2 composite could be related to the density increment. It appears that the phases of the sintered composite have least influence on the hardness. The biaxial flexural strength of the sintered sample was determined on circular specimen. The strength increases with increase in sintering temperature (Fig. 5.30). The lower value of strength is due to the combined effect of porous microstructure and microcracking (the later resulting from spontaneous $t \rightarrow m$ ZrO_2 transformation).

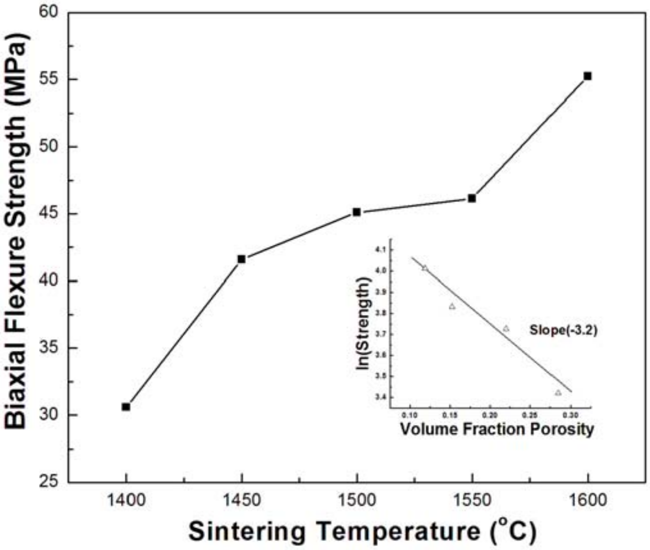

Fig.5.30. Effect of sintering temperature on biaxial flexure strength of Al_2O_3-ZrO_2 composite (ROUTE 3)

The strength of the composite show an exponential relationship with porosity and the highest biaxial strength of the composite was 55 MPa. The three point bending strength at 1600°C was 63.7± 2.6 MPa, which is higher than that of biaxial strength. Since the biaxial flexure takes place due to more severe tensile stress state in the sample, its value is usually lower than that obtained with three point bending test. Thus it is observed that the Al_2O_3–ZrO_2 composite powder prepared by precipitation route using chloride precursors at higher pH (8.7-9.1) has fine crystallites and high surface area as compared to the powder prepared by gelation method. The subsequent post precipitation treatment of water and iso propyl alcohol washing resulted in soft and porous agglomerates which improved the densification.

SENB fracture toughness (K_{IC}) measured in three point bending (1600^{0}C sintered sample) was 1.75 MPa√m, which is lower than pure and dense Al_2O_3 ceramics. It thus appears that the extensive matrix microcracking due to spontaneous transformation of ZrO_2 associated with low density porous microstructure has resulted in poor toughness

The density of the samples could be increased to 90% of the theoretical. However, even then *t*-ZrO_2 phase could not be retained in the significant fraction in the sintered sample. As already mentioned, residual chlorides may affect the densification. Thus it was decided to partially reduce the chloride content of the precursors by replacing $AlCl_3$ with $Al(NO_3)_3$.

5.4 *Al_2O_3-ZrO_2 Composite Prepared by Precipitation using Nitrate and Chloride Precursors: Effect of Hot Water and Alcohol Washing (ROUTE 4)*

As already mentioned, the presence of residual chloride in the powder affects its densification behaviour. Therefore, it was decided to replace one of the precursors ($AlCl_3$) with $Al(NO_3)_3$ to study the effect of precursor on density and phase retention of the sintered Al_2O_3- ZrO_2 composites. Since zirconyl nitrate is costly and difficult to work with, $Al(NO_3)_3$ (because of its ready availability and better workability) replaced $AlCl_3$ while $ZrOCl_2$ was retained as ZrO_2 precursor for Al_2O_3-ZrO_2 composite processing.

The Al_2O_3-ZrO_2 composite was prepared by precipitation at higher pH 8.7-9.1 from a mixed solution of $Al(NO_3)_3$ and $ZrOCl_2.8H_2O$.The precipitate was washed with hot water to remove the excess NH_4OH and NH_4Cl followed by washing with propanol. The effect of washing on the properties of Al_2O_3-ZrO_2 composite is discussed in the following sections.

5.4.1 Thermal Analysis of Dried Washed Precipitates

The DSC/TG plot of the as dried washed precipitates is shown in Fig. 5.31. The DSC curve in this case shows an endothermic peak at 110°C, a sharp exothermic peak at about 260°C and another endothermic peak at 280^{0}C respectively. In between the first endothermic peak at 100^{o}C and first exothermic peak at 260°C there is another endothermic peak at 122^{o}C (indicated by slope change). At higher temperature the DSC curve shows a sharp endothermic peak at 280^{o}C and broad endothermic peak at 357^{o}C followed by exothermic peaks at 420^{o}C and 780°C respectively. Finally there is a broad hump around 1000^{o}C. The TG curve of the gel shows a gradual weight loss of about 14.58% in the temperature range 30 - 250^{0}C which takes place in two stages. The first stage weight loss is 9% and second stage weight loss (between 100-225°C) is 5.4%.

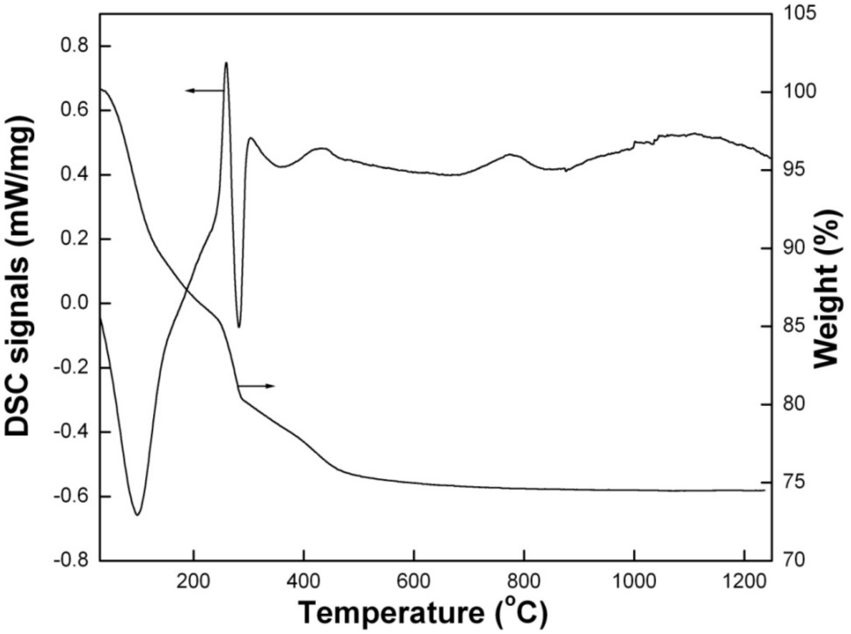

Fig.5.31. DSC/TG thermogram of dried washed precipitates (ROUTE 4)

A sharp weight loss of 5.6% is recorded in the temperature range 250 – 300°C followed by another weight loss of 5.5% occurring between 300 and 500°C.The X-ray diffraction pattern of as dried uncalcined powder shows the presence of disordered bayerite. It is reported [5.16] that the dedydroxylation of bayerite ($Al_2O_3.3H_2O$) took place in two stages. In the first stage, bayerite decomposes to boehmite according to the reaction:

$$Al(OH)_3 = AlO(OH) + H_2O \qquad (5.6)$$

In the present study, the weight loss for this stage is 9.4%. In the second stage, boehmite decomposes to form amorphous Al_2O_3 with a weight loss of 6% following the reaction given below:

$$2AlO(OH) = Al_2O_3 + H_2O \tag{5.7}$$

The total weight loss is 15.4%. Subsequently the amorphous Al_2O_3 crystallizes to γ-Al_2O_3 at 260°C. The observed weight loss (14.58%) matches well with the calculated weight loss.

Following this exothermic peak, a sharp endothermic peak occurs at 280°C associated with a total weight loss of 11.1% occurring in two stages. The most probable reaction which will describe the decomposition of $Zr(OH)_4$ [5.17,5.18] are as follows:

$$Zr(OH)_4 = ZrO(OH)_2 + H_2O \tag{5.8}$$

$$ZrO(OH)_2 = ZrO_2 + H_2O \tag{5.9}$$

The first stage of weight loss (5.54%) takes place between 250°C and 300°C, the second stage of weight loss (5.56%) is between 300°C and 450°C. Since the weight loss of ZrO_2 takes place in two stages, it can be assumed that $Zr(OH)_4$ first completely decomposes to $ZrO(OH)_2$ (Eqn. 5.8) and subsequently $ZrO(OH)_2$ decomposes to ZrO_2 (Eqn. 5.9). The weight loss for Eqn. (5.8) and (5.9) would have been 6.9% and 7.8% respectively for equal volume composition. However, since the observed weight loss is less than the theoretical weight. It is possible that some overlapping of reaction (5.8) and (5.9) takes place and the following sequence is proposed:

In the first stage a small fraction of $Zr(OH)_4$ directly convert to ZrO_2 according to the reaction (Eqn. 5.4) and the remaining fraction of $Zr(OH)_4$ converts to $ZrO(OH)_2$ according to the reaction (Eqn.5.8). This $ZrO(OH)_2$ subsequently decomposes to ZrO_2 in the second stage according to the reaction (Eqn. 5.9).

On back calculating from the final product, it is found that weight loss of 5.54% in the first stage corresponds to decomposition of 16.8% of $Zr(OH)_4$. This fraction of $Zr(OH)_4$ directly converts to ZrO_2 and the remaining 83.2% of $Zr(OH)_4$ converts to $ZrO(OH)_2$. In the second stage, this 83.2% $ZrO(OH)_2$ converts to ZrO_2.

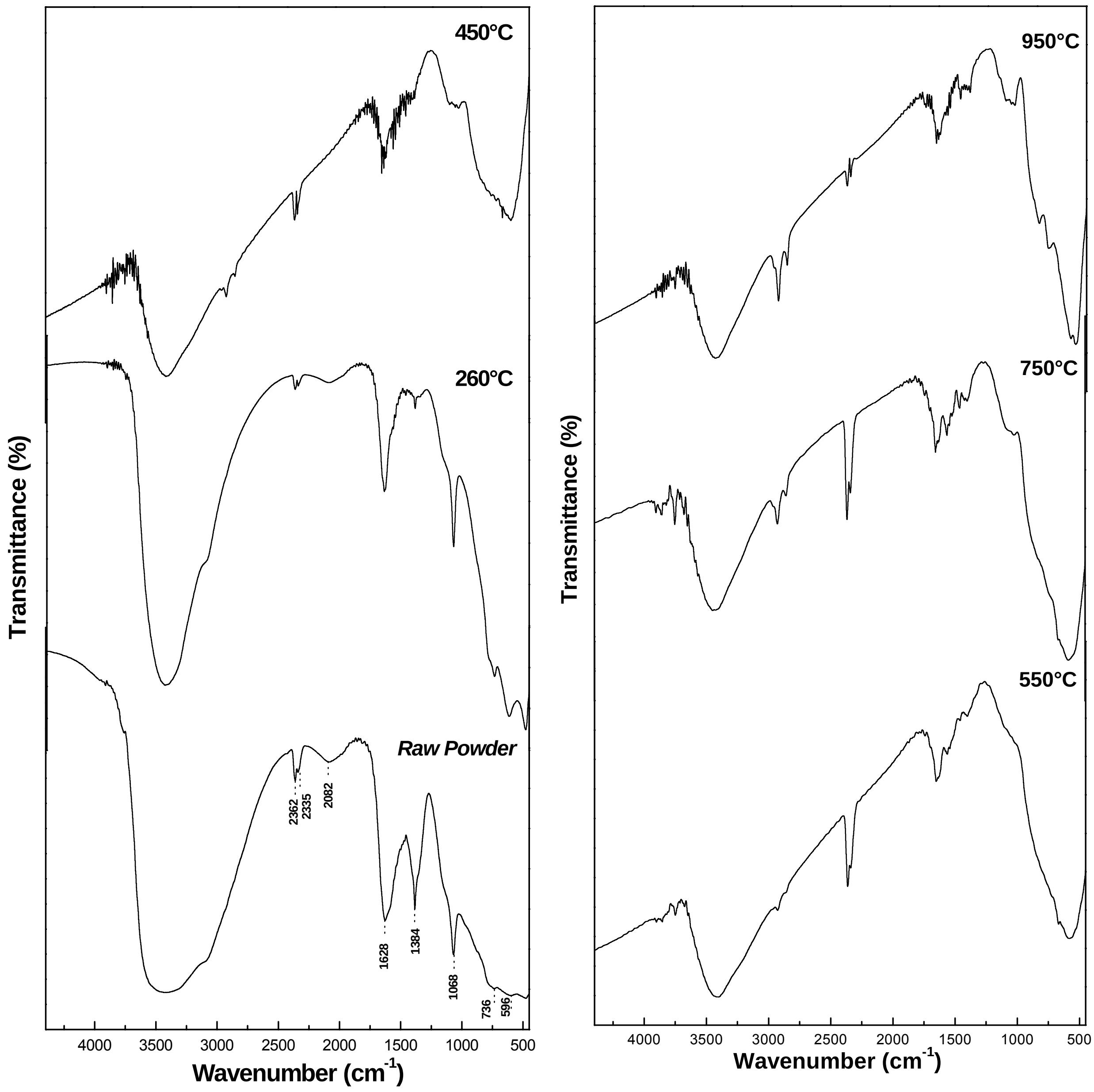

Fig.5.32. IR spectra of Al_2O_3- ZrO_2 dried and calcined washed Precipitates (ROUTE 4)

5.4.2 FTIR Analysis

The nature of bonds present in dried washed precipitates was studied by FTIR analysis and shown in Fig. 5.32. The broad band at 3200-3600 cm^{-1} in raw powder is assigned to asymmetric and symmetric stretching vibration of $(OH)^{-1}$ group. The sharp peaks at 2362 and 2335 cm^{-1} are due to bending vibration of Cl^- group. The peak positions at 1628 and 1384 cm^{-1} result from the bending vibration of Zr-OH group. The stretching vibrations are also present in the 260°C calcined powder but the peaks become sharp and strong [Table 5.8].

Table 5.8 FTIR spectra of Al_2O_3-ZrO_2 powder calcined at different temperature (ROUTE 4)

Raw powder	Calcination Temperature				
	260°C	*450°C*	*550°C*	*750°C*	*950°C*
3911			3751	3904	
3478	3435	3418	3422	3859	3418
3092	3085	2922	2932	3753	2920
2425		2854	2856	3681	2853
2362	2366	2370	2367	3451	
2335	2343	2341	2340	2928	2341
2082	2099			2858	
1628	1636	1632	1652	2370	1670
1384	1384	1448	1567	2342	
1068	1068		1455	1653	
872			1408	1565	830
760	734			1461	760
610	613	606	583	1403	573
	478			587	538

The stretching positions of raw powder as well as calcined powder are quite similar. The relative intensity of all possible peaks is higher for calcined powder. The peaks at 1068 and 734 cm^{-1} correspond to Al-OH bond. In the powder calcined at 450°C, the stretching vibrations at 613 and 478 cm^{-1} were attributed to cubic ZrO_2. The peaks at 3420 and 1670 cm^{-1} were present till 950°C corresponding to the Al-OH stretching vibration. The stretching of crystalline Zr–O bonds show absorption bands at lower frequencies of 760 and 538 cm^{-1} and 573 cm^{-1}, which is an Al-O octahedral band at 950°C. IR spectra show that a trace amount of $(OH)^{-1}$ group still remains in the structure of Al_2O_3-ZrO_2 composites even after heating at 1000°C. Similar results have also been observed by

Sarkar [5.22]**.** This causes a weight loss of Al_2O_3-ZrO_2 composites samples during sintering which is explained in later sections.

Table No 5.9 Properties of calcined powder (ROUTE 4)

D_{50} (μm)	D_{BET} (nm)	D_{TEM} (nm)	P_j (MPa)	S ($m^2\ gm^{-1}$)	AF
3.54	7.27	10-15	98	170	120

5.4.3 Phase Evolution of Calcined Powder

The XRD pattern of dried washed precipitates is shown in Fig. 5.33 as a function of calcination temperature. The dried precipitates contain disordered bayerite (JCPDS 22-0011), while ZrO_2 is in amorphous state. At 260°C, the bayerite changes to boehmite. A mixture of poorly crystalline cubic ZrO_2 and transitional Al_2O_3 is observed at 550°C. At 750°C cubic ZrO_2 appears along with γ-Al_2O_3. Finally at 1050°C, ZrO_2 consists of a mixture of cubic + tetragonal while Al_2O_3 is present as γ-Al_2O_3

5.4.4 Particle Size, Pore Size Distribution and Surface Area Analysis of Calcined Powder

The particle size of washed calcined precipitates is distributed between 1-20 μm. The calcined powder had monomodal particle distribution with average size of 3.54 μm. The specific surface area of the calcined powder is 170 $m^2\ gm^{-1}$ and the calculated particle size (D_{BET}) is 7.27 nm. Both micro and meso pores are present in the calcined powder. The agglomeration factor AF is much lower (120) than the precipitated and washed powder prepared from all chloride precursors indicating that residual chloride ion play a role in determining the agglomerate strength.

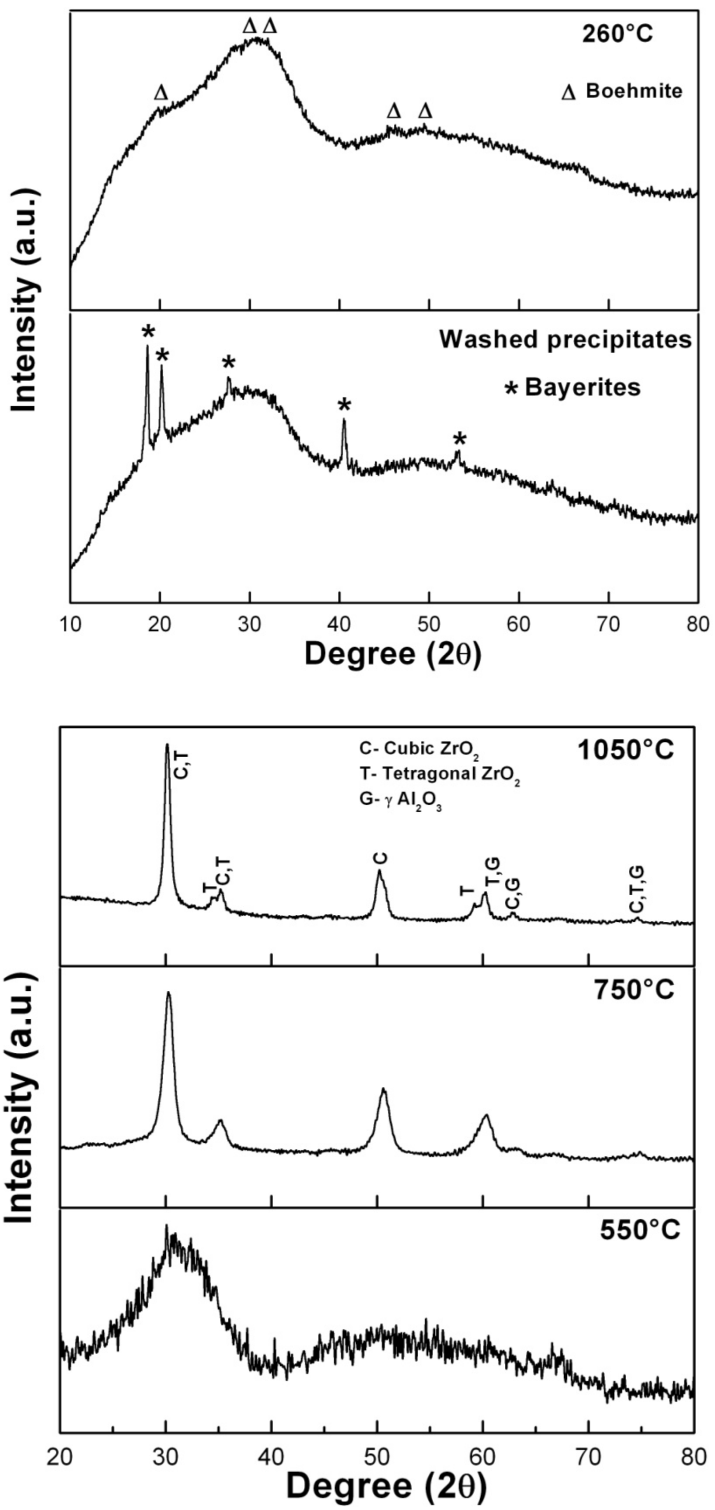

Fig.5.33. X-ray diffraction of Al_2O_3-ZrO_2 powder calcined at different temperature (ROUTE 4)

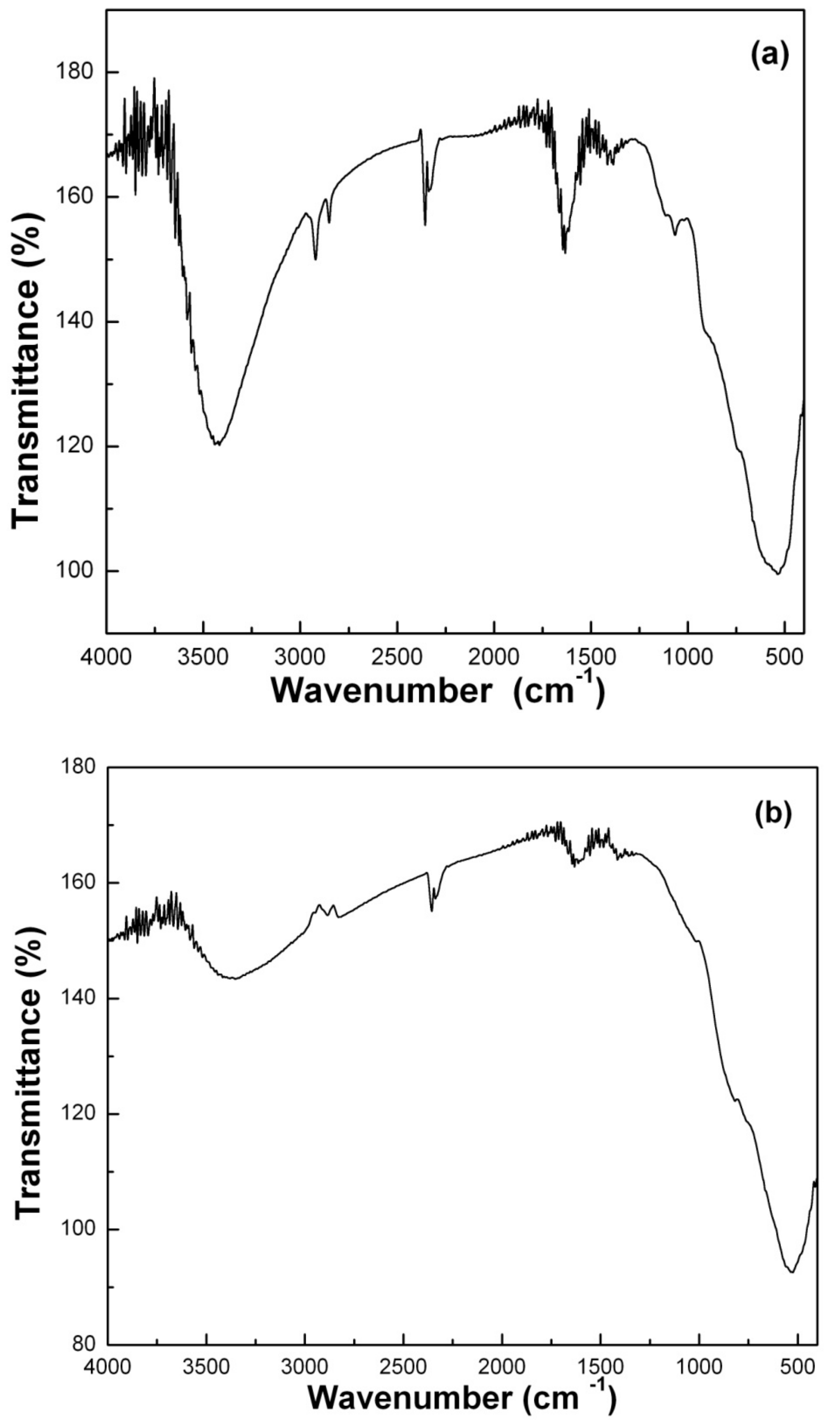

Fig.5.34. FTIR spectra of calcined Al_2O_3-ZrO_2 precipitates (a) for all chloride precursors and (b) for chloride- nitrate combination precursor (ROUTE 4)

A rough estimate of the relative chloride concentration in the two type of calcined powders (i.e. one prepared from all chloride precursors and the other prepared from the combination of nitrate and chloride precursors) was made by studying the FTIR study of calcined powders of the above two types. The results are reproduced in Fig 5.34(a) (for all chloride precursors) and 5.34(b) (for chloride- nitrate combination precursor). The chloride peak is detected from the shoulder peak 2360 and 2330 cm^{-1} [5.2]. The Fig shows that the relative concentration of chloride is less when the precursor is a combination of chloride and nitrate. The lower amount of chloride in chloride-nitrate combination helps in achieving a higher density of the latter samples.

5.4.5 TEM Analysis

The TEM microstructure of the calcined washed precipitates is shown in Fig. 5.35. The micrograph shows fine spherical shaped particles in the range of 10-15 nm size. There is no difference in particle size and that of the crystallite size calculated from XRD and particle size from surface area. Hence the particles behave like individual crystal without clustering. The particle size shows a narrow range distribution.

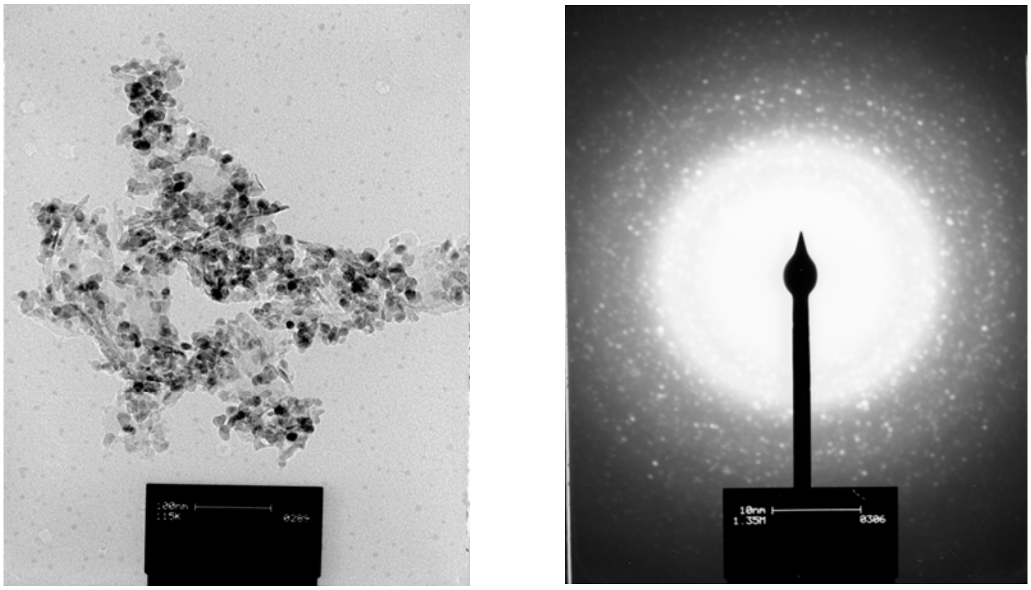

Fig.5.35. TEM micrograph and diffraction patterns of Al_2O_3-ZrO_2 850℃ calcined power (ROUTE 4)

5.4.6 Compaction Behaviour of Powder

The compaction behaviour of the calcined washed precipitates is shown in Fig. 5.36. As the powder was less agglomerated (AF 120), the powder was soft and fluffy and compaction was easy. The linear behaviour of the curve at lower pressure range signifies that the packing is done by rearrangement of particle which behaves like loose mass instead of a coherent mass. Hence, it may be said that P_j value decreases with decreases in agglomerate size. But it was difficult to exactly find out P_j value due to the rounding of the curve. However, it appears to be about 98 MPa. The compaction constant 'M' calculated from Eqn. 5.5 is 7.4 which is in the range of soft agglomerate.

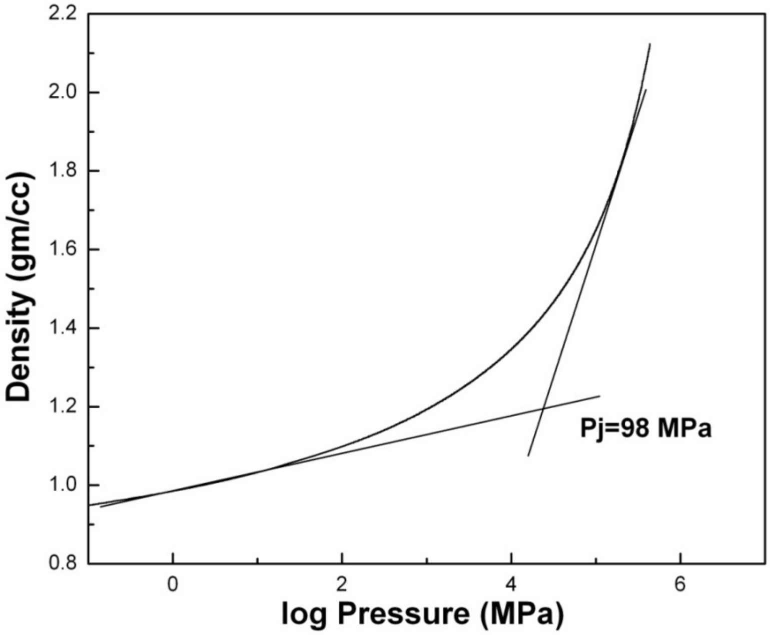

Fig.5.36. Compaction behaviour of the Al_2O_3-ZrO_2 power during uniaxial compaction (ROUTE 4)

5.4.7 Sintering and Microstructure

The densification behavior of Al_2O_3-ZrO_2 composites as a function of sintering temperature is shown in Fig. 5.37. The relative density increases linearly with temperature till 1500°C. The anisotropy factor decreased with increase in sintering temperature till 1450°C (90% theoretical density) and remained unchanged thereafter. The microstructure of polished and etched sintered sample (1600°C) (Fig. 5.38) shows that the average grain size of Al_2O_3 and ZrO_2 are 1.77 ± 0.79 μm, 1.27± 0.25 μm respectively. The spherical ZrO_2 was present mostly in intergranular position. The improvement in density in Route 4 samples (as compared to Route 3 samples) is due to the combined effect of water and alcohol washing. It has already been discussed in the literature review section of the powder processing chapter that the presences of both chloride ions as well as hard agglomerates affect the density improvement. While water washing has reduced the chloride content alcohol washing has produced the soft agglomerates. The presence of soft agglomerates has improved the sintered density. The M value is 3% which indicate the soft agglomerate.

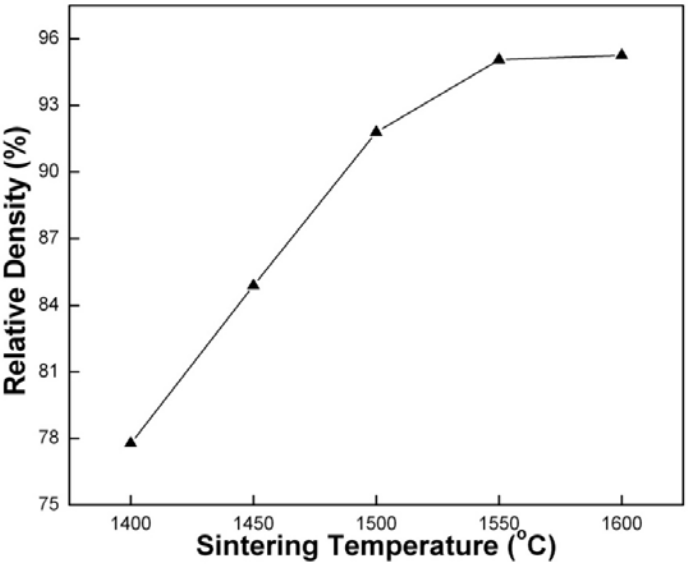

Fig.5.37.Relative density of Al_2O_3-ZrO_2 composites as a function of sintering temperature (ROUTE 4)

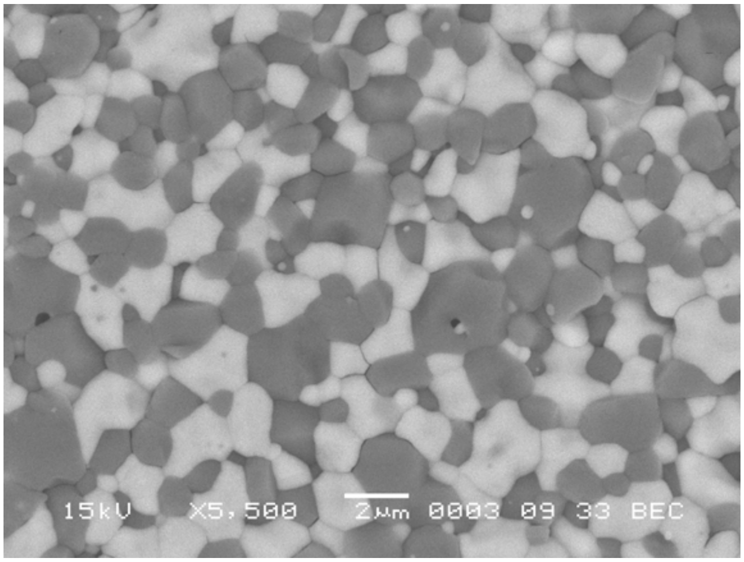

Fig.5.38. SEM micrograph of Al_2O_3- ZrO_2 composite sintered at 1600°C (ROUTE 4)

TEM microstructure (Fig. 5.39) shows that the microcracks (generated due to the spontaneous transformation of *t*-ZrO_2 on cooling) are present at the Al_2O_3- ZrO_2 grain boundary and show a twin like appearance.

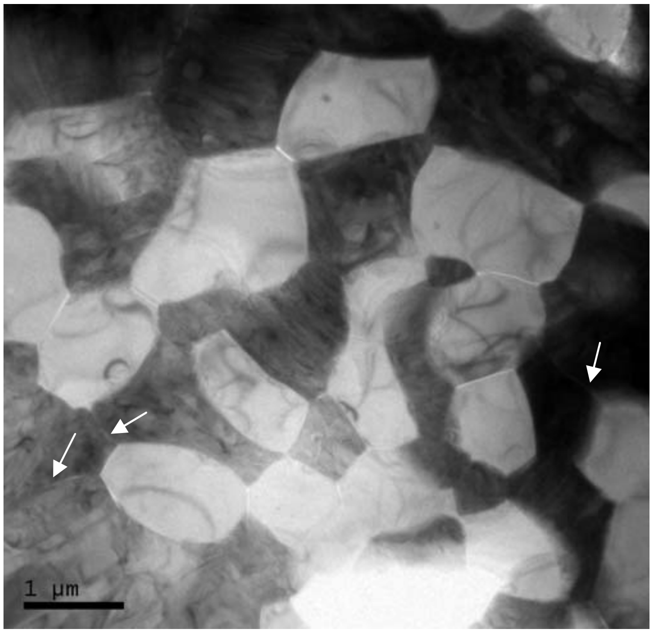

Fig.5.39. TEM micrograph of sintered Al_2O_3-ZrO_2 composite (ROUTE 4)

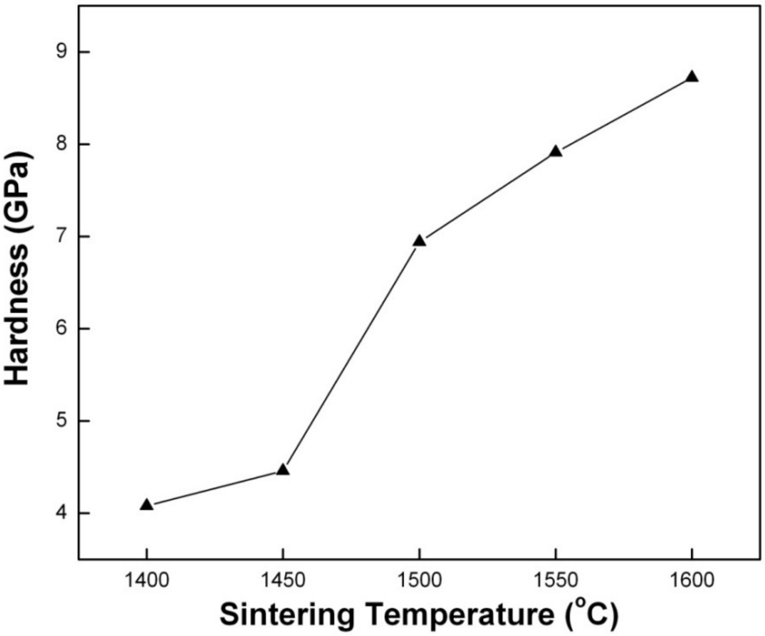

Fig.5.40. Effect of sintering temperature on hardness of Al_2O_3-ZrO_2 composite (ROUTE 4)

5.4.8 Hardness and Biaxial flexural strength

The Vickers hardness of the sintered Al_2O_3-ZrO_2 composite sample is shown in Fig. 5.41. The hardness variation of the present samples (prepared from nitrate chloride precursor combination) exhibit similar hardness trend observed for the samples prepared from all chloride precursors. However, in this case, the increase in hardness is slow between 1400-1450^{o}C (4.08 to 4.46 GPa), followed by a rapid increase to 8.7 GPa at 1600^{o}C and finally between 1500 to 1600^{o}C the increase is steady and linear although, the rate of increase is slow. The above increase in the hardness of the Al_2O_3-ZrO_2 composite could be related to the density increment. It appears that the phases of the sintered composite have least influence on the hardness.

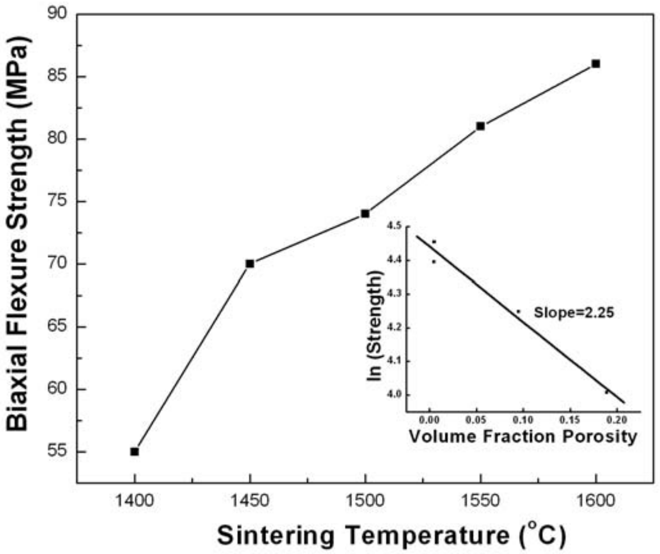

Fig.5.41. Effect of sintering temperature on biaxial flexure strength of Al_2O_3-ZrO_2 composite (ROUTE 4)

The biaxial flexural strength of the sintered sample increases with sintering temperature and also have a porosity dependence as shown in Fig.5.41.The lower strength value is due to the porous microstructure and high density of microcracks generated due to the spontaneous transformation of $t \rightarrow m$ ZrO_2 as well due to the thermal expansion between the two phases.

SENB fracture toughness (K_{IC}) measured in three point bending (1600^{0}C sintered sample) was 1.9 MPa$\sqrt{}$m, which is lower than pure and dense Al_2O_3 ceramics. It thus appears that the extensive matrix microcracking due to spontaneous transformation of ZrO_2 associated with low density porous microstructure has resulted in poor toughness The Al_2O_3-ZrO_2 composite prepared from precipitation of $Al(NO_3)_3$ and $ZrOCl_2$ followed by hot water and alcohol washing crystallized at higher temperature. TEM microstructure of the calcined powder showed monomodal particle distribution having 10-15 nm primary particles. The composite had been densified to 95% of the theoretical density at 1600°C.Thus the Al_2O_3-ZrO_2 composite prepared from the combination of $Al(NO_3)_3$ and $ZrOCl_2$ showed better densification in comparison to Al_2O_3-ZrO_2 composites prepared from all chloride precursors. However, even with high density, *t*-ZrO_2 could not be retained. This was probably due to the low matrix modulus of the composite. The calculated composite modulus (assuming *t*-ZrO_2) was 296 GPa. The failure to retain *t*-ZrO_2 caused matrix microcracking which is responsible for the observed poor mechanical behavior of the composite. Thus, it was decided to use Y_2O_3 as stabilizer for ZrO_2.The Al_2O_3-Y_2O_3-ZrO_2 composites having nominally equal volume fraction of Al_2O_3 and Y-ZrO_2 will be prepared using the same process flow diagram as before and the properties will be evaluated.

Table 5.10 Physical properties of the calcined powder at a glance

ROUTE	Av Particle size calculated from			Agglomerate strength P_j (MPa)	BET Surface area S (m^2/gm)	Agglomeration factor AF
	Particle size measurement D_{50} (µm)	surface area measurement D_{BET} (nm)	TEM micrograph D_{TEM} (nm)			
1	35.47	51	25	134	49	1418
2	30.4	17.42	22.5	126	71	1216
3	19.25	10	10-20	99	123	770
4	3.54	7.27	10-15	98	170	120

Section B

Effect of Y_2O_3 doping on the properties of Al_2O_3-ZrO_2 Composites

5.5.1 Processing of Al_2O_3-Y-ZrO_2 Composites

In the previous sections the densification behavior, mechanical properties and microstructure of Al_2O_3-ZrO_2 composites was discussed. It was observed that the precursors (especially anions) as well as the processing route controlled the density, microstructure as well as the mechanical properties of the sintered composite. The poor mechanical properties in an otherwise reasonably dense composite were attributed to extensive microcracks resulting from the spontaneous *t*→m transformation during cooling from the sintering temperature as well as to the residual pores. Due to higher volume percentage of ZrO_2, the reduced elastic modulus of matrix could not retain *t*-ZrO_2, although the grain size was small. Therefore, it was decided to add Y_2O_3 (1, 2, 2.5, and 3 mol %) for stabilizing *t*-ZrO_2. All the Y_2O_3 doped composites were prepared by precipitation route using $Al(NO_3)_3$, $ZrOCl_2$, and $Y(NO_3)_3$ as the precursors and the precipitates were washed as before (Modified ROUTE 4 Section 4.2.4) prior to calcination.

5.5.2 Densification Behaviour of Al_2O_3-Y-ZrO_2 composites

The sintered density of Al_2O_3-Y-ZrO_2 composites as a function of sintering temperature is shown in Fig. 5.42. The sintered density increases with the increase in sintering temperature from 1400 to 1600°C. At any fixed sintering temperature, sintered density is higher for samples having higher Y_2O_3. The higher density of the Al_2O_3-Y-ZrO_2 composites is attributed to the oxygen vacancy concentration in the Y_2O_3 doped samples. Although Y_2O_3 addition did not alter the densification mechanism (or the activation energy), the density increased with Y_2O_3 content.

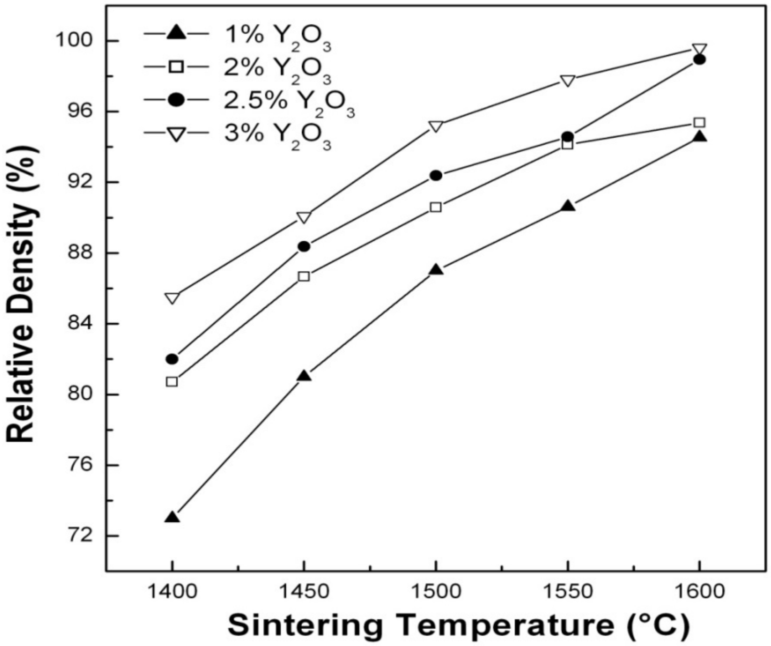

Fig.5.42. Relative Density of Al_2O_3-Y-ZrO_2 composites as function of Y_2O_3 content

5.5.3 Tetragonal-ZrO_2 phase retention in sintered Al_2O_3-Y-ZrO_2 composites

The *t*-ZrO_2 phase retention as a function of sintering temperature and Y_2O_3 content of the Al_2O_3-Y-ZrO_2 composites has been given in Fig. 5.43. The *t*-ZrO_2 retention also increases with Y_2O_3 addition with the trend similar to that observed for density variation. The maximum t-ZrO_2 retention is ~100% at 3 mol% Y_2O_3 addition. The *t*-ZrO_2 retention is very low in the composites prepared with 1.0 mol% Y_2O_3 and remain almost constant throughout the sintering temperature. However, the *t*-ZrO_2 retention for the samples prepared with 2 mol% Y_2O_3 decreases with increase in sintering temperature. The decrease in *t*-ZrO_2 retention with sintering temperature is attributed to the grain growth ZrO_2 grains. The samples prepared with high Y_2O_3 content the retention is high nearly 100% retention was observed in the sintering temperature studied.

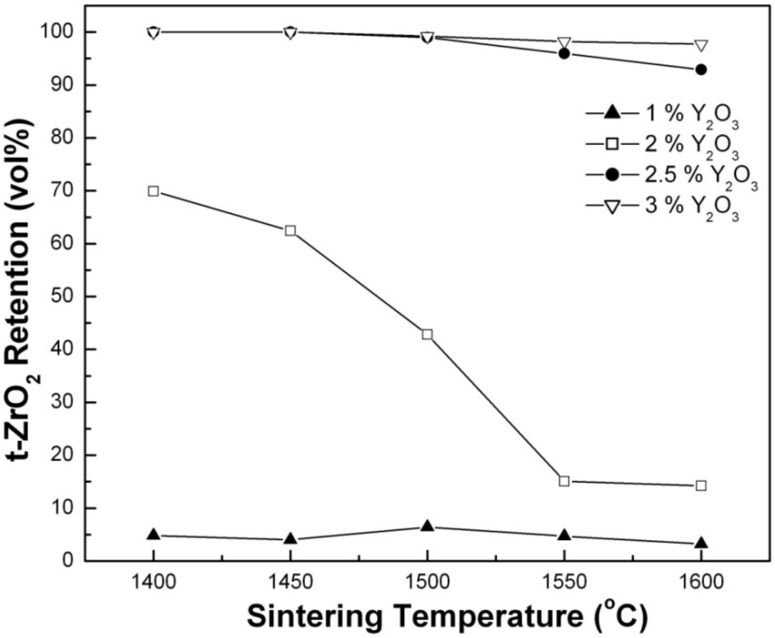

Fig.5.43. Tetragonal retention of Al_2O_3-Y-ZrO_2 composites as function of Y_2O_3 content

5.5.4 Effect of Y_2O_3 addition on the sintering kinetics of Al_2O_3-ZrO_2 composites

The non-isothermal densification behaviour of Al_2O_3-3Y-ZrO_2 was shown in Fig.5.44.The densification starts around 900°C and continues till 1450°C. It could be seen from the Fig.5.44 that Y_2O_3 doped composite has higher shrinkage as compared to undoped Al_2O_3-ZrO_2 composites. The higher shrinkage observed in these samples is due to the enhanced densification of the samples resulting from the creation of oxygen defects due to addition of Y_2O_3 in the composites. The duplex densification behavior is also observed in these samples. An attempt has also been made to calculate the densification kinetic parameters for Al_2O_3-3Y-ZrO_2 composites from the isothermal densification behavior during initial stage of sintering. It has been observed that the Y_2O_3 addition did not affect the sintering mechanism during the initial stage. The analysis of the isothermal dilatometric data in the temperature range 900 to 1050°C with a 50°C interval revealed that the kinetic parameter *n* varied from 4.76 to 5.0. This observed *n* value indicates that the volume diffusion is the dominant densification mechanism of Al_2O_3-3Y-ZrO_2 composite.

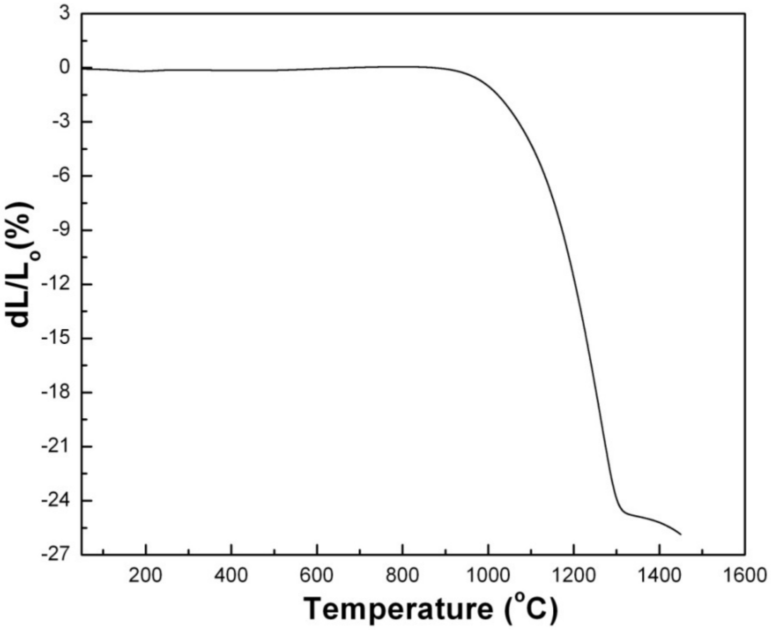

Fig.5.44.Non-isothermal densification behavior of **Al_2O_3-3Y-ZrO_2** ***composites***

Section C

Densification Kinetics of Al_2O_3-ZrO_2 Composites

5.6.1 Densification behavior of Al_2O_3-ZrO_2 composite prepared from different processing routes.

The non-isothermal densification behaviour of Al_2O_3-ZrO_2 composites has shown in Fig.5.45 as a function of different processing routes.

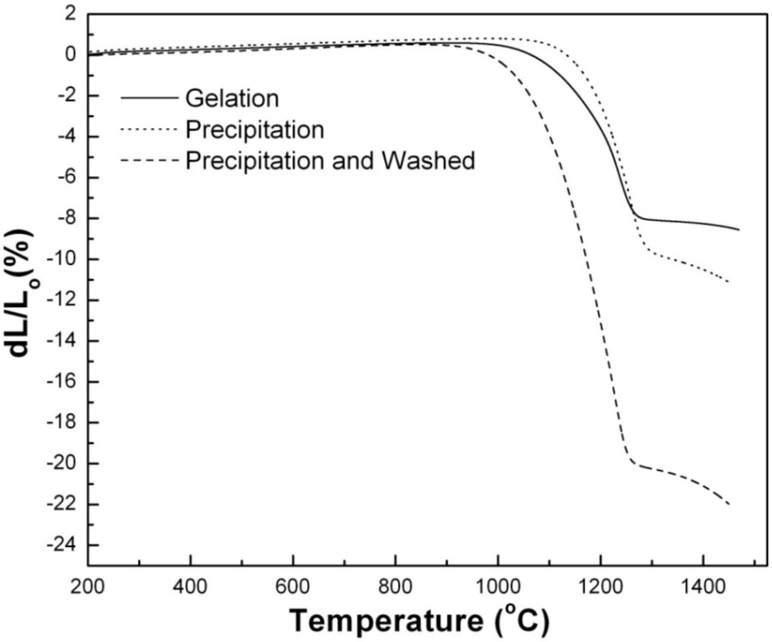

Fig.5.45. Non-isothermal densification behavior of Al_2O_3- ZrO_2 composites prepared by different processing routes

Figure 5.45 shows that in the lower temperature range (room temperature to 800°C), Al_2O_3-ZrO_2 compact under goes a small initial expansion due to the thermal expansion of the Al_2O_3-ZrO_2 composite powder compact followed by the onset of the shrinkage. The densification of Al_2O_3-ZrO_2 composite compact occurs in the temperature range 950 - 1130°C and the onset varied with the powder synthesis route. This onset temperature was related to the initial particle size and/or surface area of the powder and thus, the precipitated washed powder having higher specific surface area (123 m^2 gm^{-1}) along with finer particle size distribution showed a lower onset temperature for densification as compared to precipitated powder having lower specific surface area (71 m^2 gm^{-1}) [5.19]. The densification of Al_2O_3-ZrO_2 composite powder compact showed a duplex sintering behavior. The first stage of densification started between 950 - 1130°C and continued up to 1200-1250^{o}C at an enhanced rate. The second stage of densification started between 1200-1250°C and continued till 1450°C or higher temperature at a slower rate.

Shi et. al. [5.20] had also reported the similar duplex sintering behaviour of ZTA composite containing 15 or higher mole% Al_2O_3. The shrinkage was reported to be small for composites containing more than 45 mole% Al_2O_3 and it was higher at lower Al_2O_3 content. Among all the different types powder processing route studied in the present inveatigation, precipitated washed powder exhibited the highest shrinkage (21%) at 1450°C followed precipitation route and gelation route.

The observed shrinkage range for different powder correlated well with the agglomerate size and agglomerate strength of the starting powder and the powder having hard and larger agglomerate size ended up with a smaller shrinkage during sintering process. Tables 5.3, 5.5 and 5.7 showed that the agglomerate strength were 134, 126 and 99 MPa and agglomerate size were 35, 30 and 19 μm for gelation, precipitation and precipitated washed routes respectively. The lower agglomerate strength and smaller agglomerate size of precipitated washed powder produced higher shrinkage in the compacts. The shrinkage was found to increase rapidly in the temperature range 950 - 1250°C, thereafter the shrinkage slope changed and shrinkage increment continued at slower rate till 1450°C and above. The slope change in temperature range 1250-1300°C could be either due to $m \rightarrow t$ ZrO_2 phase transformation and/or to the γ to α-Al_2O_3 phase transformation (both the effects are expected to take place in the said temperature region). In order to substantiate the exact phenomena responsible for the observed duplex densification behavior, the densification behavior of the pure Al_2O_3 and ZrO_2 powder prepared by precipitation washed route was also studied.

The sintering behaviour of pure ZrO_2 (Fig.5.46) shows a single stage densification behavior, where as the Al_2O_3 powder showed a double stage densification behavior similar to that of the composite powder with the onset of the second stage occurring around 1270°C. Thus the duplex densification is due to the $\gamma \rightarrow \alpha$ Al_2O_3 phase transition.

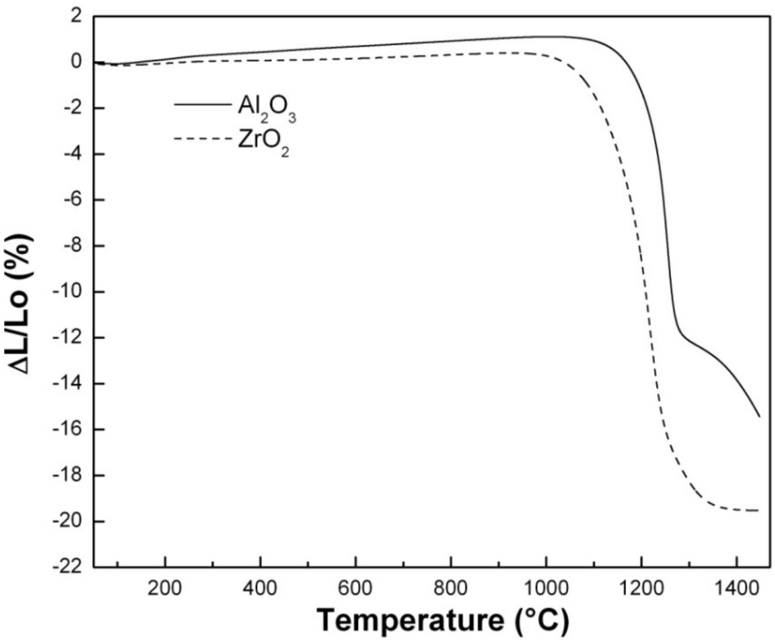

Fig.5.46. Dilatometric curves for Al_2O_3 and ZrO_2

The observed low temperature (1250°C) $\gamma \rightarrow \alpha$ Al_2O_3 phase transition in the Al_2O_3-ZrO_2 composite compacts may be due to the presence of ZrO_2 in the composite powder which reduces of the transformation temperature by 20°C.

5.6.2 Effect of precursors on densification behavior of Al_2O_3-ZrO_2 composite

The effect of precursors on densification behavior could be seen from Fig. 5.47. The samples have been prepared following precipitation and washing technique. Curve *A* shows the densification behavior of the compact prepared using $AlCl_3$ and $ZrOCl_2$ precursors and curve *B* is that prepared with $Al(NO_3)_3$ and $ZrOCl_2$. It could be seen from the figure that curve *B* has a higher shrinkage. Entrapped gases (caused by some volatile materials) at the sintering temperature affect the end point densities [5.21]. Scott and Reed [5.12] also reported that the presence of residual chlorine in the ZrO_2 powders (made by the chloride process) is detrimental to the sintering of ZrO_2 powders. The result of simultaneous DSC/TG analysis on the chloride precursor derived powder is shown in Fig.5.21.The gradual weight loss in the high temperature above 1000°C is attributed to the loss of residual chlorides as well as to the removal of OH- from hydrated Al_2O_3 [5.22]. Although both the powders had $ZrOCl_2$ as one of the precursors, the amount of chloride ions (in the mixed nitrate chloride precursor derived samples) was partially reduced when $AlCl_3$ was replaced by $Al(NO_3)_3$.

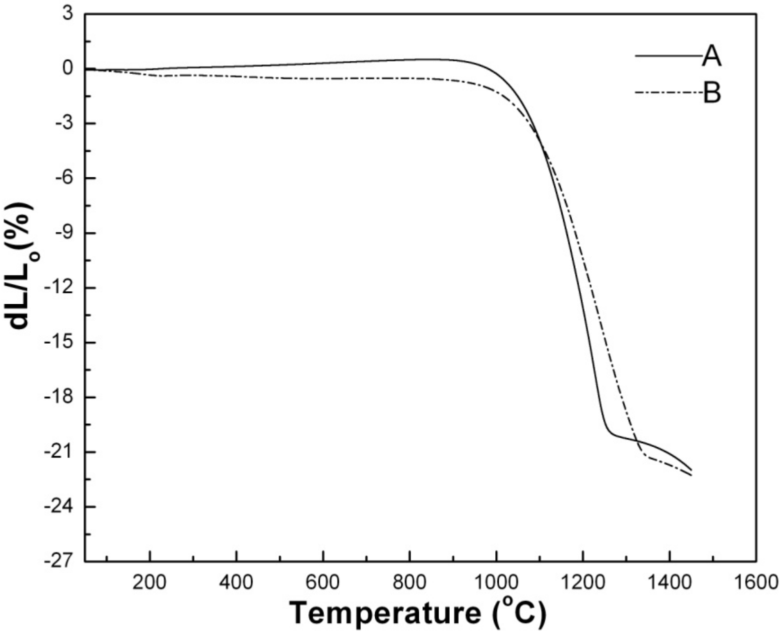

Fig.5.47. Non-isothermal densification behavior of Al_2O_3 - ZrO_2 composites prepared by different precursors

5.6.3 Effect of heating rate on densification behavior of Al_2O_3-ZrO_2 composite

The shrinkage behavior of green compacts as a function of sintering temperature and heating rate has been shown in Fig. 5.48. The onset of shrinkage was found to be independent of the heating rate. However, the temperature at which the maximum shrinkage rate was observed during first stage of sintering was found to be dependent on the heating rate and it shifted towards high temperature (1220 to 1253°C) with increase in heating rate (from 10 - 20°C /min). The maximum shrinkage rate was also found to increase with increase in heating rate during this stage.

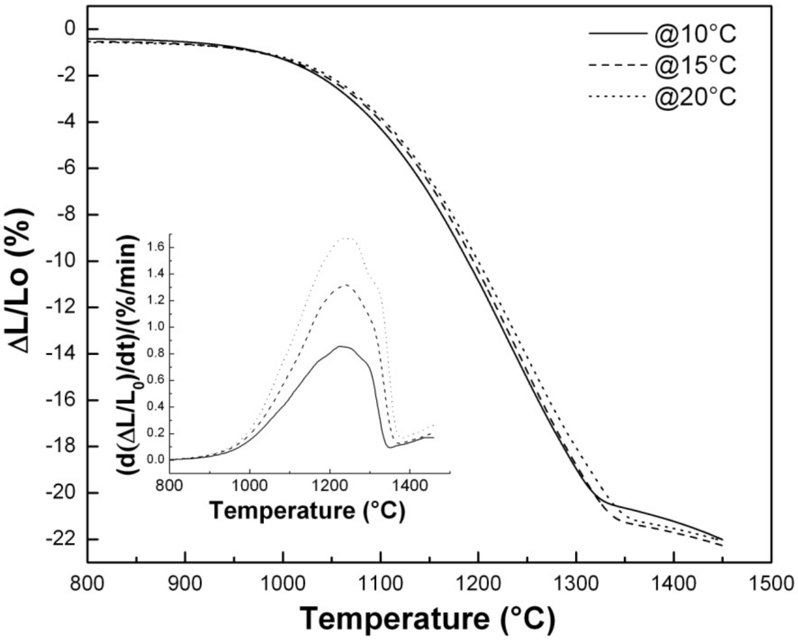

Fig.5.48. Dilatometric curves for Al_2O_3-ZrO_2 composites at different heating rates

.

5.6.4. Determination of sintering mechanism and activation energy - theoretical background

The generalized form of neck growth can be expressed from the two-sphere densification/sintering model [5.23, 5.24].

$$\left(\frac{X}{R_p}\right)^n = \frac{Bt}{R_p^m} \qquad (5.10)$$

where, X is the neck radius, R_p is the particle radius, t is the time, m and n are constants and the value of m and n depended on the kinetic mechanism of the initial stage of sintering, $B = B_0 T^a$, where B_0 corresponds to the combined material and numerical constants and is related to the temperature (T) through the Arrhenius law. The exponent n (kinetic constant) of Eqn. (5.10) identifies the sintering mechanism. The value of n for different mechanism and the corresponding values of the temperature exponent 'a' have been given in Table 5.11.

The neck growth and the shrinkage for the densification can be correlated by Eqn. (5.11), where, L_0 is the initial dimension of the green compact and ΔL is the shrinkage at time t.

$$\frac{\Delta L}{L_0} = \left(\frac{X}{2R_p}\right)^2 \tag{5.11}$$

Equation (5.10) and (5.11) can be combined to yield Eqn. (5.12)

$$\frac{\Delta L}{L_o} = \left(\frac{B_o T^a t}{2^n R_p{}^m}\right)^{2/n} \tag{5.12}$$

and this describes the densification behavior for isothermal conditions.

***Table 5.11 Dependence of frequency factor with temperature corresponding to the kinetics models used in literature* [5.24]**

Kinetic Model	*a*	*n*
Viscous flow	0	2
Plastic flow	-1	2
Volume diffusion	-1	5
Grain boundary diffusion	-1	6
Evaporation condensation	-3/2	3
Surface diffusion	-1	7

The time derivative of Eqn. (5.12) is

$$\begin{aligned}\frac{d(\Delta L/L_0)}{dt} &= \frac{d}{dt}\left[\frac{B_o T^a t}{2^n R_p{}^m}\right]^{2/n} \\ &= k\left(\frac{\Delta L}{L_0}\right)^{1-n/2}\end{aligned} \tag{5.13}$$

where, $k = B_0 T^a / 2^{n-1} n R_p{}^m$. B_0 can be expressed by the Arrhenius type relationship

$$k = Ae^{-Q/RT} \tag{5.14}$$

where, Q is the activation energy and $A = A_0 T^a$. The pre-exponential factor (A) of the Arrhenius equation is dependent on the exponent 'a' describing the dependence with the absolute temperature T. Substitution of Eqn. (5.14) into eqn. (5.13) results in the following equation.

$$\frac{d(\Delta L/L_0)}{dt} = A_0 T^a e^{-Q/RT}\left(\frac{\Delta L}{L_0}\right)^{1-n/2} \tag{5.15}$$

Equation (5.15) describes the time rate of shrinkage ($\Delta L/L_0$) at a certain temperature and gives the generalized expression applicable for both isothermal and non-isothermal densification condition [5.25-5.27]. Thus, any set of data $d(\Delta L/L_0)/dt$ - T- $\Delta L/L_0$ should fit Eqn. (5.15) independent of the experimental conditions (i.e., isothermal, non-isothermal conditions).

The dilatometric curve obtained from a linear-heating rate ($\beta = dT/dt$), i.e., non-isothermal condition can be described by the Eqn. (5.17) (which is obtained by integrating (5.16) followed by rearrangement).

$$T^2\left(\frac{d(\Delta L/L_0)}{dt}\right) = \frac{2\beta Q}{nR}\left(\frac{\Delta L}{L_0}\right) \tag{5.16}$$

The sintering activation energy and the mechanism of densification can be determined from the value of the Q and n respectively. The linear plot of $T^2\left(\frac{d(\Delta L/L_0)}{dt}\right)$ vs $\left(\frac{\Delta L}{L_0}\right)$ as a function of heating gives an idea of $\left(\frac{Q}{n}\right)$ ratio; however, the individual value is difficult to determine. In order to find the densification mechanism and densification activation energy, one needs to know the value of either Q or n. The simultaneous determination of Q and n is only possible using the modified eqn. (5.15).

Freeman and Carroll [5.28] proposed that the sintering kinetics could be determined from a single CRH curve by modifying the Eqn. (5.15).

The differentiation of the logarithmic form of Eqn. (5.15) with respect to $d\ln(\Delta L/L_0)$ gives

$$\frac{d\ln\frac{d(\Delta L/L_0)}{dt}}{d\ln(\Delta L/L_0)} - a\left(\frac{d\ln T}{d\ln(\Delta L/L_0)}\right) = -\left(\frac{Q[d(1/T)]}{R[d\ln(\Delta L/L_0)]}\right) + 1 - \frac{n}{2} \tag{5.17}$$

or

$$\frac{\Delta\ln\frac{d(\Delta L/L_0)}{dt}}{\Delta\ln(\Delta L/L_0)} - a\left(\frac{\Delta\ln T}{\Delta\ln(\Delta L/L_0)}\right) = -\left(\frac{Q[\Delta(1/T)]}{R[\Delta\ln(\Delta L/L_0)]}\right) + 1 - \frac{n}{2} \tag{5.18}$$

For a fixed value of '*a*', the plot of LHS of Eqn. (5.17) or (5.18) against $\mathrm{d}(1/T)/\mathrm{d}\ \ln(\Delta L/L_0)$ or $\Delta(1/T)/\Delta\ln(\Delta L/L_0)$ respectively, yields a straight line whose slope is Q/R and $(1\text{-}n/2)$ is the intercept. The straight line thus obtained gives Q/R *as* slope and $(1\text{-}n/2)$ as the intercept. Thus, Q and n can be simultaneously determined from this model (Eqn. (5.17) or (5.18)) using a single dilatometric curve. However, the parameter 'a' is to be assumed from the Table-10 for fitting into these equations.

5.6.5 Determination of initial stage sintering kinetic parameter from CRH sintering

The kinetic analysis of initial stage sintering is limited to the fractional shrinkage ≤ 3 %, implying densification without grain growth. The initial stage sintering kinetics for Al_2O_3-ZrO_2 composites for different heating rates has been analyzed from dilatometric studies using Eqn. (5.16). The shrinkage data ($\Delta L/L_0$ ≤ 3 %) has been obtained from the nonisothermal sintering curve at different heating rate (Fig.5.48). The shrinkage rate has been calculated from the fitted time dependent shrinkage curve using numerical differentiation. The graph of $T^2\left(\frac{d(\Delta L/L_O)}{dt}\right)$ vs $\left(\frac{\Delta L}{L_O}\right)$ as a function of heating rates yields a straight line (Fig.5.49). The *'a'* parameter has been assumed to be -1 as the viscous flow (a = *0*) and evaporation and condensation (a = *-1.5*) are forbidden mechanism for densification in Al_2O_3- ZrO_2 composites. The slope, r (regression coefficient) and hence Q/n value calculated from the fitted equation has been tabulated in Table 5.12. The Q/n value has been found to be independent of the heating rate. Although it yields consistent values of Q/n ratio but the value of both Q and n cannot be determined simultaneously from the fitted eqn. (5.17).

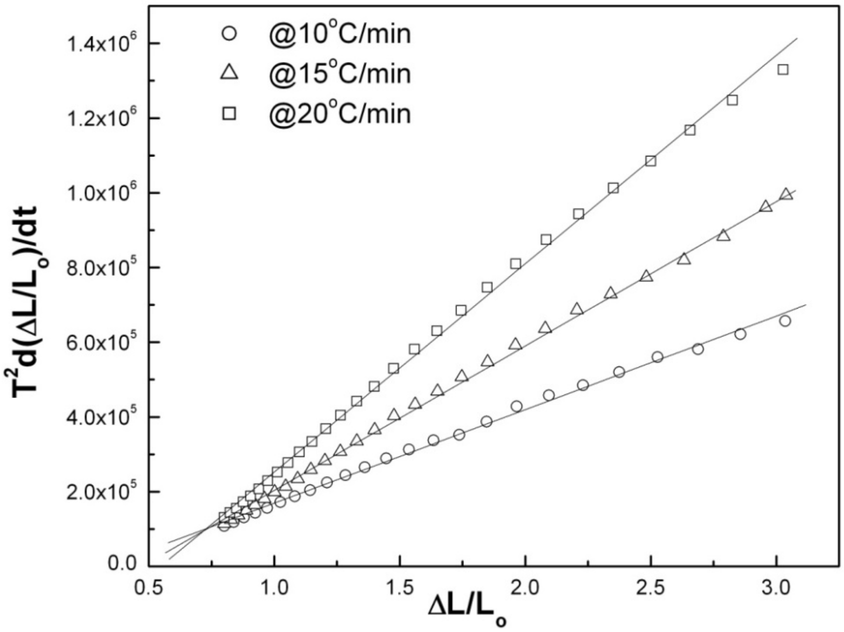

Fig.5.49. Analysis of the dilatometric curve (constant rate heating sintering) of Al_2O_3-ZrO_2 composites obtained at different heating rates using eqn. (5.16).

Table 5.12 The slopes and Q/n from the Fig.5.46 using Eqn. (5.16)

Rate (β) *°C/min*	Slope= $\frac{2\beta Q}{nR}$	r	$\frac{Q}{n}$
10	113273	0.998	47089
15	179136	0.999	49647
20	237609	0.999	49389

5.6.6 Determination initial stage sintering kinetic parameter from isothermal densification behaviour

The isothermal shrinkage behavior of the Al_2O_3-ZrO_2 composite has also studied in order to confirm the validity of the diffusion mechanisms. The sintering rate equation during isothermal sintering (initial stage) is given by.

$$\frac{\Delta L}{L_0} = \left(\frac{B_0 T^a t}{2^n R_p^m}\right)^{2/n} = At^{2/n} \qquad (5.12)$$

The logarithms of eqn. (5.13) yields

$$\log\left(\frac{\Delta L}{L_0}\right) = \log A + \frac{2}{n}\log t \tag{5.19}$$

Eqn. (5.19) is applicable for fractional shrinkage < 3%, a condition which satisfies the initial stage of sintering.

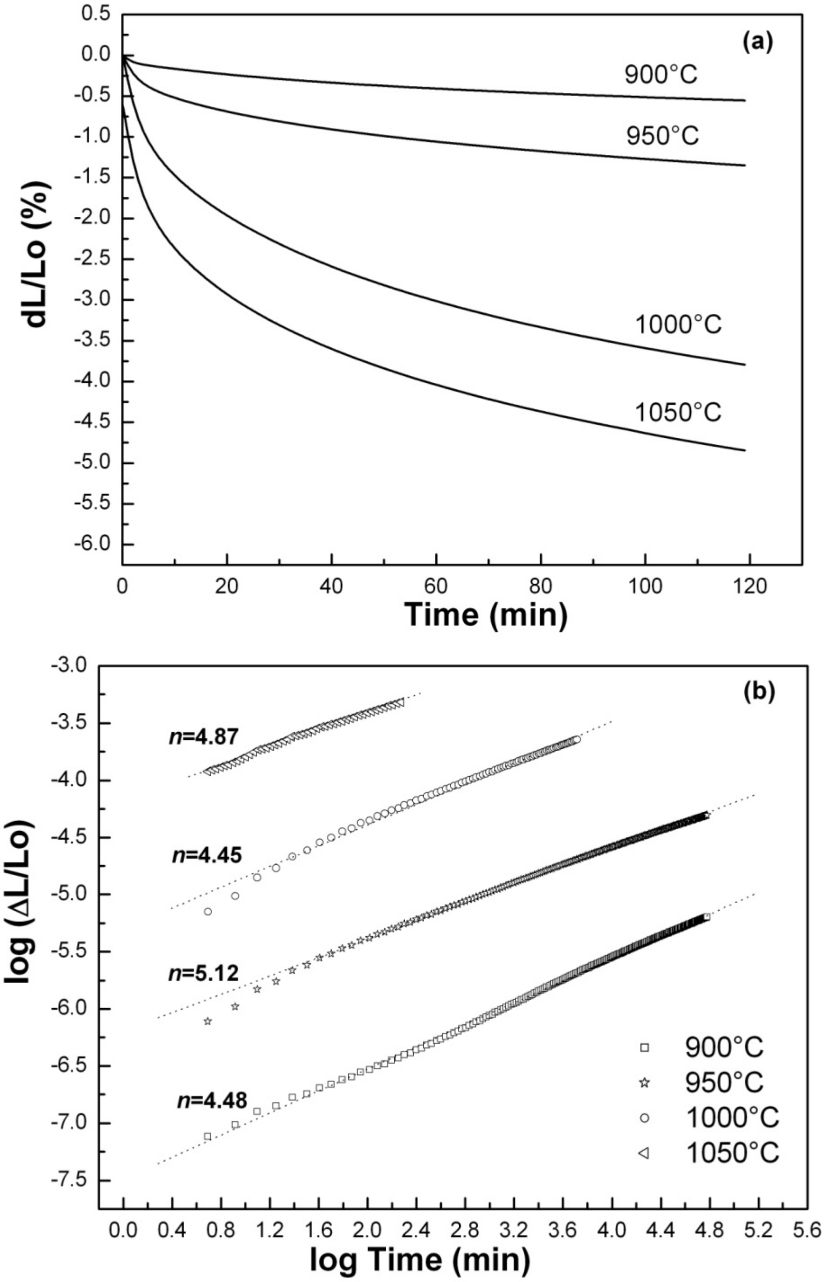

Fig.5.50. Isothermal densification behaviour of Al_2O_3-ZrO_2 composites (a) Isothermal dilatometric curve (b) analysis of isothermal curve using Eqn.5.19.

Figure 5.50 (a) shows the change in shrinkage with holding time of isothermal sintering in the temperature ranges 900 to 1050°C with an 50°C interval. The isothermal shrinkage data obtained from the isothermal study has been plotted in Fig.5.50 (b) following Eqn. (5.19). The kinetic parameter '*n*' value was determined from the slope of the fitted straight line. The value n varied between 4.45- 5.12 for different temperature. According to Table 5.11, n = 5 indicate that the densification is governed by volume diffusion. Thus, the activation energy for densification could be calculated from the Q/n ratio obtained by analyzing the constant rate heating sintering dilatometric curves

5.6.7 Simultaneous determination of initial stage sintering kinetic parameter from constant rate heating sintering dilatometric data

Figure 5.51 shows the plot of LHS of Eqn. (5.17) for a = -1 as a function of $\Delta(1/T)/\Delta\ln(\Delta L/L_0)$.The slope (Q/R) at different heating rate and intercept $(1- n/2)$ thus obtained is given in Table 5.12.

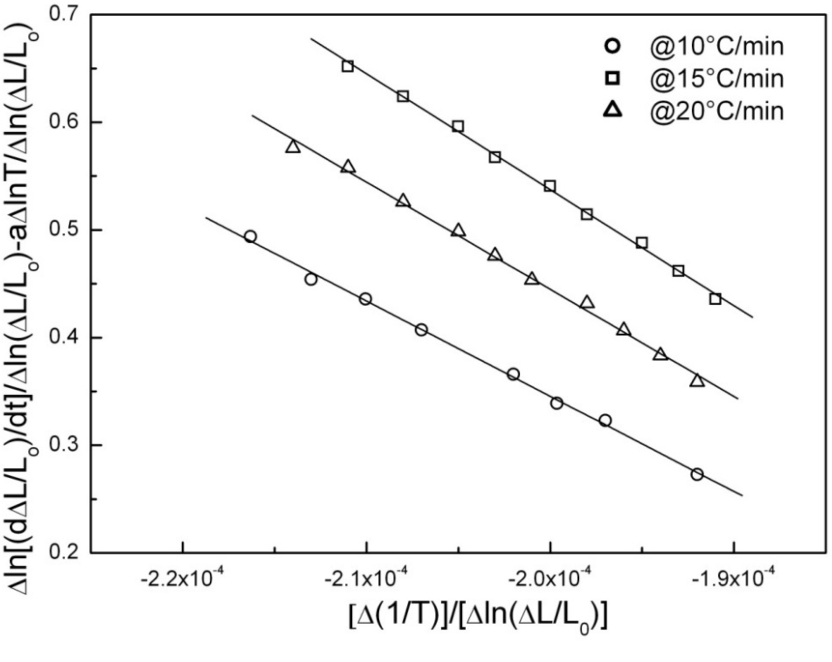

Fig.5.51. Analysis of the dilatometric curve (constant rate heating sintering) of Al_2O_3-ZrO_2 composites obtained at different heating rates using Eqn. 5.17.

According to Table 5.12, the ratios of Q/n as well as n were very close to the calculated (Q/n) (obtained using Eqn.5.16). The value of n varied between 5.02 and 5.22 thereby confirming that volume diffusion is the dominant sintering mechanism (as per Table 5.12).

Table 5.13 The value of slope, intercept and Q/n from the Fig.5.46 using Eqn. (5.21) at different heating rate for a = -1.

Heating Rate (β) °C/min	Slope=Q/R	r	n (calculated from intercept)	Q/n
10	30173	0.999	5.02	49974
15	30633	0.999	5.08	50138
20	30760	0.997	5.22	48994

Matsui [5.29] reported similar densification kinetics of ZrO_2 with 0.25 wt% Al_2O_3 addition. The densification rate increased with the addition of Al_2O_3 and the activation energy decreased as the kinetics changed from grain boundary diffusion (GBD) to volume diffusion (VD). The transformation of transition Al_2O_3 was not observed during the initial stage sintering temperature range. The activation energy Q thus calculated from Q/n ratio was found to vary between 236-258 kJ mol^{-1}.

5.6.8 Grain Growth Behavior of Al_2O_3-ZrO_2

The grain growth kinetics for normal grain growth obey a power-law relationship

$$G^N - G_0^N = Kt \qquad (5.20)$$

$$G^N = Kt \qquad G_0^N \ll G^N \qquad (5.21)$$

Where, G represents the grain size at time t, G_0 is the initial grain size at t = 0, K is a constant which depended on the temperature and the activation energy of grain growth, and N the grain growth exponent characterizing the growth mechanism. The grain size of both Al_2O_3 and ZrO_2 increased as the function of the sintering time increasing. The grain growth has almost parabolic behavior (Fig.5.52).The grain growth exponent N is calculated from the slope of the log (G) versus log (t) line plot, which is equal to $1/N$ which was given in Fig. 5.53.

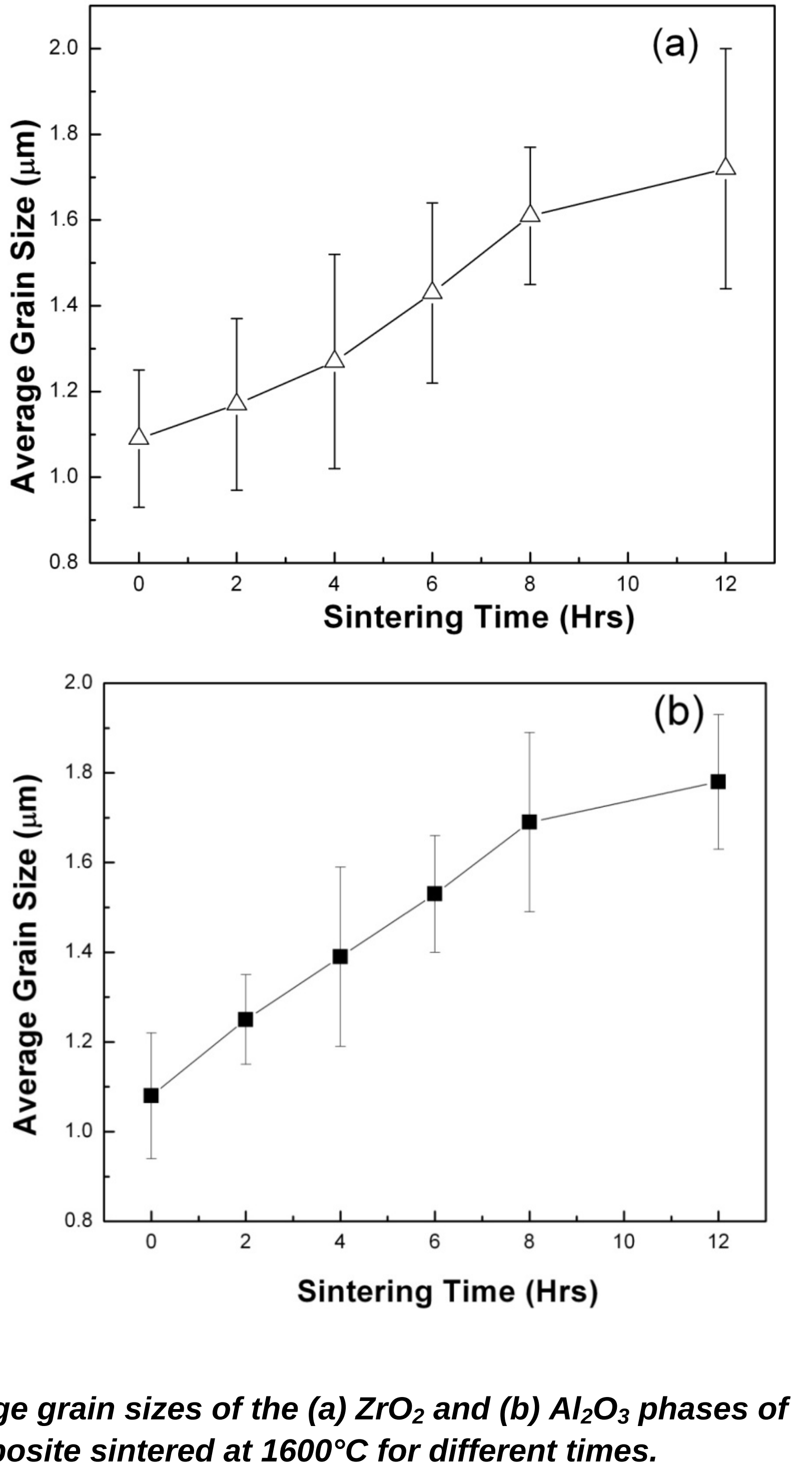

Fig.5.52. Average grain sizes of the (a) ZrO_2 and (b) Al_2O_3 phases of the composite sintered at 1600°C for different times.

The grain growth during sintering can be described by Eqn.5.21 [5.30].The grain growth exponent, N, for ZrO_2 and Al_2O_3 phase were 3.17 and 4.22, respectively, indicating that different mechanisms are responsible for grain growth of each phase.

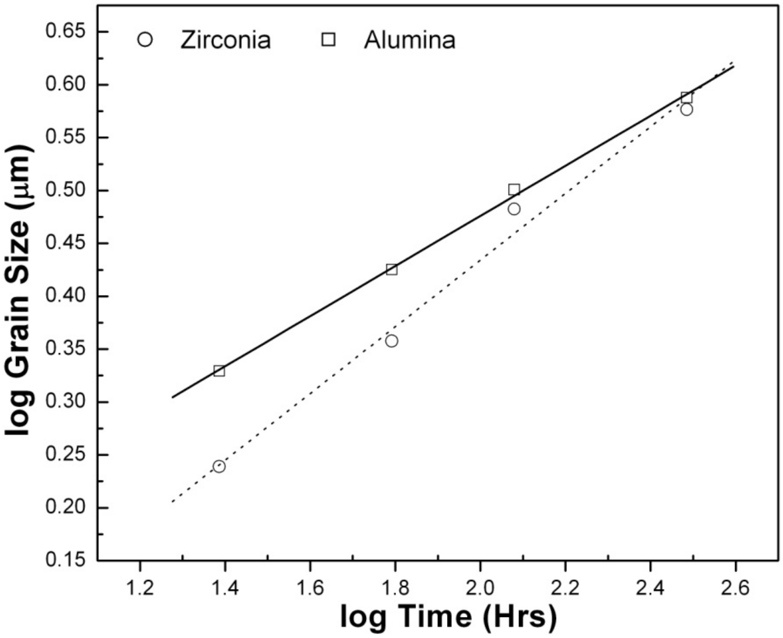

Fig.5.53. Log (grain size) vs. log (time) of ZrO_2 and Al_2O_3 sintered at 1600°C

A growth exponent of $N = 4$ indicates a grain boundary diffusion controlled process, while an exponent of $N = 3$ indicates a volume diffusion controlled process. The grain growth exponents for the ZrO_2 and Al_2O_3 found in this work are in agreement with the works of Alexander et al [5.30].

References

5.1. E. B. Amitin,Yu. A. Kovalevskaya, I. E. Paukov and K. S. Sukhovei, “Thermodynamic properties of ammonium halogenides near their tricritical points”, Journal of Engineering Physics and Thermophysics, 39,381-1384 (1980).

5.2. R. Venkatesh, S.R. Ramanan, “Effect of organic additives on the properties of sol–gel spun Al_2O_3 fibres”, J. Eur. Ceram. Soc. 20, 2543–2549 (2000).

5.3. R.P.Rana, S.K. Pratihar and S. Bhattacharyya, “Effect of powder treatment on the crystallization behaviour and phase evolution of Al_2O_3- high ZrO_2 nanocomposites”, J. Mat. Sci., 41, 7025–7032 (2006).

5.4. Q. Qu , L. Li , W. Bai, C. Yan and C. Cao, “Effects of NaCl and NH_4Cl on the initial atmospheric corrosion of zinc”, Corrosion Science, 47, 2832–2840 (2005).

5.5. C. LI, Y. Chen and T. Yen, “The effects of preparation method on the characteristics of Al_2O_3-ZrO_2 powders”, J. of Sol-Gel Sci. and Tech., 4, 205-215 (1995).

5.6. C. M. Phillippi and K. S. Mazdiyasini, “Infrared and Raman Spectra of ZrO_2 Polymorphs”, J. Am. Ceram. Soc., 54, 254-258 (1971).

5.7. J.L. Shi, B.S. Li, M.L. Ruan and T.S. Yen, “Processing of nano – Y- TZP/Al_2O_3 composite powder”, J. Eur. Ceram. Soc., 15, 959-965 (1995).

5.8. J.S. Hong, S.D. De La Torre, K. Miyamoto, H. Miyamoto and L. Gao, “Crystallization of Al_2O_3/ZrO_2 solid solution powder prepared by co-precipitation”, Mat. Letts., 37, 6-9 (1998).

5.9. R.A. Dimilia and J. S. Reed, **“**Stress transmission during the compaction of a spray-dried Al_2O_3 powder in a steel die”, J. Am. Ceram. Soc., 66, 667-672 (1983).

5.10. F. F. Lange, “Sinterability of agglomerated powders”, J. Am. Ceram. Soc., 67, 83-89 (1984).

5.11. H. K. Schmid, “Quantitative analysis of polymorphic mixes of ZrO_2 by X-ray diffraction”, J. Am. Ceram. Soc. 70, 367-376 (1987).

5.12. C.E. Scott and J. S. Reed, “Effect of laundering and milling on the sintering behavior of stabilized ZrO_2 powders”, Am. Ceram. Soc. Bull., 58, 587-590 (1979).

5.13. V. Saraswathi, G.V.N. Rao and G.V. Rama Rao, “Structural evolution in Al_2O_3 gel”, J. Mater. Sci. ,22, 2529–2534 (1987).

5.14. I.Levin and D.Brandon, “Metastable Al_2O_3 polymorphs: crystal structure and transition sequences”, J. Am. Ceram. Soc. 81, 1995-2012 (1998).

5.15. R C Garvie, “Stabilization of the tetragonal structure in ZrO_2 microcrystals”, J Phy. Chem, 2, 218-223 (1978).

5.16. Zárate, G. Rosas and R. Pérez,n “Structural transformations of the Pseudoboehmite to α-Al_2O_3” Journal of Material Online,172, 1-11 (2005).

5.17. G Y Guo and Y L Chen, “High quality ZrO_2 powder resulting from the attempted separation of acetic acid from acrylic acid with zirconium oxychloride”, J Mat. Chem., 11, 1283-1287 (2001).

5.18. S G Chen, Y S Yin and D P Wang, “Experimental and theoretical investigation on the correlation between aqueous precursors structure and crystalline phases of ZrO_2”, J Molecular Structure, 690, 181-187 (2004).

5.19. R.P.Rana, S.K.Pratihar and S. Bhattacharyya, “Powder processing route and densification behaviour of Al_2O_3 – high ZrO_2 composites using chloride precursors”, J. Mat. Pro. Tech., 190, 350-357(2007).

5.20. J.L. Shi, J.H. Gao, B. S. Li and T.S Yen, et al., Processing of nano-Y-TZP/Al_2O_3 composites II: compaction and sintering behaviour of nano-Y-TZP/ Al_2O_3 composite powders, J. Euro. Ceram. Soc.15, 967-973 (1995).

5.21. D.H. Kim and C. H. Kim, “Entrapped gas effect in the fast firing of Y_2O_3-doped ZrO_2”, J. Am. Ceram. Soc., 75, 716-18 (1992).

5.22. D. Sarkar, “Synthesis and Thermo – Mechanical Properties of Sol – Gel Derived ZrO_2 Toughened Al_2O_3 Nanocomposite”, Ph.D. Thesis, N.I.T, Rourkela, 2007.

5.23. M. Rahaman, “Ceramic Processing and Sintering”. Marcel Dekker, New York, 1995.

5.24. R. German, “Powder Metallurgy Science” Metal Powder Industries Federation, Princeton, NJ, 1984.

5.25. M. Brown, D. Dolimore, and A. Galwey, “Reactions in the Solid State in Comprehensive Chemical Kinetics”. Elsevier, Amsterdam, Netherlands, 1980.

5.26. A. Galwey and M. Brown, “Thermal Decomposition of Ionic Solids”. Elsevier, Amsterdam, Netherlands, 1999.

5.27. F. Gotor, J. Criado, J. Malek, and N. Koga, “Kinetic Analysis of Solid-State Reactions: The Universality of Master Plots for Analyzing Isothermal and Nonisothermal Experiments”, J. Phys. Chem., 104, 777–782 (2000).

5.28. E.S. Freeman and B. Carrol, “Application of Thermo analytical Techniques to Reaction Kinetics: Thermogravimetric Evaluation of Decomposition of Calcium Oxalate Monohydrate,” J. Phys. Chem., 62, 397-394 (1958).

5.29. K. Matsui, N. Ohmichi and M. Ohgai, “Sintering kinetics at constant rates of heating: Effect of Al_2O_3 on the Initial sintering stage of fine ZrO_2 powder”, J. Am. Ceram. Soc., 88, 3346–3352 (2005).

5.30. K. B. Alexander, P. F. Becher, S.B. Waters, and A. Bleier, “Grain growth kinetics in Al_2O_3-ZrO_2 (Ce-ZTA) composites”, J. Am. Ceram. Soc., 77, 939-946 (1994).

Chapter VI

Results and discussion- Al_2O_3-Y-ZrO_2 Composites

6.1. Flexural Strength

The effect of Y_2O_3 content on the flexural strength of Al_2O_3-Y-ZrO_2 composites is shown in Fig. 6.1.

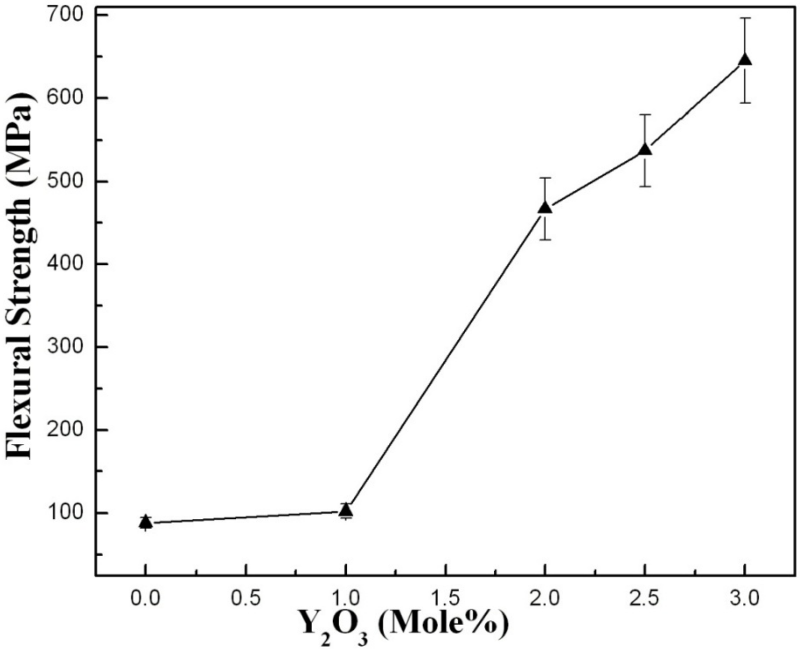

Fig.6.1. Effect of Y_2O_3 addition on flexural strength of Al_2O_3-Y-ZrO_2 composites

The strength gradually increases with Y_2O_3 addition till 1.0 mol% Y_2O_3 (102 MPa) followed by a rapid increase for 2, 2.5, and 3 mol% Y_2O_3 compositions which are 467, 537 and 645 MPa respectively. The low density till 1.0 mol% Y_2O_3 addition probably causes a spontaneous microcracking of the samples. In Al_2O_3-1Y-ZrO_2 composites, the sintered density at 1600°C is 94.5% and retained *t*-ZrO_2 is 10%. For Al_2O_3-2Y-ZrO_2 composites, under similar sintering conditions, the density is 95.4% and *t*-ZrO_2 retention is 16.4%. In both these composites, the combined effect of lower Y_2O_3 and lower sintered density resulted in poor *t* -ZrO_2 retention. This causes a spontaneous $t \rightarrow m$ ZrO_2 transformation giving a microcracked microstructure.

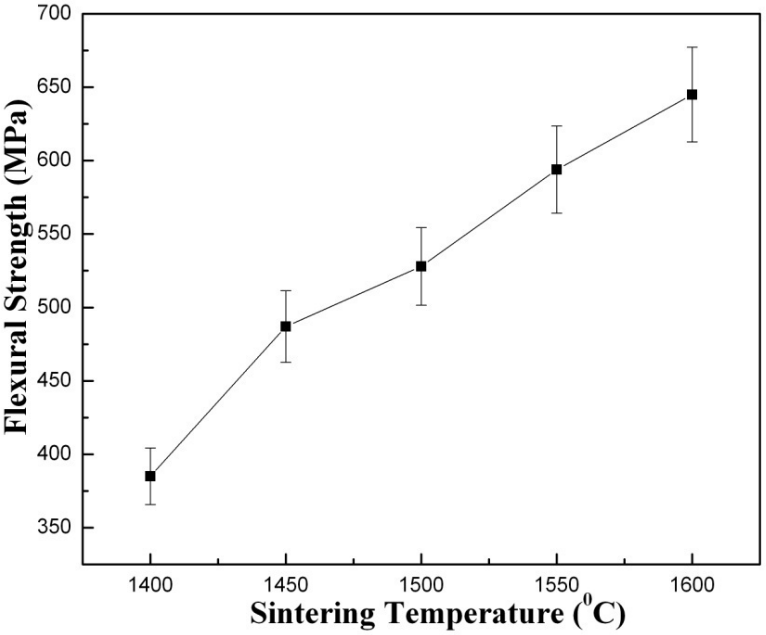

Fig.6.2. Effect of sintering temperature on flexural strength of Al_2O_3-3Y-ZrO_2 composites

For any brittle ceramics, the fracture strength is controlled by the size of the largest flaw (controlled by the largest flaw size). The fracture toughness and fracture toughness (K_{IC}) and fracture strength (σ_f) are related by the following Eqn. 6.1.

$$K_{IC} = Y\sigma_f c^{1/2} \quad (6.1)$$

where, Y is a shape related geometrical factor (constant for all the compositions) and c is the half flaw size of the most critical flaw from which fracture initiates. Therefore, for any particular composition if K_{IC} and σ_f are experimentally known then the relative value of half critical flaw size can be computed. The normalized critical flaw size for Al_2O_3-Y-ZrO_2 (Y = 1, 2, 2.5 and 3 mol%) are tabulated in Table 6.1 and 6.2 using the data of three point bending strength (σ_f) as well as biaxial flexural strength (σ_r) respectively.

The Tables 6.1 and 6.2 show that the normalized flaw size variation is very small for Al_2O_3-Y-ZrO_2 composites with Y = 2, 2.5 and 3 mol%. However, in Al_2O_3-1Y-ZrO_2 the flaw size is large (by an order of magnitude for three point bend test and by three times for biaxial flexural strength) as compared to other compositions.

Thus, it is proposed that in Al_2O_3-1Y-ZrO_2 composite the large flaws appear to be partially responsible for low strength in this composition. However, in Al_2O_3-Y-ZrO_2 composites with Y = 2, 2.5 and 3 mol%, flaw size appear to have less effect on the final strength.

Table 6.1 Normalized critical flaw size (Y^2c) of Al_2O_3-Y-ZrO_2 sintered composites (three point bending strength)

Compositions	*Three point bending strength (σ_f) (MPa)*	*Fracture Toughness (K_{IC}) (MPa $\sqrt{m}$)*	*Normalized Y^2c*
Al_2O_3-1Y-ZrO_2	102	5.68	3.02×10^{-3}
Al_2O_3-2Y-ZrO_2	467	8.45	3.27×10^{-4}
Al_2O_3-2.5Y-ZrO_2	537	9.46	2.97×10^{-4}
Al_2O_3-3Y-ZrO_2	640	13.04	4.38×10^{-4}

Table 6.2 Normalized critical flaw size (Y^2c) of Al_2O_3-Y-ZrO_2 sintered composites (biaxial flexural strength)

Compositions	*Biaxial flexural strength (σ_r) (MPa)*	*Fracture Toughness (K_{IC}) (MPa $\sqrt{m}$)*	*Normalized Y^2c*
Al_2O_3-1Y-ZrO_2	102	5.68	3.1×10^{-3}
Al_2O_3-2Y-ZrO_2	190	8.45	1.97×10^{-3}
Al_2O_3-2.5Y-ZrO_2	264	9.46	1.28×10^{-3}
Al_2O_3-3Y-ZrO_2	335	13.04	1.51×10^{-3}

.

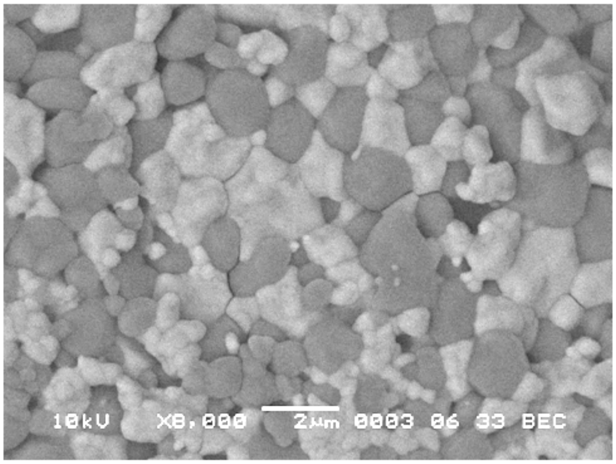

Fig. 6.3. SEM microstructure of Al_2O_3-1Y-ZrO_2 composites

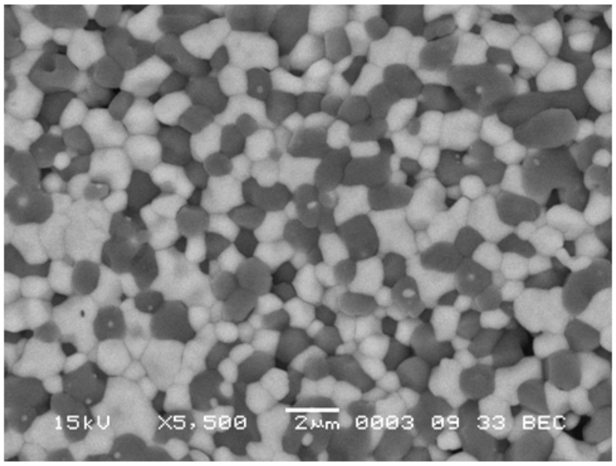

Fig. 6.4. SEM microstructure of Al_2O_3-2Y-ZrO_2 composites

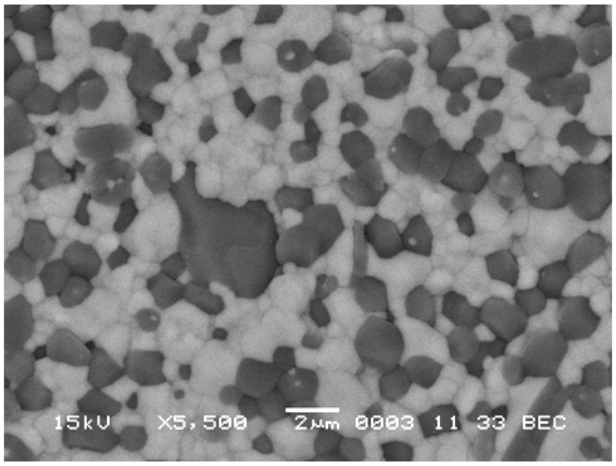

Fig. 6.5. SEM microstructure of Al_2O_3-2.5Y-ZrO_2 composites

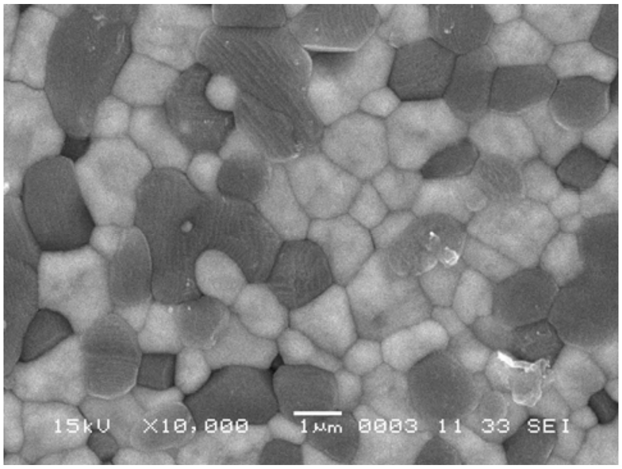

Fig. 6.6. SEM microstructure of Al_2O_3-3Y-ZrO_2 composites

At higher Y_2O_3, not only the retention of *t*-ZrO_2 was higher, but also the sintered density was also high as well as the grain sizes were also finer. In Al_2O_3-Y-TZP composite the t-ZrO_2 retention among other factors, is also critically dependent on the mole fraction of Y_2O_3, its distribution within the ZrO_2 grains and not only on grain size alone. It has been observed and reported by many that the stabilizer distribution in ZrO_2 varies from grain to grain and also within a grain and this distribution of stabilizer content gives rise to different degree of stabilization of different grains as well as different level of transformability. Thus it is quite possible that some of the grains of Al_2O_3-1Y-TZP composite had lower amount of Y_2O_3 than required for stabilization and some of these grains possibly have transformed to *m*-ZrO_2 during cooling. Thus in spite of having lower grain size and some grains possibly have transformed to m-ZrO_2 during cooling and *t*-ZrO_2 retention was less in Al_2O_3-1Y-TZP composition. All this combined effect gave rise to higher strength. The inter dependence of strength and sintered density becomes more clear on comparing relative density and flexure strength as a function of sintering temperature. Both the graphs exhibit an increasing strength thereby suggesting that the fracture strength of Al_2O_3-Y-ZrO_2 composites is controlled by sintered density (or in the other words residual flaw size). Since the flaw size in dense composites (composition 2, 2.5 and 3Y) is small and nearly constant, the strength appears to be independent of flaw size and is controlled by transformation toughening.

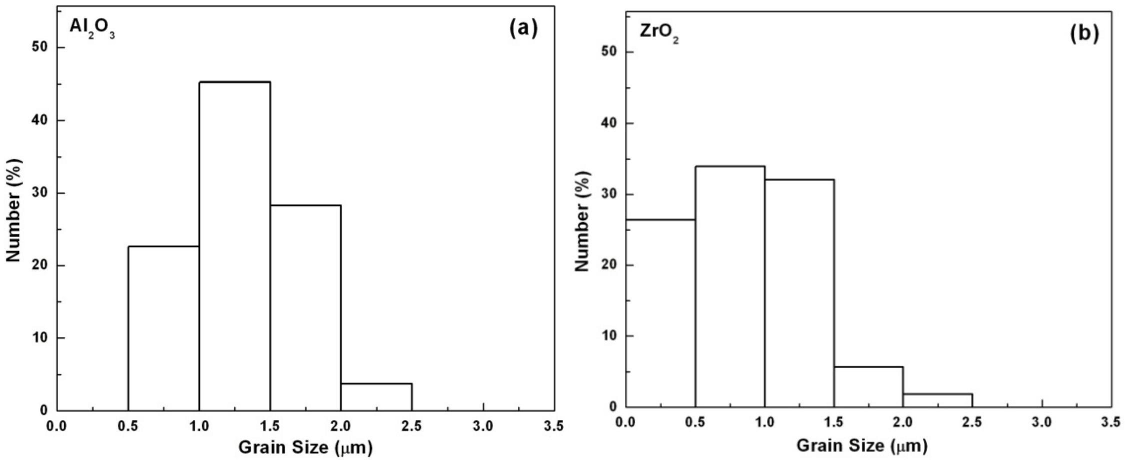

Fig. 6.7 Grain size distribution of Al_2O_3-1Y-ZrO_2 sintered (1600^oC) composites

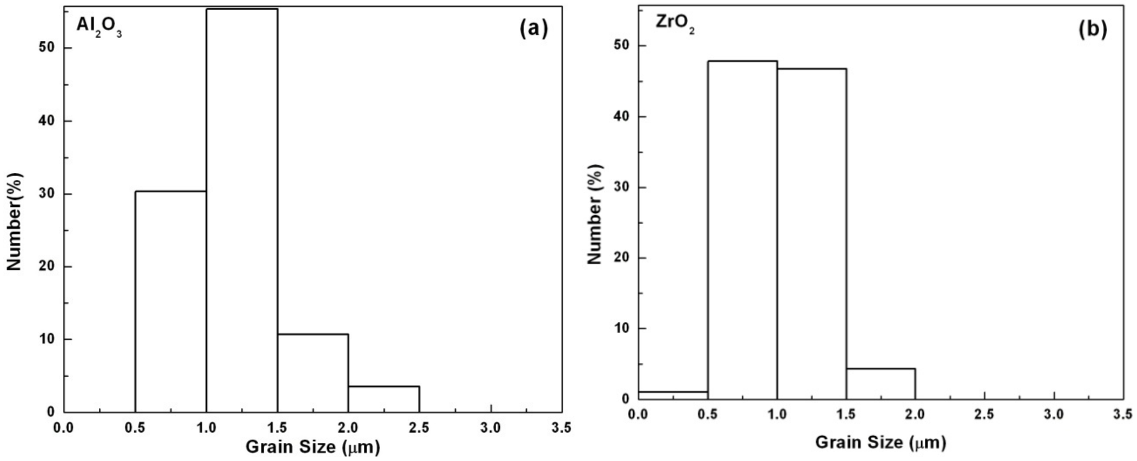

Fig.6.8. Grain size distribution of Al_2O_3-2Y-ZrO_2 sintered (1600^oC) composites

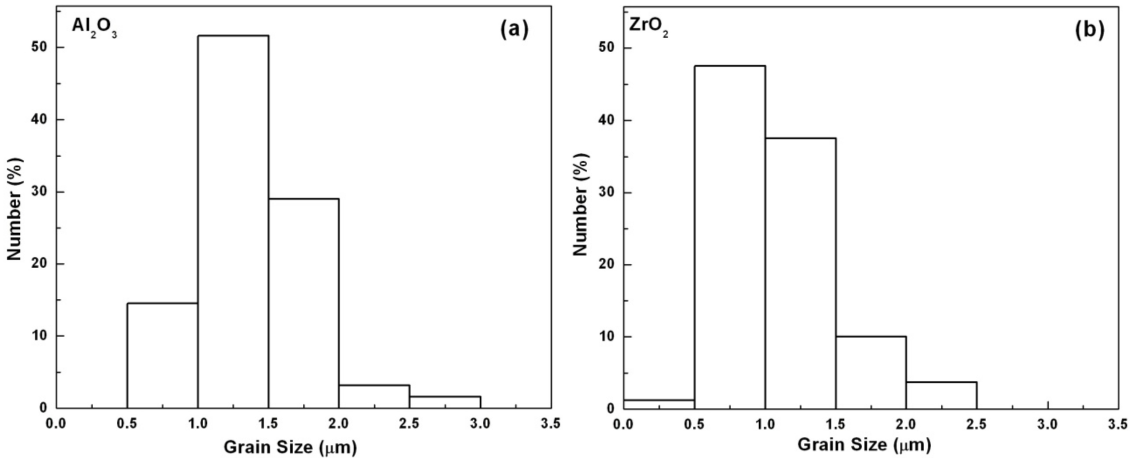

Fig.6.9. Grain size distribution of Al_2O_3-2.5Y-ZrO_2 sintered (1600^oC) composites

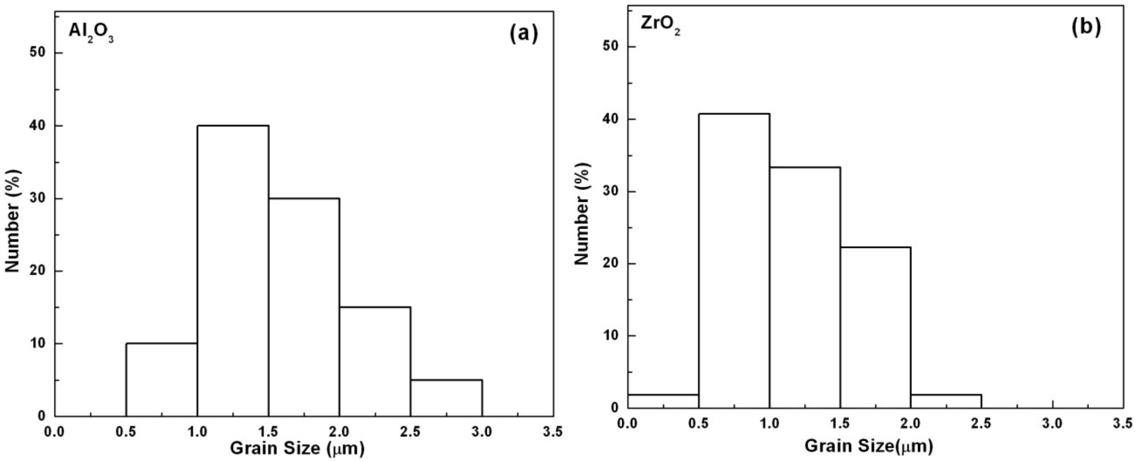

Fig.6.10. Grain size distribution of Al_2O_3-3Y-ZrO_2 sintered (1600°C) composites

The grain size variations (separately for Al_2O_3 and ZrO_2) are shown in Fig. 6.7-6.10. The grain size distribution of Al_2O_3 and ZrO_2 for all Al_2O_3-Y-ZrO_2 compositions. The distribution shows that the grain size did not vary much with compositions and majority of the grains were between 1-2.5 μm. Thus it appears that the grain size did not affect the strength in a significant way.

6.2 Biaxial Flexural Strength

The biaxial flexural strength of the composite as a function of Y_2O_3 content is shown in Fig. 6.11.

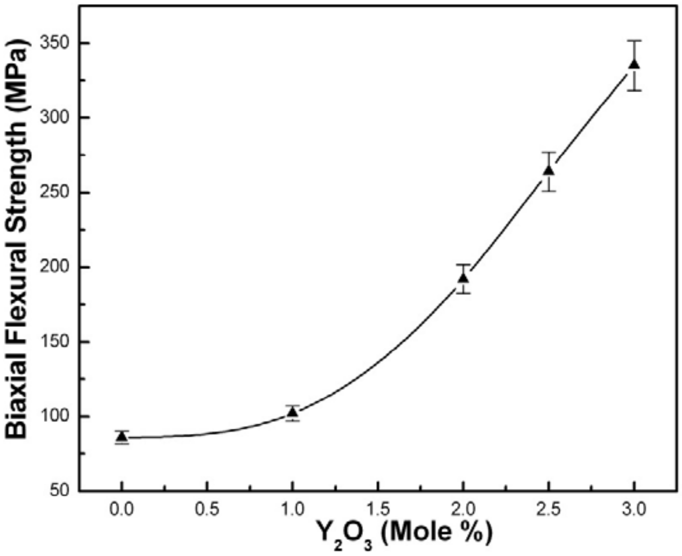

Fig.6.11. Biaxial flexural strength of Al_2O_3-Y-ZrO_2 composites as a function of Y_2O_3 content

The biaxial flexural strength values show similar trend to that observed for three point bend strength. Highest strength is 345 MPa for Al_2O_3-3Y-ZrO_2 composites sintered at 1600°C.

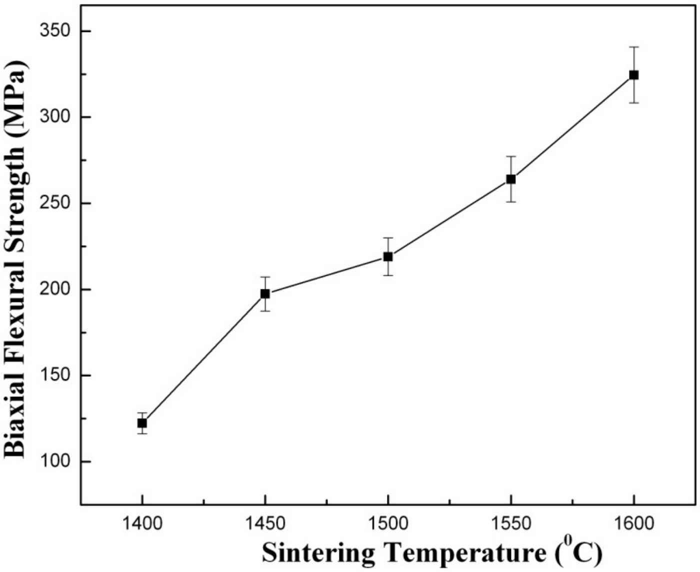

***Fig.6.12. Biaxial flexural strength of Al_2O_3-3Y-ZrO_2 composites as a function of* sintering temperature**

Figure 6.12 shows the strength of Al_2O_3- 3Y-ZrO_2 composites as a function of sintering temperature. The low strength value at lower sintering temperature (<1600°C) is due to incomplete densification. However, the strength values are lower in this mode (in comparison to three point bend strength) because mixed mode fracture (Mode I and Mode II) take place in these cases. Thus tensile strength required to initiate crack propagation is lower in this case leading to lower strength.

6.3 Fracture Toughness of Al_2O_3-Y-ZrO_2 Composites

The SENB fracture toughness as a function of Y_2O_3 content is shown in Fig. 6.13 for samples sintered at 1600°C. The fracture toughness increases with Y_2O_3 content at first gradually (1.8 MPa√m to 5.5 MPa√m) till 1 mol% Y_2O_3 followed by rather rapid increase to 8.5 MPa√m at 2 mol% Y_2O_3 which further increases to 9 MPa√m at 2.5 mol% Y_2O_3. Thereafter, the fracture toughness steeply rises to 13.04 MPa√m at 3 mol% Y_2O_3 addition. The fracture toughness as a function of sintering temperature could not be determined because at lower sintering temperatures the composites did not attain the required density for toughness measurement.

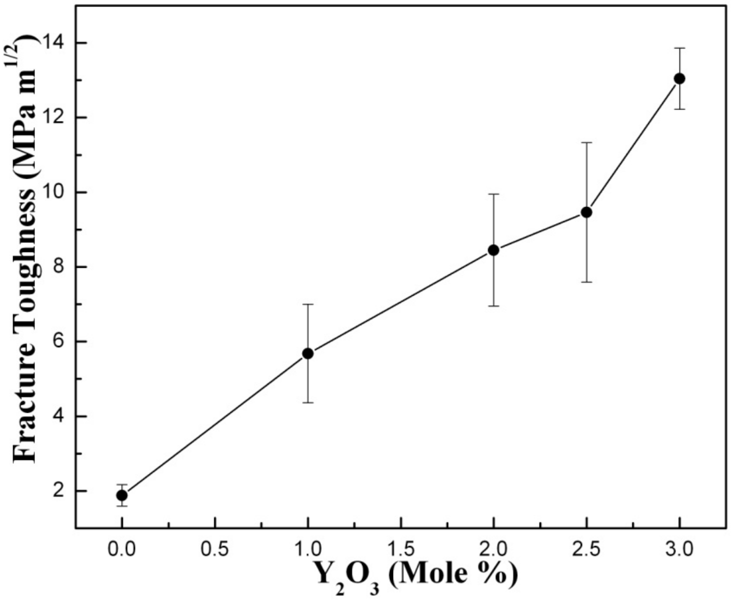

Fig.6.13. Fracture toughness of Al_2O_3-Y-ZrO_2 composites as a function of Y_2O_3 content

The observed toughness values are quite high and it is possible that more than one toughening mechanism is operative in this composite. Besides transformation toughening, additional toughening effect that may arise from some grain boundary phase which either change the crack propagation path (intergranular to transgranular) or may cause crack deviation, microcrack toughening and/or combined action of these mechanisms. In order to compute the contribution of transformation toughening (ΔK_{ICTT}) to the overall toughness, the fraction of transformable t-ZrO_2 was measured on the ground surface for the two high toughness compositions, viz, Al_2O_3-2.5Y-ZrO_2 and Al_2O_3-3Y-ZrO_2. The volume fraction of transformed t-ZrO_2 was found by measuring the volume fraction of net m-ZrO_2 on the ground surface using Eqn. 4.10 and 4.11. Although Al_2O_3-2Y-ZrO_2 also had high toughness but due to the presence of large monoclinic phase on the sintered surface (Table 6.3), the zone depth could not be accurately calculated and theoretical evaluation of toughness was made only on Al_2O_3-2.5Y-ZrO_2 and Al_2O_3-

$3Y-ZrO_2$ samples. The volume fractions of transformed $t-ZrO_2$ for those three compositions are shown in Table 6.3.

Table 6.3 Volume fraction of transformed t-ZrO_2 on the ground surface of sintered A_2O_3-Y-ZrO_2 compositions

Composition	***Fraction m-ZrO_2 phase on sintered surface***	***Fraction m-ZrO_2 phase on ground surface***	***Fraction t-ZrO_2 transformed***
Al_2O_3-2Y-ZrO_2	0.86	0.94	0.08
Al_2O_3-2.5Y-ZrO_2	0.07	0.50	0.43
Al_2O_3-3Y-ZrO_2	0	0.39	0.39

Using the above data and the transformation toughening model of Mc Meeking and Evans [6.1] and considering shear and dilation stress, the transformation toughening contribution was evaluated from the following equation:

$$\Delta K_{IC\,TT} = \frac{0.38\,EV_f\sqrt{h}\;e^T}{(1-\nu)} \qquad (6.2)$$

The composite elastic modulus (E) was calculated using the volume fraction of each phase (viz. Al_2O_3 and ZrO_2) and their respective E values (E_{Al2O3} = 380 GPa and E_{ZrO2} = 210 GPa), V_f is the volume fraction of transformed t-ZrO_2 phase obtained from Table 6.1, e^T is the transformation strain (e^T = 0.06), h is the transformation zone depth. The transformation zone depth was calculated using Mori's formula [6.2].

$$h = \frac{\sin\theta}{2\mu}\left[\frac{X_{meas}-X_{bulk}}{Y_{bulk}-X_{meas}}\right] \qquad (6.3)$$

where, X and Y denotes the fraction of monoclinic and tetragonal ZrO_2 and the subscript refer to their position. μ is the linear absorption coefficient and for Al_2O_3-50 vol% ZrO_2 composite, μ is taken to be 0.037, 2θ is the diffraction angle for t-ZrO_2 [6.3]. The calculated zone depth (h) for all the two levels of Y_2O_3 doping is listed in Table 6.4.

Table 6.4 Transformation zone depth of sintered Al_2O_3-Y-ZrO_2 compositions

Y_2O_3 (Mol%)	Zone depth (h) (μm)
2.5	2.99
3	4.69

The contribution of transformation toughening (ΔK_{ICTT}) to the overall toughening was evaluated on the basis of Eqn. 6.2 using the data provided in Table 6.3 and 6.4. The calculated ΔK_{ICTT} values for the three compositions of Al_2O_3-Y-ZrO_2 composites are listed below:

Table 6.5 Comparison of the experimental and calculated fracture toughness of sintered Al_2O_3-Y-ZrO_2 compositions

Composition	Experimental K_{IC} (MPa√m)	Calculated K_{IC} (MPa√m)	Difference (MPa√m)
Al_2O_3-2.5Y-ZrO_2	9.46	7.36	+2.10
Al_2O_3-3Y-ZrO_2	13.04	9.21	+3.83

Thus, it could be seen that besides transformation toughening some other toughening mechanism is also helping the toughness increment. In an attempt to understand the other possible mechanisms resulting in the toughness increment, detailed microstructural analysis was carried out through FE-SEM and TEM.

The FE-SEM images (SE mode) of Al_2O_3-2.5Y-ZrO_2 and Al_2O_3-3Y-ZrO_2 are shown in Fig. 6.14 (a, b) and (c, d) respectively. The lower magnification images Fig. 6.14 (a, c) shows that the ZrO_2 grains (0.53 μm) are smaller than that Al_2O_3 (0.69 μm).It has also been observed that in Al_2O_3-3Y-ZrO_2 (Fig. 6.14 d), both intergranular and transgranular cracks are present which is absent in Al_2O_3-2.5Y-ZrO_2 (Fig. 6.14 b). The intergranular cracks are present at Al_2O_3-ZrO_2 interface and the transgranular cracks are found to start mostly from the ZrO_2 grains (bright grains, arrow marked). This feature is not present in Al_2O_3-2.5Y-ZrO_2 composite.

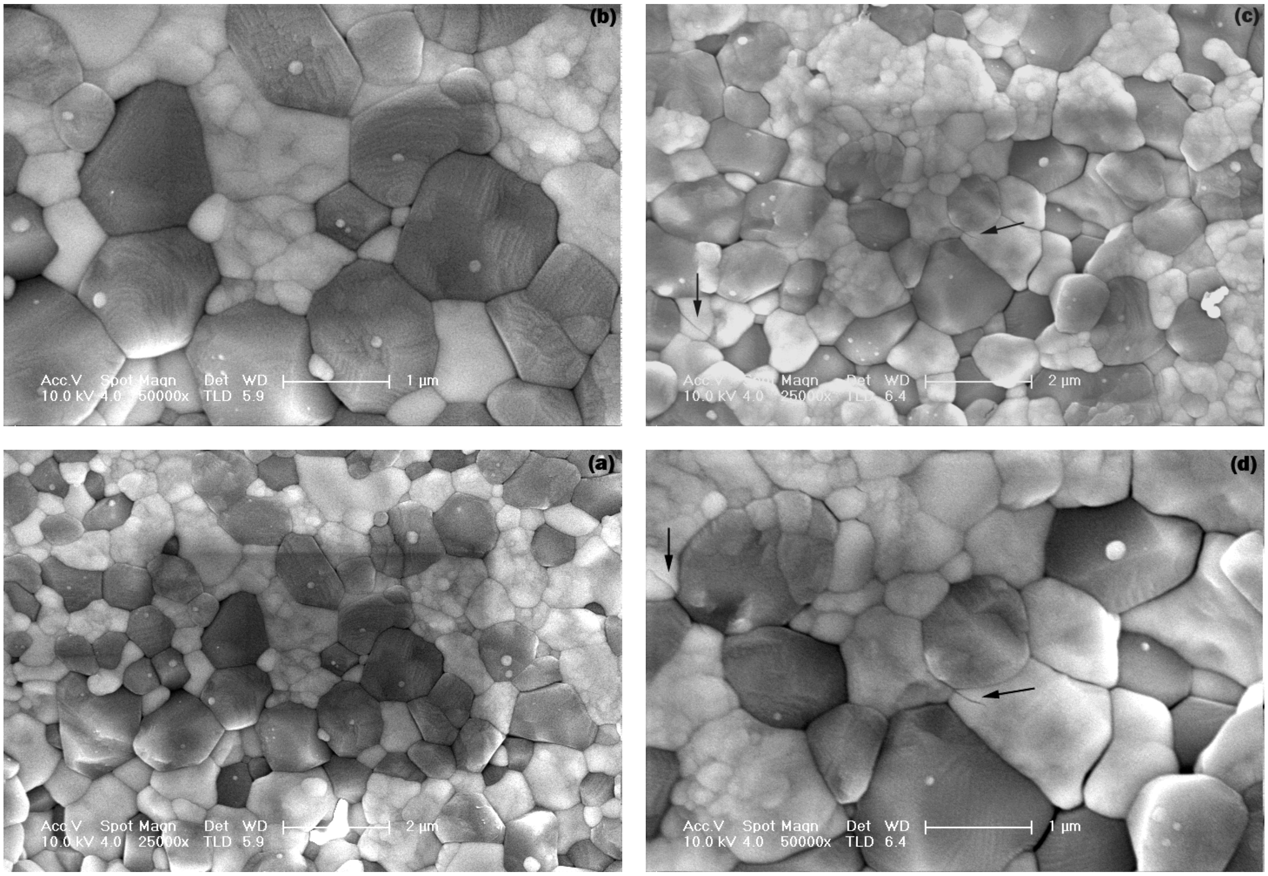

Fig.6.14. FE-SEM microstructure of Al_2O_3-2.5Y-ZrO_2 (a, b) and Al_2O_3- 3Y-ZrO_2 composites (c, d).

It was also observed (through EDAX) that in Al_2O_3-3Y-ZrO_2, there was Y^{3+} concentration gradient from ZrO_2 to Al_2O_3 grains through the ZrO_2-Al_2O_3 interface. The presence of both intergranular (curve) and transgranular cracks (arrow marks) as well as Y^{3+} concentration gradient suggests the possibility of new compound formation at the interface definitely in Al_2O_3-3Y-ZrO_2 and possibly in Al_2O_3-2.5Y-ZrO_2. Therefore, it was decided to further study the microstructure of these two compositions through TEM with the possibility of looking more minutely at the interface. Figure 6.15(a) shows the HR-TEM microstructure of Al_2O_3-2.5Y-ZrO_2. The upper image represents the lattice image of ZrO_2 grain (d =1.88 A^o) and the lower image represents the Al_2O_3 (d =4.07 A^o) grain. But it is also seen that at the interface a third structure also exists.

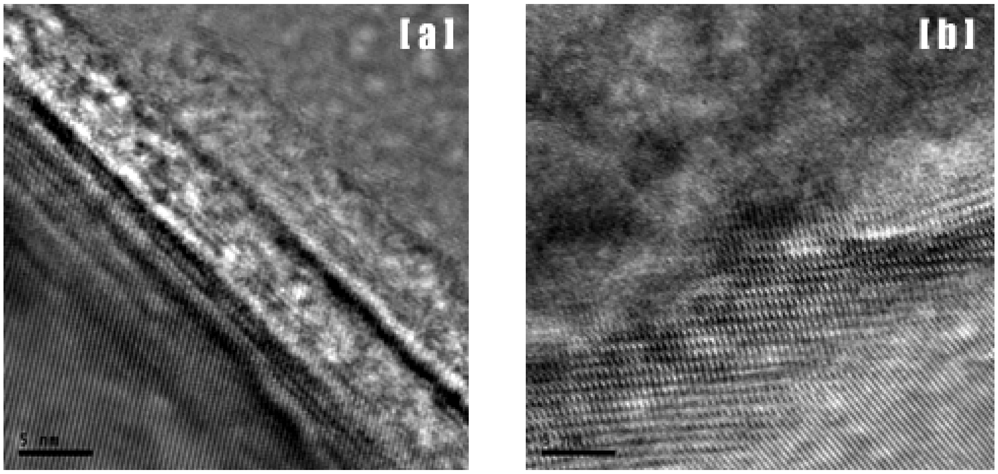

Fig.6.15. HRTEM image of (a) Al_2O_3-2.5Y-ZrO_2 (b) Al_2O_3-3Y-ZrO_2 composites

Figure 6.15(b) shows the HR-TEM image of Al_2O_3-3Y-ZrO_2 interface. As before, the lower image is Al_2O_3 (d=4.08A^0) and upper image are ZrO_2 (d=1.88A^0). At the interface, a secondary phase is clearly seen which is identified as YAG (d=4.21A^0). It appears that the migration of Y^{3+} across the Al_2O_3-ZrO_2 interface at the high sintering temperature resulted in nano-YAG formation at the interface. Similar results have been reported by Gao et al. [6.4] and Moya et al. [6.5] while working with Al_2O_3-25 vol% Y_2O_3 composites. At high sintering temperature, Al_2O_3 and Y_2O_3 react to form YAG. However, in the present investigation, since the amount of Y_2O_3 is very less (2 -3 mol%) in comparison to the reported study and only a certain fraction of the Y_2O_3 is diffused, the interface layer will be very thin (in angstrom level). The presence of YAG appears to have helped in enhancing the toughness by three possible mechanisms: (a) the YAG improves the grain boundary strength, (b) the presence of YAG (due to higher α) also induces a residual stress on ZrO_2 (ZrO_2 grains are put in tension) and this might have helped in higher transformability of ZrO_2 grains there by leading to higher toughness and (c) the migration of Y^{3+} towards Al_2O_3-ZrO_2 interface lowers the overall Y^{3+} concentration in ZrO_2 to less than 3 mol%. Thus the Y_2O_3 distribution in ZrO_2 grains becomes inhomogeneous making it more susceptible to transformation under the applied stress (the stress level to initiate the transformation decreases). The effect of inhomogeneous dopant distribution on the enhanced transformability has also been reported by Lange et al. [6.6] and Basu et al. [6.7]. Moreover, Nihara et al. [6.8, 6.9] have investigated the microstructure and properties of different kind on nanocomposites and reported significant improvements of mechanical properties when nano-size dispersions were present in the composite within the matrix grains and at the grain boundaries. It has also been reported that among the different type of nano-composites; the inter-type had improved mechanical properties like strength, toughness and hardness.

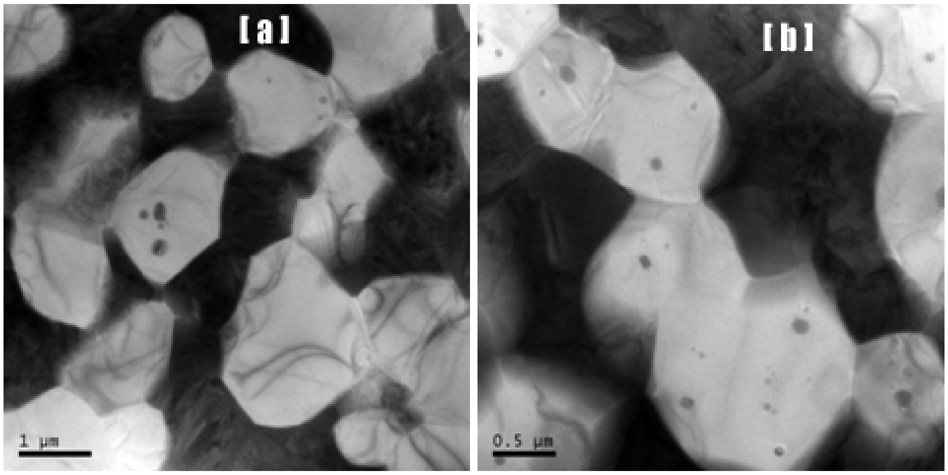

Fig.6.16. TEM Microstructure of sintered Al_2O_3-Y-ZrO_2 composites (a) 2.5 Y (b) 3 Y. The microstructure shows the grains are of sub micron size with nano intragranular dispersion

The microstructure (Fig.6.16 (a, b)) of the composites in the present investigation also suggests that these composites are of nano intra type. Thus it appears that presence of intragranular nano phase as well as the intergranualr YAG phase has caused the improvement of strength and toughness of Al_2O_3-Y-ZrO_2 composites. The possible strengthening and toughening mechanisms are grain boundary strengthening (due to grain boundary YAG phase), existence of both intergranular and transgranular fracture mode, enhanced transformability of Y-ZrO_2 grains (due to Y^{3+} migration) as well as the unique combination of micro-nano composites as suggested by Nihara [6.8].

6.4 Hardness of Al_2O_3-Y-ZrO_2 Composites

The Vickers hardness of Al_2O_3-Y-ZrO_2 composites as a function of sintering temperature is shown in Fig. 6.17. The hardness increases with sintering temperature as well as Y_2O_3 content. The increase in hardness is due to the increased density of the composite. The hardness increases both due to sintering temperature as well as Y_2O_3 addition. The maximum hardness is 14 GPa for Al_2O_3-3Y-ZrO_2 composites sintered at 1600°C.

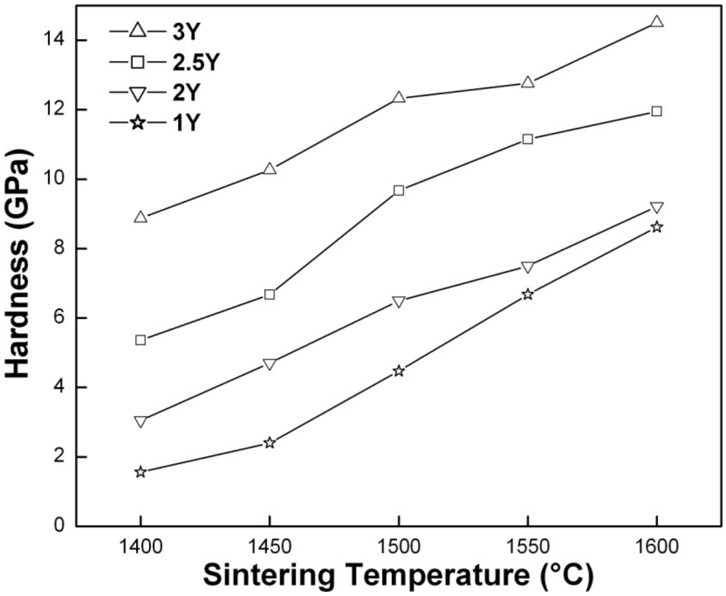

Fig.6.17. Vickers hardness of Al_2O_3-Y-ZrO_2 composites as a function of sintering temperature

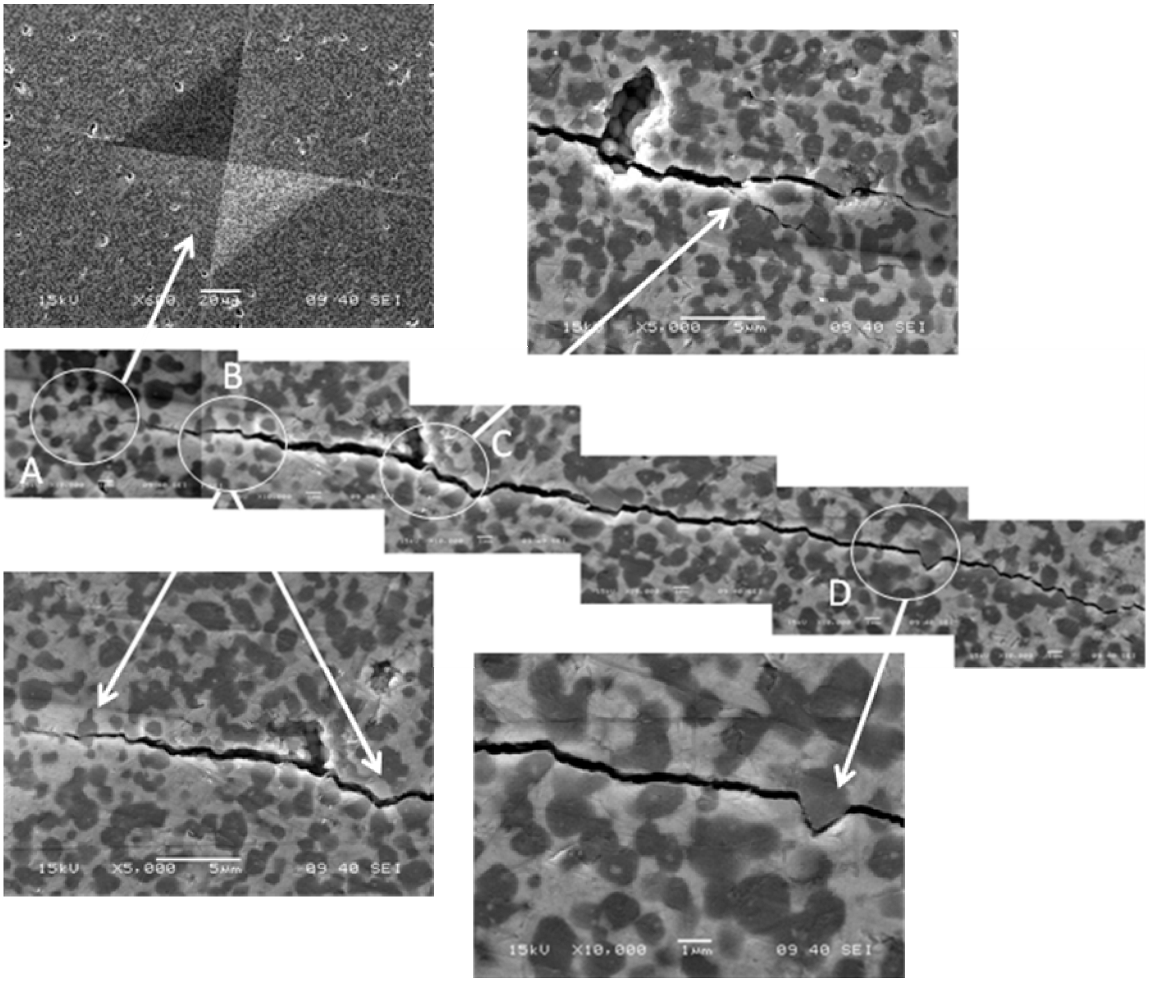

Fig. 6.18 Crack propagation path in indented Al_2O_3-3Y-ZrO_2 composites. The central figure is the combined picture showing the crack propagation paths and the different zones (A, B, C, D) are enlarged in the four corners

At the same sintering temperature, the hardness values for Al_2O_3-2Y-ZrO_2 and Al_2O_3-2.5Y-ZrO_2 composites are 9 and 12 GPa respectively. Similar trend in hardness has also been observed by Basu et al. [6.10].

The nature of the crack propagation (on impact) in Al_2O_3-Y-ZrO_2 was also studied by SEM. Figure 6.18 shows the crack propagation behavior from the corner of an indent for Al_2O_3-3Y-ZrO_2 composites (Zone A). A careful observation of the crack propagation path reveals that the crack path is tortuous – i.e. the crack deviates from its main path (Zone A-D), the crack cuts through the particle (Zone B) or the crack branches out (Zone C) or the crack bypasses a particle (Zone D). Similar observations have also been made on the indentations carried out on Al_2O_3-2.5Y-ZrO_2 composites Fig. 6.19 (a, b), where most of the above features (as observed in Al_2O_3-3Y-ZrO_2 composites) such as tortuous crack path, crack either bypassing a particle or cutting through a particle is also observed [Fig. 6.19 (b)]. The above observation suggests that due to multiple toughening mechanism operating simultaneously in Al_2O_3-3Y-ZrO_2 composites; the crack propagation is not easy in this composites and high toughness values are obtained.

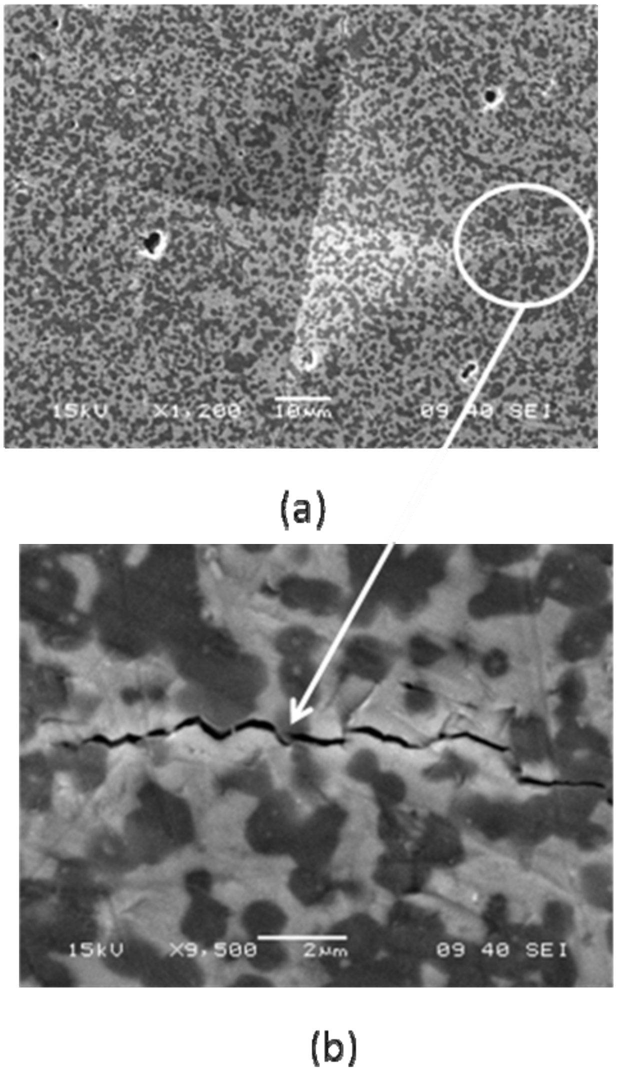

Fig. 6.19 Crack propagation paths in indented Al_2O_3-2.5Y-ZrO_2 composites. The upper figure (a) shows the indent with crack and the crack path are enlarged in the bottom figure (b).

6.5 Thermal Shock Resistance of Al_2O_3-3Y-ZrO_2 Composites

The thermal shock resistance of Al_2O_3-3Y-ZrO_2 (because it has the proper combination of high strength and toughness) was studied by air quenching method. The samples were heated to three different temperatures (1200, 1100, and 1000^oC) and air quenched from that temperature. Strength and toughness (SENB method) were measured on these quenched samples.

Table 6.6 Effect of thermal quenching temperature on the strength and toughness of Al_2O_3-3Y-ZrO_2 composites

Quenched from temperature (^oC)	σ_f (MPa)	K_{IC} (MPa√m)
1000	547	7.28
1100	485	4.55
1200	473	4.02
No quenching	645	13.04

Table 6.5 shows the results of thermal quenching temperature on the strength and toughness of Al_2O_3-3Y-ZrO_2 composites. It is seen from the Table that although the toughening is drastically affected by quenching temperature, the strength degradation is less due to the quenching. The decrease in toughness on quenching appears to be due to the generation of microcracks but these microcracks did not affect the strength that much. This hints at strengthening of grain boundary by nano YAG [6.4]. However, the results show that this composition retains significant strength and toughness even when quenched from 1000^oC The strength and toughness trends are different from the usual trend observed for quenched samples (the loss of strength on quenching is less drastic)> it is possible that the presence of nano YAG (due to its high strength both at room and high temperature) at the grain interfaces might have caused high strength.

References

6.1 R.M. McMeeking and A.G. Evans, “Mechanics of transformation toughening in brittle materials”, J. Am. Ceram. Soc, 65, 242-246 (1982).

6.2 Y. Mori, Y. Mori, Y. Kitano and A. Ishitani, “X-ray Determination of transformation zone size in toughened zirconia ceramics”, J Am. Ceram. Soc., 71, C-322-C-324 (1988).

6.3 T. Kosmac, R. Wagner and N. Claussen,” X-ray determination of transformation depths in ceramics containing tetragonal ZrO_2”, J Am. Ceram. Soc., 64, C-72-C-73 (1981).

6.4 W.Q. Li and L. Gao, “Processing, microstructure and mechanical properties of 25 vol% YAG-Al_2O_3 nanocomposites”, NanoStructured Materials,11, 1073–1080, (1999).

6.5 C. Pecharromán, A. Esteban-Cubillo, R. Torrecillas and J.S. Moya, “Micro/nano composites: a simple and safe way to fabricate nanomaterials”, Int. J. Nanotechnology, 4, 282-297 (2007).

6.6 F F Lange, D B Marshall and J R Porter, “Controlling microstructures through phase partioning from metastable precursors: The ZrO_2-Y_2O_3 System”, in Ultrastructure Processing of Advanced Ceramics, Proceedings of the Third International Conference on Ultrastructure Processing of Ceramics, Glasses and Composites, San Diego, CA, 1988, pp 519-532.

6.7 B. Basu, J. Vleugels and O. Vander Biest, “Transformation behaviour of tetragonal zirconia: role of dopant content and distribution”, Mat. Sci. and Engg. A, 366, 338–347(2004)

6.8 K. Nihara, “New design concept of structural ceramics: Ceramic Nanocomposites”, J. Ceram. Soc, Jpn, 99, 974-982 (1991).

6.9 K. Niihara and Y.Suzuki, “Strong monolithic and composite $MoSi_2$ materials by nanostructure design”, Mat. Sci.and Engg. A, 261, 6–15 (1999).

6.10 B. Basu, J. Vleugels and O. Vander Biest, “Al_2O_3-ZrO_2 composites with tailored toughness”, Journal of Alloys and Compounds, 372, 278–284 (2004).

Chapter VII

Conclusions and Scope of Further Work

7.1 Conclusions

The present study on the powder processing densification behavior and mechanical properties of Al_2O_3-high zirconia composites were undertaken to study the following:

a) Use of different powder processing methods on the powder properties, its optimization and t-ZrO_2 retention.
b) Effect of precursor type (or nature of anions) on the metastable phase evolution and densification behaviour as well as properties of similar composites.
c) Detailed densification mechanism of the composites during initial stage sintering.
d) Effect of stabilizer on the composite properties, microstructures, strength, toughness and hardness.
e) Exploring the possible strengthening and toughening mechanism in these composites.

In this present study, Al_2O_3- 50 vol% ZrO_2 composites were processed through soft chemistry routes using $AlCl_3$ or $Al(NO_3)_3$ and $ZrOCl_2$ as the respective precursors. Three different processing routes, viz. gelation (ROUTE 1), precipitation (ROUTE 2) and precipitation followed by washing (ROUTE 3) of the precipitates were adopted. Only the ROUTE 3 gave the desired composite with 88% sintered density (for $AlCl_3/ZrOCl_2$ precursor combination). Microstructural analysis showed residual porosity in the sintered samples and FTIR of the calcined powder confirms the presence of residual chloride ions. It has been well documented that the presence of residual chloride ions can adversely affect the densification behavior. In the present study, it was found that not only the removal of chloride ions but also the removal of $(OH)^-$ groups of Al^{3+} causes weight loss during the later stage of sintering. Chloride ions were partially reduced when $Al(NO_3)_3$ replaced $AlCl_3$ as the precursor for Al_2O_3 (ROUTE 4). FTIR study showed lesser amount of chlorides in the calcined powder and the sintered density increased to 95% of theoretical. The washing of the precipitates by water and alcohol reduced the agglomeration tendency of the powders thereby increasing their sinterability. This specific feature was elaborately studied through TEM photography of the calcined powder, determination of agglomeration strength and SEM microstructure of sintered samples. The TEM picture showed less agglomerated powder and the agglomeration strength was 97 MPa. This marks the end of the first section and it was observed at this stage that due to the low elastic modulus of the composite (260 GPa). The matrix could not provide constraint to arrest the spontaneous $t \rightarrow m$ ZrO_2 transformation. So, all the sintered composites had very small fraction of retained t-ZrO_2 (5 to 10 vol%). This factor coupled with existence of extensive microcracking (as a result of spontaneous $t \rightarrow m$ transformation) could not improve the mechanical properties of the composites in specific strength and toughness, which were very low (σ_f =88.7 MPa, K_{IC} = 1.9 MPa√m).

The densification of Al_2O_3-ZrO_2 composite showed duplex sintering behavior for all processing routes. However, the onset temperature was different and could be correlated with surface area, particle size and agglomeration strength of the calcined powder. The densification kinetics and activation energy of Al_2O_3-ZrO_2 composites was determined from isothermal and non-isothermal dilatometry study. The value of kinetic parameter '*n*' varied between 5.02 and 5.22 which indicate that volume diffusion is the dominant mass transfer mechanism and the activation energy for initial stage of sintering was 236-258 kJ mol^{-1}.

The second part of the study involved the addition of Y_2O_3 (1, 2, 2.5 and 3 mol %) to the precursor solution of Al and Zr salt, so that Y-TZP could form during calcination and subsequent sintering process. It was observed that the addition of Y_2O_3 not only helped to retain large fraction of t-ZrO_2 in the sintered composites but the sintered density was also significantly improved and all the Y-doped compositions had high sintered density (>90%) and while Al_2O_3-2.5Y-ZrO_2 composition could retain 93% of t-ZrO_2 it was 100% for Al_2O_3-3Y-ZrO_2. Both flexural as well as biaxial flexural strength had improved with Y_2O_3 doping and the highest values were 645 and 335 MPa respectively. It was noted that only for Al_2O_3-1Y-ZrO_2 composites the strength was flaw controlled while for others it was transformation controlled. The fracture toughness (SENB method) increased from 5.68 MPa√m (at 1 mol% Y_2O_3) to 9.46 MPa√m in Al_2O_3-2.5Y-ZrO_2 composites which further increased to 13.04 MPa√m in Al_2O_3-3Y-ZrO_2 composites. The K_{IC} results were analyzed in terms of transformation toughening model of Evans and Mc Meeking and it was found that transformation toughening was not able to account for the entire toughness increment. Thus some other toughening mechanisms were also simultaneously operative. Assuming that there might be some additional microstructural features, selected samples (with 2.5 and 3 Y_2O_3 doping) were observed in FESEM and TEM. FESEM indicated that Al_2O_3-3Y-ZrO_2 had some transgranular cracks in ZrO_2 grains. EDAX analysis revealed a concentration gradient of Y^{3+} from ZrO_2 grain to Al_2O_3 grain. TEM picture of bulk Al_2O_3-2.5Y-ZrO_2 and Al_2O_3-3Y-ZrO_2 samples revealed the presence of a third phase at the interface of Al_2O_3 and ZrO_2. HR lattice image of the interface area confirmed that YAG has formed at the interface. Thus it appears that the formation of YAG in situ and its deposition along grain boundary of Al_2O_3/ZrO_2 is responsible for property improvement as it allows the simultaneous operation of a number of additional mechanisms like grain boundary strength, generation of residual tensile stress at ZrO_2 grain and the initiation of transgranular fracture.

The hardness of all Al_2O_3-Y- ZrO_2 composites increased at higher sintering temperature as well as at higher Y_2O_3 content. This implies that addition of Y_2O_3 promotes densification due to enhanced mass transport augments densification of the composites.

The study of thermal shock resistance behavior for Al_2O_3-3Y-ZrO_2 composites showed that the thermal shock resistance is high till $\Delta T = 1000^oC$ where the retained fracture toughness is 7.28 $MPa\sqrt{m}$ and fracture strength is 540 MPa.

7.2 Scope of Further Work

The present study reveals that powder processing is an important step for achieving a dense microstructure. The anions (particularly chlorides and hydroxyl groups) affect the sintered density and phase retention as the above ions go off at high temperature where pore coalescence is not possible. Y_2O_3 doping improves the situation through the formation of YAG phase at Al_2O_3/ZrO_2 interface. The doping also results in significant improvement of strength, toughness, hardness and thermal shock resistance. However, it is felt that some more questions needs to be answered and these are suggested as the possible future work:

(i) Is it possible to improve the densification behavior and phase retention (t-ZrO_2) of the Al_2O_3-undoped ZrO_2 composites by either hot pressing or vacuum sintering or spark plasma sintering? Will the anions still affect the densification and phase retention?

(ii) What may be the effect of two stage rapid sintering on the density, microstructure and properties?

(iii) Y_2O_3 doping results in the property enhancement, but the amount of Y_2O_3 need to be optimized.

(iv) Will this type of behavior still exist if prereacted Y_2O_3 doped ZrO_2 is dispersed in Al-sol for preparing the composites?

(v) What will be the tribological behavior of these composites?

(vi) The composites had a good combination of strength, toughness and hardness. Thus it may be used as a cutting tool material. However it is possible that this material have some bioactive properties or in other words can it be used in biomedical applications where dense prostheses are used?

Publications resulting from the Ph.D. work

1) **R.P. Rana,** S.K. Pratihar and S. Bhattacharyya, "Effect of Powder Treatment on the Crystallization behaviour and Phase Evolution of Alumina- High Zirconia Nanocomposites", J. Mater. Sci. 41 (2006) 7025–7032.

2) **R.P.Rana**, S.K.Pratihar and S. Bhattacharyya, "Powder Processing Route and Densification Behaviour of Alumina – High Zirconia Composites Using Chloride Precursors" J. of Mat. Pro. Tech., 190(2007), 350-357.

Curriculum Vitae

Raghunath Prasad Rana
S/O Mr. Bhikari Charan Rana
At:-Ashok Nagar & P.O. - Athgarh
District-Cuttack, Orissa-754029, INDIA.
Phone No: +91-6723-220925 (R), +91-9337293283 (M)
Email: raghunath_rana@yahoomail.com

Date of Birth: 25.04.1980

Education: Ph.D., B. Tech. (Chemical Engg.)

Technical Exposure: Publication: **4**, Conference: **13**

Work Experience: Presently working as a **Research Scientist** in R&D at
Tata Refractories Ltd. Belpahar, Orissa since 25th August 2008.

Publications:

3) **R.P. Rana,** S.K. Pratihar and S. Bhattacharyya, "Effect of Powder Treatment on the Crystallization behaviour and Phase Evolution of Alumina- High Zirconia Nanocomposites", J. Mater. Sci. 41 (2006) 7025–7032.
4) **R.P.Rana**, S.K.Pratihar and S. Bhattacharyya, "Powder Processing Route and Densification Behaviour of Alumina – High Zirconia Composites Using Chloride Precursors" J. of Mat. Pro. Tech., 190(2007), 350-357.
5) Y.Nayak, **R.P.Rana**, S.K. Pratihar, S. Bhattacharyya., "Low Temperature Processing of Dense Hydroxyapatite-Zirconia composites" International Journal of Applied Ceramic Technology, 5, 1 (2008), 29-36.
6) Y.Nayak, **R.P.Rana**, S.K. Pratihar, S. Bhattacharyya.,"Pressure Less Sintering of Dense Hydroxyapatite-Zirconia Composites", Accepted in Journal of Materials Science: Materials in Medicine Jan 2008.

Professional Membership:
Studentship member of Indian Science Congress Association [M. No.181].